

ALICE

Addendum to the Letter of Intent

CERN-LHCC-2013-014

LHCC-I-022-ADD-1

ALICE-UG-003

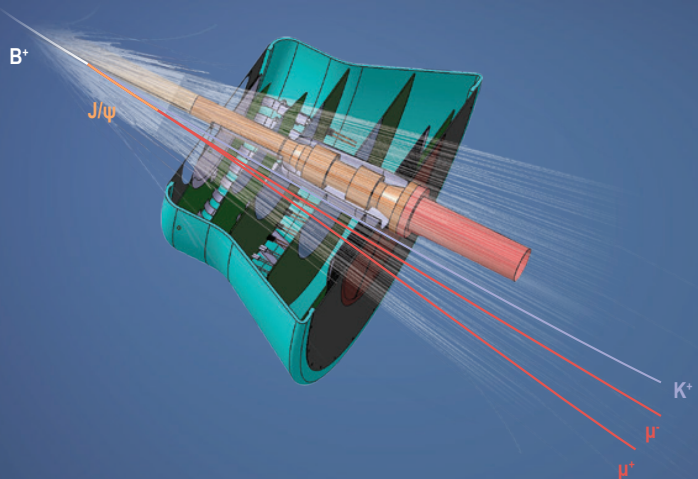
September 25, 2013



Upgrade of the **ALICE Experiment**

Addendum to the Letter of Intent

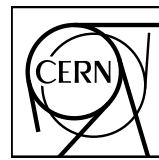
The Muon Forward Tracker





ALICE

ALICE-UG-003



CERN-LHCC-2013-014 / LHCC-I-022-ADD-1

September 25, 2013

Upgrade of the ALICE Experiment

Addendum to the Letter of Intent

The Muon Forward Tracker

The ALICE Collaboration*

Copyright CERN, for the benefit of the ALICE Collaboration.

This article is distributed under the terms of Creative Commons Attribution License (CC-BY-3.0), which permits any use provided the original author(s) and source are credited.

*See Appendix A for the list of collaboration members

Contents

Introduction	1
Physics program with the MFT	1
Current Muon Spectrometer performance and limitations	2
Comparison of MUON / MUON+MFT scenarios	4
Physics performance of the MFT compared with other LHC approved programs	4
MFT Beyond Muon Physics	7
1 Physics motivation	9
1.1 Heavy Flavour and Quarkonium Physics	9
1.1.1 Open Heavy Flavour in Heavy Ion Collisions	9
1.1.2 Charmonium in Heavy-Ion Collisions	11
1.1.3 Bottomonium in Heavy-Ion Collisions	13
1.1.4 The Low p_T Yield Excess in Heavy-Ion Collisions.	13
1.1.5 Exotic Heavy-Flavour Studies	14
1.1.6 Summary of MFT Motivation Related to Heavy-Flavour Physics	14
1.2 Low-Mass Dimuons in Heavy-Ion Collisions	15
1.2.1 Chiral Symmetry Breaking and Restoration	16
1.2.2 Experimental Probes	16
1.2.3 Experimental Status	17
1.2.4 Current Theoretical Scenario	17
1.3 Proton-Proton and Proton-Nucleus Collisions	18
2 Performance Studies for the Muon Forward Tracker	21
2.1 MFT Simulation Strategy	21
2.1.1 A “Standard Setup” for the MFT	21
2.1.2 Full Simulations: the MFT in the AliRoot Framework	22
2.1.3 Fast Simulations for the MFT	24

2.2	Global Event Properties	24
2.2.1	Expected Interaction Rates and Pile-up	24
2.2.2	Occupancy of MFT Planes	25
2.3	Global Fit Performance for the Single Muons	26
2.3.1	Phase Space Available	26
2.3.2	Correct Matching Rate	27
2.3.3	Pointing Accuracy	27
2.3.4	Prospects for the MFT Standalone Tracking	31
2.4	Charmonium States in Central Pb–Pb	31
2.4.1	Signal and Background Simulations	31
2.4.2	Cuts and Selections	32
2.4.3	Background Rejection	33
2.4.4	Expected Yields and Signal Extraction	34
2.4.5	Contribution of the MFT to the ALICE Charmonia Program	44
2.5	Open Heavy Flavour in Central Pb–Pb collisions	46
2.5.1	Signal and Background Simulations	46
2.5.2	Track Selection	47
2.5.3	Expected Yields and Signal Extraction for Single Muons	48
2.5.4	Expected Yields and Signal Extraction in Dimuons	53
2.5.5	Contribution of the MFT to the ALICE Heavy-Flavour Program	55
2.6	Low Mass Dimuons in Central Pb–Pb	58
2.6.1	Signal and Background Simulations	58
2.6.2	Cuts and Selections	59
2.6.3	Rejection Power	59
2.6.4	Mass Resolution	61
2.6.5	Expected Yields and Signal Extraction	63
3	Detector Technology and Integration	67
3.1	CMOS Monolithic Pixel Sensor Technology	67
3.2	Data Flow and Readout Architecture	68
3.3	General Layout	68
3.4	MFT Design	69
3.4.1	Global Design	69
3.4.2	Design of the Ladders	69

3.4.3	Design of a Half Disk	70
3.5	MFT Cooling	74
3.5.1	Cooling System	74
3.5.2	Cooling Simulations	75
3.6	Assembly Procedure	76
3.7	Integrations Aspects	76
3.7.1	The Services	76
3.7.2	The Mechanical Supports	78
3.7.3	Integration Constraints from Other Forward Detectors	80
3.8	Alignment Strategy	81
4	Project Organisation	83
4.1	Project Management	83
4.2	Participating Institutes	84
4.3	Cost Estimate	85
A	The ALICE Collaboration	87
References		94

Introduction

Heavy-ion collisions at relativistic energy produce a piece of matter with extremely high temperature and energy density. In such thermodynamical conditions, matter presents itself as a strongly-interacting partonic medium in which quarks and gluons are no longer bound like in hadrons but can roam freely. This deconfined medium is called the Quark Gluon Plasma (QGP). It is believed to have filled the Universe a few microseconds after the Big Bang. With a nucleus-nucleus center of mass energy of a few hundred TeV, the system produced in heavy-ion collisions at the LHC reach the highest temperature and energy density ever achieved in the laboratory. This together with the almost vanishing baryon chemical potential of the system renders it close to the conditions of the primordial Universe and offers an ideal ground for the study of the QGP.

In the energy regime of the LHC, heavy-ion collisions lead to a massive production of hard processes (heavy-flavour hadrons, quarkonia, photons and jets). They are sensitive probes of the collision dynamics at both short and long timescales. Their production cross section and interaction with the medium are well controlled theoretically thus allowing a detailed characterization of the deconfined medium. The ALICE physics program after LS2 is mostly devoted to a high precision measurement of these probes with an upgrade of the central barrel detectors as reported in [1] and with the Muon Forward Tracker (MFT) described in this Letter Of Intent. This will allow to study the properties of the QGP far beyond the capabilities of the present detector.

The motivation for operating the upgraded ALICE detector at high luminosity after LS2 are extensively discussed in [1]. We shortly describe hereafter the physics program specific to the MFT, its expected physics gain with respect to the existing ALICE Muon Spectrometer and compared to other existing LHC approved programs, as well as its capabilities to extend the physics reach in the forward region of ALICE beyond muon physics.

Physics program with the MFT

The quantitative understanding of the properties of QGP requires to precisely measure the fundamental parameters of the medium such as its temperature, energy density, transport coefficients and equation of state. This is to be achieved by studying how hard processes couple with the medium, possibly thermalize in the medium, and hadronize. The MFT physics program will be decisive in settling the following issues:

- Evaluate the medium temperature and study charmonium dissociation and regeneration mechanisms via measurements of prompt J/ψ and ψ' production and elliptic flow;

- Pin down the medium equation of state and study the degree of thermalization of heavy quarks in the medium via measurements of heavy flavour and charmonium elliptic flow;
- Extract the energy density of the medium, the color charge and mass dependence of parton in-medium energy loss via measurements of
 - heavy quark production separately for charm and beauty in the single muon channel;
 - J/ψ from b -hadrons decay.
- Investigate the chiral nature of the phase transition via measurements of low mass vector mesons.

The MFT will allow to perform high statistics measurements over a broad range in transverse momentum and versus collision centrality. Its acceptance will cover a forward pseudorapidity region which is not explored by any of the other LHC detectors thus making the measurements unique and complementary to those at mid-rapidity. Moreover, in this forward region, heavy-ion collisions at the LHC access unprecedented small Bjorken- x values where phenomena related to saturation of low-momentum gluons can be best evidenced.

Technologically, the MFT project will take advantage of a synergy with the R&D program already ongoing for the ITS upgrade, as both detectors are foreseen to share the same CMOS sensor technology.

Current Muon Spectrometer performance and limitations

Identification and measurement of muons in ALICE are currently performed by the Muon Spectrometer [2] covering the pseudo-rapidity region $-4 < \eta < -2.5$.¹ The Muon Spectrometer (Figure 1) is composed of the following elements:

- A hadron absorber made of carbon, concrete and steel, between $z = -0.9$ and $z = -5.03$ m; its material budget corresponds to ten hadronic interaction lengths ($60 X_0$), providing a reliable muon filter for momenta above $4 \text{ GeV}/c$ ($p_T \gtrsim 0.5 \text{ GeV}/c$).
- A dipole magnet placed at $z = -9.87$ m, 5 m long, providing a magnetic field of up to 0.7 T in the horizontal direction, corresponding to a field integral of 3 Tm.
- A set of five tracking stations, each one composed of two cathode pad chambers with a spatial resolution of about $100 \mu\text{m}$ in the bending direction: the stations are located between $z = -5.2$ and $z = -14.4$ m, the first two ones upstream of the dipole magnet, the third one in its gap and the last two ones downstream.
- A 1.2 m thick iron wall, corresponding to 7.2 hadronic interaction lengths, placed between the tracking and trigger systems, which absorbs the residual secondary hadrons emerging from the front absorber.
- The muon trigger system, consisting of two detector stations, placed at $z = -16.1$ and -17.1 m, respectively, each one composed of two planes of resistive plate chambers, with a time resolution of about 2 ns.

¹Where appropriate we will denote the Muon Spectrometer by the abbreviated name MUON, in particular in figure and table captions.

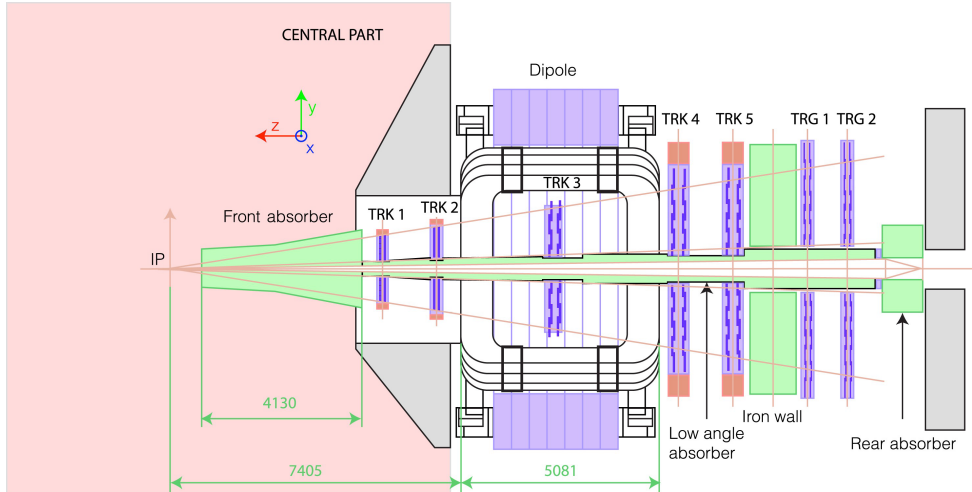


Figure 1: Schematic of the ALICE Muon Spectrometer.

Since the start of its data taking, the ALICE experiment has an important physics program based on muon measurements performed in pp, Pb–Pb and p–Pb collisions. Within this program three main directions can be identified: the study of quarkonium production [3], the study of open heavy flavour (HF) production [4], and the study of low mass dimuons [5].

The existing Muon Spectrometer has provided a wealth of results and will continue to do so. However, it has an important limitation, which prevents us from unleashing the full potential of muon measurements in ALICE. Effectively no track constraints in the region of the primary vertex are available from the spectrometer. This is mainly due to the large distance of the tracking stations from the primary vertex in combination with the multiple scattering induced on the muon tracks by the frontal absorber. The details of the vertex region are then completely smeared out: this, to begin with, leaves us with very limited possibilities to reject muons coming from semi-muonic decays of pions and kaons, representing an important background both in single muon and dimuon analyses, in particular at low masses and/or low p_T . In addition, the lack of details in the vertex region prevents us to disentangle prompt and displaced J/ψ production (the production of J/ψ from b -hadrons accounting for $\sim 10\%$ of the prompt cross section at low p_T) as well as to disentangle open charm and open beauty contribution to muon production directly from the data. Finally, the straggling of the track direction and the corresponding degradation of the angular resolution caused by multiple scattering in the hadron absorber plays a crucial role in determining the mass resolution for the resonances, especially at low masses in the region of the ω and ϕ mesons.

To overcome this limitation and to better exploit the unique kinematic range accessible at the LHC by the ALICE Muon Spectrometer, the Muon Forward Tracker (MFT) is proposed in the context of the ALICE upgrade plans, to take place in the years 2017/2018 during the LHC Long Shutdown 2. The MFT is a silicon pixel detector added in the Muon Spectrometer acceptance ($-4 < \eta < -2.5$) upstream of the hadron absorber. The basic idea, motivating the integration of the MFT in the ALICE setup, is the possibility to match the extrapolated muon tracks coming from the tracking chambers *after* the absorber with the clusters measured in the MFT planes *before* the absorber. For correct matches between the muon tracks and the MFT clusters, the muon tracks gain enough pointing accuracy to permit a reliable measurement of their offset with respect to the primary vertex of the interaction.

Comparison of MUON / MUON+MFT scenarios

Table 1 summarises the physics reach in central Pb–Pb collisions for different observables studied in Chapter 2. A comparison is presented between the two scenarios: the upgraded Muon Spectrometer alone as defined in [1] and the upgraded Muon Spectrometer with the addition of the proposed MFT. For both scenarios, an integrated luminosity of 10 nb^{-1} is assumed. In Chapter 2, the details of the simulations performed to evaluate the physics reach of the MFT will be shown.

Table 1: Comparison of physics reach for the two scenarios without and with the MFT (MUON only / MUON + MFT) assuming an integrated luminosity of 10 nb^{-1} in central Pb–Pb collisions. p_T^{\min} gives the minimum accessible p_T for the different observables. The quoted uncertainties include both statistical and systematic uncertainties.

Observable	MUON only		MUON + MFT	
	p_T^{\min} (GeV/c)	uncertainty	p_T^{\min} (GeV/c)	uncertainty
Inclusive $J/\psi R_{AA}$	0	5 % at 1 GeV/c	0	5 % at 1 GeV/c
$\psi' R_{AA}$	0	30 % at 1 GeV/c	0	10 % at 1 GeV/c
Prompt $J/\psi R_{AA}$		not accessible	0	10 % at 1 GeV/c
J/ψ from b -hadrons		not accessible	0	10 % at 1 GeV/c
Open charm in single μ			1	7 % at 1 GeV/c
Open beauty in single μ			2	10 % at 2 GeV/c
Open HF in single μ no c/b separation	4	30 % at 4 GeV/c		
Low mass spectral func. and QGP radiation		not accessible	1–2	20 % at 1 GeV/c

Physics performance of the MFT compared with other LHC approved programs

Other LHC experiments have an important program of upgrades [6–9] aiming at improving the experiments to cope with the ultimate luminosity that will be achieved during phases 2 and 3 of the LHC. LHCb experiment has no plan to run in heavy-ion collisions: indeed, the detector is not designed to cope with high multiplicities as encountered in Pb–Pb. Charmonia will be studied by all three other experiments in nucleus–nucleus collisions, ATLAS and CMS covering the central rapidities $|y| < 2.5$. The threshold in transverse momentum for the measurement of the charmonia is 3 GeV/c for the CMS experiment. The ATLAS and CMS measurements will complement the one we are proposing in the dimuon channel in the forward region ($2.5 < y < 3.6$), but also the one from the central part of ALICE in dielectrons ($|y| < 0.9$). The addition of the MFT upstream of the Muon Spectrometer allows a major enhancement of the muon physics capabilities in order to have similar detection performance at forward rapidities and at mid rapidity. As it has been shown by the RHIC experiments, the study of the QGP probes as a function of the rapidity along the Bjorken mid-rapidity plateau ($\Delta y \lesssim 4$ at LHC energies) is crucial for the understanding of the experimental results and to constrain experimental models [10–15]. We flash in this Section the main results of the performance simulation studies (details will be presented in Chapter 2).

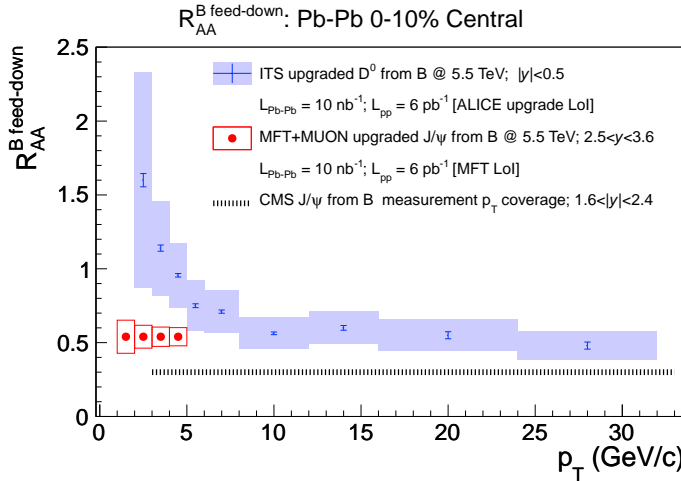


Figure 2: Beauty nuclear modification factor versus p_T of the observed particle. Comparison between the expected performance with the new ITS via the non-prompt D^0 measurement [1] (blue band) and the expected performance of the MFT/MUON via the non-prompt J/ψ identification (red points). The CMS p_T coverage via non-prompt J/ψ identification is represented (dotted line). The p_T in this figure refers to the p_T of the measured particle, $p_T^{D^0}$ in the case of the new ITS and $p_T^{J/\psi}$ for the MFT and CMS.

Thanks to its capability to measure muons coming from displaced vertices, the MFT is opening the possibility to separate prompt J/ψ from J/ψ coming from b -hadron feed-down. The expected performance on the nuclear modification factor of J/ψ from B decays are shown in Figure 2. This is compared to the expected performance of the new ITS on the nuclear modification factor of D^0 from B decays [1]. The MFT measurement is nicely complementing the CMS and the central ALICE measurements increasing the rapidity and p_T coverages to higher rapidity and lower p_T ².

The MFT allows a significant reduction of the combinatorial background coming from the semi-muonic decay of light hadrons, mainly pions and kaons. The background reduction is important for all signals, but is of major interest for the study of the ψ' in most central Pb–Pb collisions. The very low signal over background ratio obtained with the current Muon Spectrometer makes the ψ' extraction in the most central Pb–Pb collisions very difficult. The measurement of the ψ' , combined with the J/ψ measurement, offers an important tool to discriminate between different charmonium production models. Figure 3 shows the experimental status for the measurement of the $R_{AA}^{\psi'}/R_{AA}^{J/\psi}$ ratio, together with the expected performance of the MFT. The addition of the MFT allows a tremendous improvement of the physics reach.

The MFT will address the study of heavy flavour both in single muons and dimuons thanks to the charm/beauty separation, down to low- p_T ($p_T \sim 1$ GeV/c for charm and $p_T \sim 2$ GeV/c for beauty) even in central Pb–Pb collisions. The measurement at the lowest p_T is crucial in order to extract the total charm and beauty cross sections with the smallest systematic uncertainties possible. As the charmonium production models are very sensitive to the charm-production cross section, its precise measurement is of great interest for the understanding of the charmonium measurements in the same rapidity range.

The difference in the energy loss of heavy quarks, light quarks and gluons reflects in the hierarchy of the nuclear modification factors of light, charmed and beauty hadrons: $R_{AA}^\pi < R_{AA}^D < R_{AA}^B$. Mass and colour charge dependences can be investigated experimentally with the ratio of nuclear modification factors. Figure 4 shows the expected uncertainties on the R_{AA}^B/R_{AA}^D measurement as a function of

² We should mention here that the high- p_T limit on the MFT/MUON points is related to the statistics available in the simulation. The foreseen statistics in the data will allow a measurement up to 10 GeV/c.

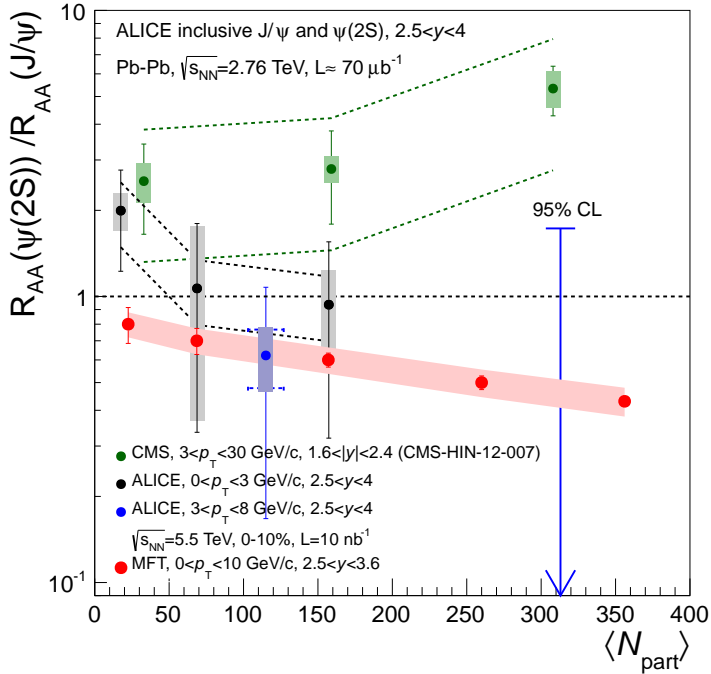


Figure 3: Ratio of the nuclear modification factor of ψ' and J/ψ versus the number of participants. The expected uncertainties of MFT/MUON (red points) are compared with the existing measurements of CMS (green points) and ALICE (blue and black points) at $\sqrt{s_{\text{NN}}} = 2.76$ TeV. The error bars represent the statistical uncertainties, the coloured area the systematic ones, while the dashed lines shows the uncertainties coming from the pp reference.

rapidity for two p_{T} intervals using the MFT in addition with the Muon Spectrometer compared to the expected performance of the new ITS. We should note that the measurement is done using the non-prompt and prompt D^0 measurement in the ITS, while the measurement is done using single muon in the MFT/MUON: therefore, the charm and beauty p_{T} accessed by those two measurements are not the same for the same p_{T} of the observed particle (D^0 or μ). The MFT offers a nice complement to the CMS and central ALICE measurements in rapidity coverage.

The high luminosity of the LHC combined with the ALICE capability of recording data in minimum-bias collisions at high rate will allow us to make a high precision measurement of low-mass lepton pairs. Again, due to the coverage down to low p_{T} , where interesting in-medium effects are expected, this measurement is unique at the LHC.

In conclusion, the ALICE capabilities for detecting muons at forward rapidity will be enhanced by the presence of the MFT detector: not only by a general improvement of the measurements with the Muon Spectrometer, but also by accessing new observables like prompt/displaced J/ψ separation and charm/beauty separation, in both cases to very low transverse momentum. It should be noted that ALICE with MFT will be the only experiment performing these measurements at forward rapidities at the LHC. Although the properties of the QGP at the LHC are expected to exhibit similar initial conditions within $|\eta| \lesssim 4.0$ [16], many other effects like shadowing, energy loss, charm rapidity density, could strongly vary with rapidity. At RHIC one of the most intriguing results was the unexpected rapidity dependence of several observables like charged hadron R_{AA} [17] or $J/\psi R_{\text{AA}}$ [14]. For this reason, it is crucial that different rapidity domains can be explored in heavy ion collisions at the LHC.

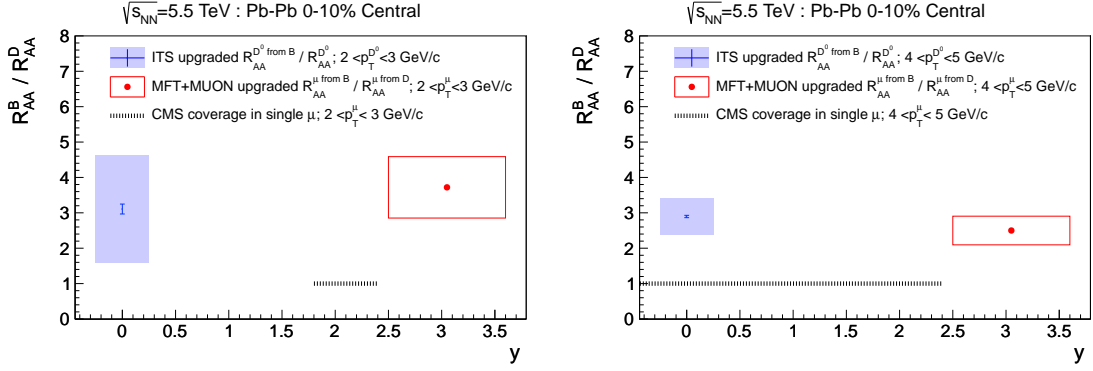


Figure 4: Ratio of the nuclear modification factors of open charm and beauty versus rapidity for $2 < p_T < 3 \text{ GeV}/c$ (left) and $4 < p_T < 5 \text{ GeV}/c$ (right). The uncertainties expected with the new ITS in the central rapidity domain using the non-prompts and prompts D^0 measurement (blue area) [1] are compared with the ones expected using the measurement of single muon coming from open charm and beauty using the MFT and the upgraded Muon Spectrometer (red points). These two methods are not probing the same p_T of the charm and beauty hadrons. Errors bars represent the statistical uncertainties while the boxes show the systematics uncertainties. The CMS rapidity coverage in single muon analysis is also represented (dotted line).

MFT Beyond Muon Physics

The physics performance studies described in Chapter 2 are related to the muon measurements. The MFT can of course be used as a standalone inner tracker without requiring any matching with the muon tracks. In that case, other physics topics can be studied, out of which we just mention the following:

- Direct multiplicity measurements at high rapidity;
- Measurement of the reaction plane and event anisotropies (complementing the central barrel detectors);
- Study of long range correlations exploiting the complementary ITS coverage at central rapidities.

As the MFT is using the same technology as the ITS, it will share with it the potential trigger capabilities, which can also make use of topological information.

No simulation addressing these different topics has been performed so far, but a dedicated effort will be done in the context of a Physics Performance Report in the case the MFT project is accepted.

Chapter 1

Physics motivation

1.1 Heavy Flavour and Quarkonium Physics

1.1.1 Open Heavy Flavour in Heavy Ion Collisions

Heavy quarks (charm and beauty), and correspondingly hadrons carrying open heavy flavour, are abundantly produced in pp and heavy ion collisions at LHC energies. Heavy flavour is regarded as an important probe of the hot and dense medium produced in ultra-relativistic heavy-ion collisions. Due to the large mass of these quarks, they are only produced in the early stage of the collision and can therefore experience the full evolution of the medium itself. In particular, they are sensitive to the density of the medium through the mechanism of in-medium energy loss of heavy quarks. This effect is usually studied by means of the nuclear modification factor:

$$R_{AA}(p_T) = \frac{1}{\langle N_{coll} \rangle} \cdot \frac{dN_{AA}/dp_T}{dN_{pp}/dp_T} = \frac{1}{\langle T_{AA} \rangle} \cdot \frac{dN_{AA}/dp_T}{d\sigma_{pp}/dp_T}, \quad (1.1)$$

where $\langle N_{coll} \rangle$ and $\langle T_{AA} \rangle$ are the mean number of binary collisions and the average nuclear overlap function corresponding to the considered collision centrality class; dN_{AA}/dp_T , dN_{pp}/dp_T and $d\sigma_{pp}/dp_T$ are the production yields and cross section (σ) as a function of transverse momentum in nucleus-nucleus (AA) and pp collisions. According to QCD, quarks should lose less energy than gluons when passing through the medium. This is due to the fact that in-medium gluon radiation is expected to increase with the colour-charge of the emitting particle. The energy loss should further decrease with increasing mass, due to the so-called “dead-cone” effect [18]. Hence, gluons, which are dominating the production of light hadrons, are expected to lose more energy than quarks due to their larger colour-charge, while charm quarks will lose more energy than beauty quarks, due to the difference in mass. This should result in an ordering of the corresponding nuclear modification factors: $R_{AA}^\pi < R_{AA}^D < R_{AA}^B$. The heavy hadron production yields in heavy ion collisions could also be modified by other mechanisms, such as the collisional energy loss [19], in-medium fragmentation, recombination and coalescence [20–22]. Furthermore, initial state effects [23, 24], such as gluon shadowing/anti-shadowing, saturation, Cronin effect, could induce similar modifications

and make the interpretation of the nuclear modification factor in terms of hot medium effects more complicated.

The study of heavy flavour production in heavy-ion collisions is of the utmost interest at the LHC, where the large heavy-quark production yield should allow to simultaneously measure both charm and beauty hadrons in similar kinematic ranges and to perform a direct comparison via the so-called “double” nuclear modification factors¹. Such double ratios should be particularly sensitive to some of the features of in-medium parton energy loss [25, 26]. On the other hand, the question, whether the interaction of the partons with the medium leads to their thermalisation, can be addressed via the measurement of the elliptic flow strength of particles carrying heavy quarks. Finally, we note that a precise measurement of the total production cross section of heavy quarks in heavy ion collisions represents a reference measurement for the study of the modification of the production yield of quarkonia (charmonia and bottomonia), whose production mechanism is directly linked to the production cross section of the corresponding heavy quarks. **The study of heavy flavour at low p_T is an experimental challenge that will be addressed by the upgraded ALICE detector (see sections 1.2.1 and 2.1 in the general ALICE LoI [1] for the physics motivations).**

Heavy-flavour production in heavy-ion collisions has been investigated at RHIC by the PHENIX and STAR collaborations, which observed a strong suppression of the yield of heavy flavour decay electrons at mid-rapidity in central Au–Au collisions at $\sqrt{s} = 200$ GeV, expressed via the corresponding R_{AA} [27–30]. More recently, measurements performed at central rapidity by the CMS collaboration at the LHC showed a significant suppression of J/ψ from b -hadron decays [31].

In ALICE, the R_{AA} of D^0 , D^+ and D^{*+} mesons have been measured as a function of p_T for various collision centralities [32]. In the most central collisions (0–20%) a suppression of a factor $\sim 2.5–4$ is observed for $p_T \gtrsim 5$ GeV/c. This suppression is similar to that of π^+ within uncertainties. For $p_T \lesssim 5$ GeV/c, the D -meson R_{AA} is higher than the π^+ R_{AA} , which indicates a different behaviour of light and heavy quarks in the medium. On the other hand, the R_{AA} of mid-rapidity electrons from heavy-flavour decays shows a suppression of a factor $\sim 1.5–4$ for $p_T \gtrsim 4$ GeV/c, in the 0–10% most central collisions [4]. The centrality dependence of the R_{AA} of D^0 ($p_T > 6$ GeV/c) was compared to that of mid-rapidity electrons ($p_T > 4.5$ GeV/c) from heavy-flavour decays. In the two cases, the suppression shows a strong increase with increasing centrality, being compatible with unity for the most peripheral collisions and reaching a factor ~ 5 (2.5) for D^0 (electrons) in the 0–20% most central collisions. This could be an indication for a different interaction of charm and beauty quarks with the medium since, according to FONLL, leptons from beauty decay dominate the spectrum for $p_T \gtrsim 6$ GeV/c.

The present status of heavy-flavour measurements in Pb–Pb collisions at forward rapidity with ALICE [33] is shown in Figure 1.1. The R_{AA} of muons from heavy-flavour decays has been measured as a function of p_T in different centrality bins. A larger suppression is observed in central collisions than in peripheral collisions, with no significant p_T dependence within uncertainties. The suppression magnitude in the most central collisions is similar to that observed with electrons from heavy-flavour decays in the mid-rapidity region.

The present measurement in the forward-rapidity region suffers from being inclusive (muons from charm decays cannot be separated from muons from beauty decays) and from being limited to high p_T (because muons from pion and kaon decays, which dominate the p_T spectra at low p_T , cannot be separated from muons from heavy-flavour decays). The MFT will offer new opportunities for these measurements, by allowing to measure the production cross section of muons from charm decays and muons from beauty decays, separately, down to low p_T . The effect of the separate measurement of the charm and beauty cross sections is twofold: on the

¹ R_{AA} (heavy flavour)/ R_{AA} (light flavour) and R_{AA} (beauty)/ R_{AA} (charm)

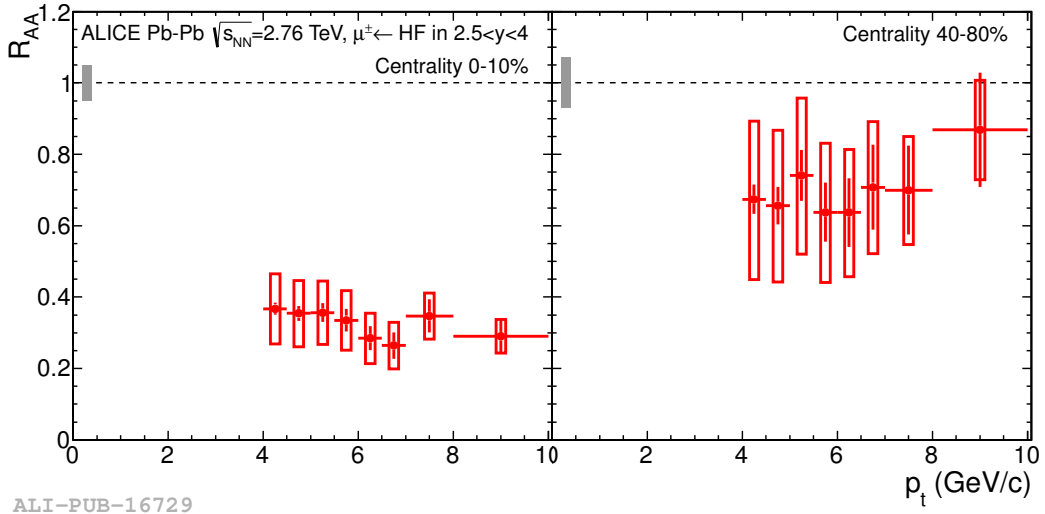


Figure 1.1: R_{AA} of muons from heavy-flavour decays in $2.5 < y < 4$ as a function of p_T , in the 0–10 % (left) and 40–80 % (right) centrality classes, in Pb–Pb collisions at $\sqrt{s_{NN}} = 2.76$ TeV. Open (full) boxes represent the systematic (normalisation) uncertainty. Horizontal bars show the bin widths. From [33].

one hand, as already remarked, it would provide an essential reference for the study of charmonium (bottomonium) suppression and/or regeneration in the quark-gluon plasma. On the other hand, measuring the charm and beauty R_{AA} (and/or R_{CP}) independently allows to test the theoretical predictions for the difference in the energy loss of charm and beauty quarks in the medium. This, together with the measurement of charm and beauty elliptic flow, will thus help us in obtaining a comprehensive understanding of in-medium parton energy loss and thermalisation.

1.1.2 Charmonium in Heavy-Ion Collisions

Quarkonium was proposed as a probe of the QCD matter formed in relativistic heavy-ion collisions more than two decades ago. The well-known prediction, quarkonium suppression due to colour-screening of the heavy-quark potential in deconfined QCD matter, has been experimentally searched for at the SPS and RHIC heavy-ion facilities [34, 35]. In particular, according to the colour-screening model, measuring the in-medium dissociation probability of the different quarkonium states is expected to provide an estimate of the initial temperature of the system. A less familiar prediction was also suggested: the enhancement of quarkonium production due to recombination of charm and anti-charm quarks occurring for sufficiently high densities of charm quarks created in the initial stages of the collisions [36]. The recombination mechanism implies the displacement of charm quarks over significant distances, and it would be a clear signal for the presence of a deconfined phase [37]. **The study of quarkonium production in heavy ion collisions at LHC energies is one of the main physics cases addressed by the letter of intent of the ALICE upgrades.** ALICE presents excellent performance to study charmonium production down to zero transverse momentum. The main motivations for quarkonium studies in ALICE are reported in the sections 1.2.2 and 2.2 of the ALICE general upgrade LoI [1]. In the present addendum we focus on the performance improvements of the ALICE detector with the MFT.

The data analysis of the first LHC run has provided many intriguing results [38–40]. The transverse momentum dependence of the nuclear modification factor as shown in Figure 1.2 is dramatically different at the LHC compared to RHIC measurements. At low- p_T the nuclear suppression is significantly reduced (i.e. larger R_{AA}) at the LHC [39] compared to RHIC [41]. Transport model

calculations reproduce the data quantitatively [42]. In current models [42, 43], about half of the low- p_T J/ψ yield in Pb–Pb collisions at 2.76 TeV is produced by the recombination of charm quarks in QGP, while the rest is due to primordial production. Both the kinetic and the statistical hadronisation models require thermalisation of the charm quarks in QGP. As a consequence they will follow the collective behaviour of the bulk QGP and their flow will be reflected in that of charmed hadrons and quarkonia. Indeed, elliptic flow of J/ψ at LHC energies was predicted within a transport model [43]. The first measurement at the LHC [40], shown in Figure 1.2, provides a tantalizing hint of a finite elliptic flow of J/ψ (the significance of non-zero flow for the centrality range 20–60 % is 2.3σ in the p_T range 2–4 GeV/c). The preliminary ALICE data are consistent with the expectation from transport models, but higher precision data are needed in order to be able to extract information on the QGP properties and on the amount of J/ψ produced via regeneration.

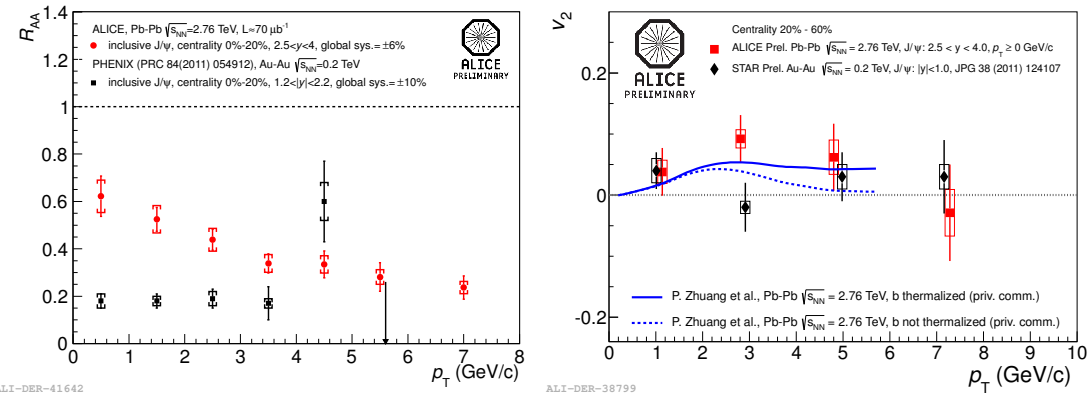


Figure 1.2: Left: transverse momentum dependence of the nuclear modification factor for the J/ψ at forward rapidity [39]. The ALICE results are compared to the PHENIX results. Right: Elliptic flow of J/ψ as a function of the transverse momentum in 20–60 % Pb–Pb collisions at 2.76 TeV [40]. The ALICE data are compared to STAR results [44].

The study of the production of $\psi(2S)$ in heavy ion collisions at the LHC is certainly a challenge for the experiments due to the small production cross section (significantly lower than that of the J/ψ) and the low branching ratio in the dimuon channel. The measurement of the $\psi(2S)$ is crucial to disentangle the different mechanism of recombination of c and \bar{c} , eventually confirming or refuting the statistical hadronisation model. The first measurements at the LHC [45, 46] comes with too large uncertainties to make any conclusion. Future measurements will be of outstanding importance to study how deconfined matter recombines into colourless heavy-flavoured hadrons.

Last but not least, the measurement of the total charm production cross section could allow to constrain the model calculations with high precision. Indeed the charm-quark recombination rate strongly depends on the initial production cross section, and therefore this measurement will be crucial to shed light on the charmonium physics at LHC.

In this respect, new crucial quarkonium measurements at forward rapidities will become accessible with the high-precision internal tracking system for the Muon Spectrometer (MFT). The MFT will allow to disentangle prompt and non-prompt quarkonium, which is decisive for the interpretation of future measurements of the J/ψ nuclear modification factor, elliptic flow and polarisation. Finally, the rejection of muons with displaced vertices by the MFT will improve the precision of the $\psi(2S)$ measurement in the most central collisions, and will allow for the first time the measurement of the $\psi(2S)$ R_{AA} as a function of the transverse momentum. All these measurements of prompt J/ψ and $\psi(2S)$ at forward rapidities will be complementary to the measurements that will be performed by ALICE in the dielectron channel at mid rapidity [1].

Although the properties of the QGP at the LHC are expected to exhibit similar initial conditions within $|\eta| \lesssim 4.0$ [16], many other effects like shadowing, energy loss, charm rapidity density, etc. could strongly vary with rapidity. In this context, measurements in two different rapidity intervals will strongly constrain theoretical models on charmonium production at LHC. At RHIC, one of the most intriguing results was the unexpected rapidity dependence of the $J/\psi R_{AA}$, pointed out by the comparison of results at mid and forward rapidities [14]: for this reason it is crucial that different rapidity domains could be measured at the LHC.

1.1.3 Bottomonium in Heavy-Ion Collisions

Bottomonium resonances are also being studied at RHIC and LHC and the measurements are complementary to those of charmonium. In particular, the beauty rapidity density at LHC is expected to be similar to that of charm at RHIC, and colour-screening of the $\Upsilon(2S)$ resonance should be similar to that of the J/ψ . Recently, the STAR and CMS experiments have performed the first measurements of Υ production in heavy-ion collisions. The STAR experiment has measured the ΥR_{AA} for the Au–Au 200 GeV 0 – 60 % centrality bin and a suppression to ~ 0.56 with a 40 % relative error [47] is observed. CMS has been able to disentangle the different Υ resonances in Pb–Pb at 2.76 TeV. A comparison of the relative yields of Υ resonances has been performed in Pb–Pb and pp collisions at the same centre of mass energy per nucleon pair of 2.76 TeV. The double ratio of the $\Upsilon(2S)$ and $\Upsilon(3S)$ excited states to the $\Upsilon(1S)$ upsilon ground state in Pb–Pb and pp collisions was evaluated and an evidence of less suppression of $\Upsilon(1S)$ compared to $\Upsilon(2S)$ and $\Upsilon(3S)$ was found [48]. **Even if the MFT will not improve the performance of ALICE for the detection of the upsilon resonances, its contribution will be nonetheless crucial to determine the open beauty reference via the golden $B \rightarrow J/\psi + X$ channel. This measurement will be unique at LHC and unique in ALICE at forward rapidities..** The possibility to perform the open beauty measurement down to zero p_T , together with the increase of LHC Pb–Pb luminosity, will considerably improve the interpretation of the ALICE Υ measurements. Please note that this measurement will be hardly done by CMS and ATLAS due to a muon p_T threshold at 3 GeV/ c .

1.1.4 The Low p_T Yield Excess in Heavy-Ion Collisions.

Two-photon and photonuclear interactions at unprecedented high energies can be studied in ultra-peripheral heavy-ion collisions (UPC) at the LHC. In such collisions the nuclei are separated by impact parameters larger than the sum of their radii and therefore hadronic interactions are strongly suppressed. The cross sections for photon induced reactions remain large because the strong electromagnetic field of the nucleus enhances the intensity of the virtual photon flux, which grows as Z^2 , where Z is the charge of the nucleus. The virtuality of the photons is restricted by the nuclear form factor to be of the order $Q^2 \approx 1/R^2 \approx 10^{-3}$ GeV 2 (R is the radius of the nucleus). The physics of ultra-peripheral collisions is reviewed in [49, 50]. Exclusive photoproduction of vector mesons, where a vector meson but no other particles are produced in the event, is of particular interest. Exclusive vector meson production in heavy-ion interactions is expected to probe the nuclear gluon-distribution [51], for which there is considerable uncertainty in the low- x region.

Recently, the first LHC measurement on exclusive photoproduction of J/ψ in Pb–Pb collisions at 2.76 TeV in the ALICE Muon Spectrometer has been published and compared with model calculations [52]. Theoretical models, which assume that the forward scattering cross section scales with the square of the number of nucleons, disagree with the measurement both for the value of the cross section and for the ratio of the two rapidity intervals, and are thus strongly disfavoured. Best agreement is found with models including nuclear gluon shadowing.

Recently, ALICE has measured an excess of the J/ψ yield at low p_T , i.e. below 300 MeV/ c , in nuclear Pb–Pb collisions at LHC energies [53]. The physical origin of this excess, shown in Figure 1.3 for

two different centrality bins, is yet to be understood and further studied with more precise data. As it was suggested by Nystrand [54], J/ψ photo-production could explain the observed excess. Indeed the J/ψ photo-production cross section could be comparable to the hadro-production one at LHC energies. In this respect, the observed excess would result from the coherent photo-production of J/ψ during the nuclear collision. Such an observation would raise fundamental questions on how the coherent photo-production could take place, since the system will further interact due to the hadronic interaction at similar time scales. Other related open question, e.g. how the photo-produced J/ψ will interact with the QGP, may be studied. The low- p_T excess will be studied with higher precision as a function of centrality [1], and the MFT could allow for a more detailed study of its origin, namely studying the contribution from non-prompt J/ψ .

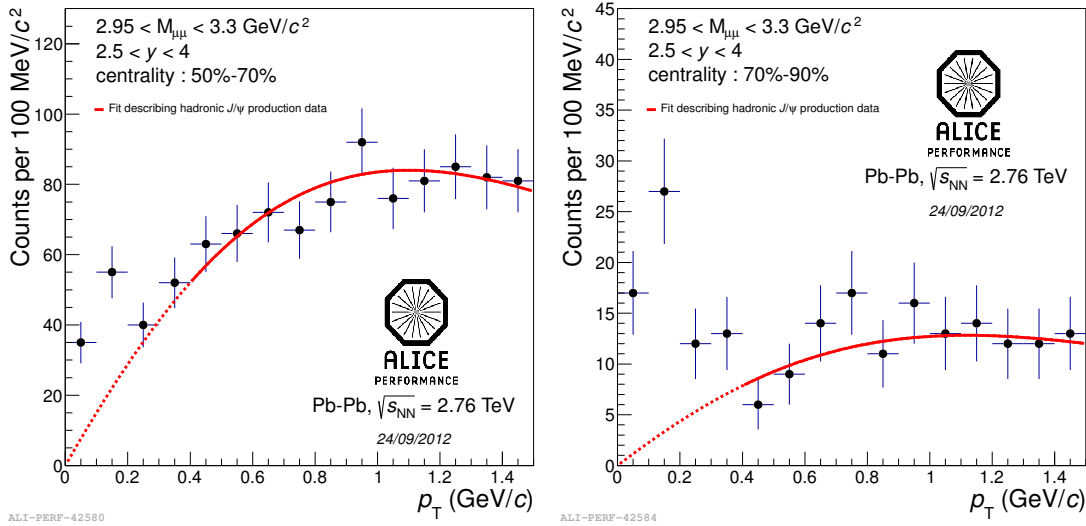


Figure 1.3: Low- p_T excess observed in the Pb–Pb at 2.76 TeV in the centrality intervals 50 – 70 % (left) and 70 – 90 % (right). The solid line is based on scaling from pp collisions [53].

1.1.5 Exotic Heavy-Flavour Studies

Searching for B_c formation in heavy-ion collisions. It is worth to mention that the MFT upgrade could open the possibility for the first observation of the B_c hadrons in heavy-ion collisions. The measurement would be extremely interesting since recombination mechanism could remarkably enhance the production of B_c mesons in heavy-ion collisions with respect to pp collisions. Indeed, the B_c would exhibit similar properties to quarkonium bound states, but with two different flavours. For this reason, the B_c lifetime is larger than the one of quarkonia ($\tau(B_c) \sim 5 \cdot 10^{-13} \text{ s}$). The most promising channel to study the B_c production in the MFT would be $B_c \rightarrow J/\psi + \mu + X$ (branching ratio of $\sim 2\%$): three muons in a displaced vertex, two of them with the J/ψ invariant mass and a third one with high p_T ($p_T > 1.5 - 2.0 \text{ GeV}/c$). At integrated Pb luminosities of 10 nb^{-1} , the equivalent nucleon luminosities are of the order of 0.5 fb^{-1} , high enough to produce a significant number of B_c hadrons.

1.1.6 Summary of MFT Motivation Related to Heavy-Flavour Physics

To summarise, new crucial measurements of heavy flavour (both hidden and open) at forward rapidities will become accessible, if the Muon Spectrometer will be upgraded with the high-precision internal tracking system (MFT) as it is proposed in the present document:

- **Prompt Charmonium.** In the present measurements of the Muon Spectrometer it is not

possible to disentangle between prompt charmonium and charmonium from b -hadron decays. As a consequence, the systematic uncertainty of the future measurements without MFT will be limited by the unknown contribution of the b -hadron to the charmonium measurements. **The MFT will allow to disentangle prompt and non-prompt charmonia.** It will be decisive for the theoretical interpretation of the J/ψ nuclear modification factor, elliptic flow and polarisation measurements.

- **Open Charm.** Charm quark production should be affected by the same cold nuclear matter effects (namely the shadowing of the gluon distribution) as charmonium production. Moreover, charm quarks do not disappear from the hot QCD matter during its hydrodynamical evolution, since annihilation is expected to be small. In this respect, the open charm production is the natural reference to study the suppression or enhancement of charmonium production in heavy ion collisions. In the ALICE Muon Spectrometer, the main contribution to the muon yield below $p_T = 2 - 3$ GeV/c results from the weak decays of light hadrons, namely charged pions and kaons. **The MFT allows the rejection of a large fraction of muons from pions and kaons, making the measurement of muons from charm-hadron decays down to $p_T = 1$ GeV/c feasible, therefore giving the possibility to measure the total open-charm cross section.**
- **$\psi(2S)$ Production.** A complete study of charmonium requires the study of J/ψ , but also of $\psi(2S)$ and χ_c . The measurement of the $\psi(2S)$ with satisfactory significance is a challenge for a heavy-ion experiment [1]. From recent ALICE analysis, the ψ' signal over background ratio (S/B) is expected (from the pp $\psi'/(J/\psi)$ ratio) to be around 0.2 % in the 0–10 % Pb–Pb collisions at 2.76 TeV. The S/B could be even smaller if the $\psi'/(J/\psi)$ ratio decreases in Pb–Pb collisions with respect to pp collisions, as it has been observed at SPS energies. Assuming a factor 4 decrease, the $\psi(2S)$ signal over background ratio could be as low as 0.05 %. Under these conditions, one would need to collect about 10 nb^{-1} Pb–Pb collisions for having a significance of 3 in the measurement of $\psi(2S) R_{AA}$ integrated over p_T in the 0–10 % central Pb–Pb collisions. An improvement of the S/B ratio is thus needed, allowing at the same time to decrease the systematic uncertainty on the $\psi(2S)$ signal extraction. In this context, **the MFT will be crucial for improving the precision of the ψ' measurement in the most central collisions allowing a p_T differential measurement**, thanks to the significant suppression of the background from pions and kaons.
- **Upsilon and Open Beauty.** The ALICE Muon Spectrometer will perform the measurement of Υ in Pb–Pb collisions in the next years. **The MFT will be crucial to determine the open beauty reference via the golden $B \rightarrow J/\psi + X$ channel.** The possibility to perform this measurement, together with the increase of LHC Pb–Pb luminosity, will considerably improve the interpretation of our Υ measurements.
- **J/ψ Low p_T excess.** The study of the origin of the recently observed J/ψ low p_T yield excess will be studied in detail thanks to the increase of the luminosity. The MFT will allow to discriminate between prompt and decay J/ψ .
- **B_c searching.** The pioneering search for B_c production in heavy ion collisions can also be performed with the MFT.

1.2 Low-Mass Dimuons in Heavy-Ion Collisions

Dileptons are important probes of the temperature and the dynamical properties of the matter formed in relativistic heavy-ion collision. Emitted at every stage of the matter evolution, they escape (almost) freely without final-state interactions; therefore, the observed dilepton spectra contain information about the entire history of the evolution. A proper disentanglement of different stages

of the collision dynamics, through an adequate analysis of these spectra, represents a challenging experimental and theoretical task. **Dilepton studies are an important physics motivation of the ALICE upgrade Letter of Intent (see section 2.3 in [1]): the MFT will improve the performance of ALICE for the measurement of dimuons at forward rapidities.**

Among the different physics topics that can be addressed, in the present document only the performance for the measurement of light vector mesons $\rho(770)$, $\omega(782)$ and $\phi(1020)$ and QGP radiation for $M_{\mu\mu} < 1 \text{ GeV}/c^2$ are presented. Other interesting physics cases, like the detection of Drell-Yan dimuon pairs [55] or the measurement of QGP radiation in the intermediate mass region $m_\phi < M_{\mu\mu} < m_{J/\psi}$ will be addressed in the future.

1.2.1 Chiral Symmetry Breaking and Restoration

Due to the small “bare” masses of light u and d quarks ($5 - 10 \text{ MeV}/c^2$), the corresponding sector of the QCD Lagrangian possesses approximate global chiral symmetry, which implies an approximate conservation of the left- and right-handedness of these quarks. Within a *naïve* quark model treatment of hadron spectra in QCD, this would imply very small (and approximately equal) masses of chiral partners.

However, the QCD vacuum has an essentially non-perturbative origin. It represents a medium filled with condensates, and hadron masses are generated through the interaction of quarks and gluons with this vacuum. Indeed, within the QCD sum rules approach, the observed masses of the hadronic ground states are satisfactorily explained in the approximation of the lowest-order quark-antiquark and two-gluon condensate contributions. The difference between the masses of chiral partners (of the order of $500 \text{ MeV}/c^2$) demonstrates the strength of the (spontaneous) breaking of the chiral symmetry, which is essentially due to the quark-antiquark ($q\bar{q}$) condensate (also known as chiral condensate).

It is expected that the condensate structure of QCD undergoes modifications at non-zero temperature and in a dense medium, resulting in the rearrangement of the hadron spectra. Indeed numerical calculations on the lattice reveal a rapid vanishing of the chiral condensate at a temperature of $T_c \simeq 160 - 190 \text{ MeV}$ (which corresponds to an energy density of about $1 \text{ GeV}/\text{fm}^3$). In the hadronic world, this would manifest as the modification of the hadron spectral functions when approaching to T_c , with eventual degeneration of the chiral partners (chiral symmetry restoration).

1.2.2 Experimental Probes

High-energy collisions of ions provide the only possibility to study *in vivo* the modification of the hadron spectral function in the hot and dense matter. The best candidates are the short-lived resonances with a lifetime comparable to – or smaller than – the lifetime of the formed medium. Further, the resonances should be analysed in channels with decay products escaping from the surrounding medium with negligible final state interaction. This is provided in the low mass region of the dilepton channel, with prominent contributions of the mesons $\rho(770)$, $\omega(782)$ and $\phi(1020)$.

The lifetimes of these vector mesons are $\tau_\rho = 1.3 \text{ fm}/c$, $\tau_\omega = 23.4 \text{ fm}/c$ and $\tau_\phi = 44.8 \text{ fm}/c$. Due to the short lifetime of $\rho(770)$, several generations of this meson would decay to the dilepton channel at different stages of the collision processes and hence its spectral function contains integrated information on the space-time evolution of the medium formed in these processes. A challenging experimental task consists in an accumulation of high statistics, along with a high accuracy (high resolution) measurement of different kinematical variables (invariant mass, transverse momenta in a large interval of their values, rapidity, relative angles) of the lepton pairs with the aim to ensure an unambiguous separation of the contribution of different sources to the observed spectra and to carry out the analysis of the individual contributions.

1.2.3 Experimental Status

Low-mass dilepton spectra in high-energy heavy-ion collisions have been measured for the first time by the CERES/NA45 experiment, one of the heavy-ion fixed-target experiments carried out in the framework of the CERN heavy ion program at the Super-Proton-Synchrotron (SPS). CERES observed in experiments with Pb–Au collisions at a beam energy of 158 AGeV that the measured yield of e^+e^- pairs in the invariant mass region $0.2 – 1.0 \text{ GeV}/c^2$ exceeded considerably the contribution of the expected reference distribution as described by the so-called hadronic cocktail. The ingredients of this cocktail are the processes involving dilepton decays of hadrons in the mass region of interest, the hadrons being (presumably) produced at the latest, freeze-out stage of the evolution of the matter formed in the heavy ion collisions. This result has been confirmed by the subsequent, higher-statistic analysis of Pb–Au collision data at 158 AGeV as well as by the measurements performed in 1999 with a 40 AGeV Pb beam.

In 200 AGeV collisions of sulphur and proton beams with a tungsten target, the HELIOS/3 collaboration observed an excess of the $\mu^+\mu^-$ pairs yield in S–W interactions relative to the p–W interactions. The excess covers a large region of dilepton invariant masses, ranging from the threshold up to the J/ψ meson mass.

More recently, the low-mass dimuon spectra in 158 AGeV In–In collisions at SPS have been intensively investigated by NA60 experiment. The measurements have been done with an apparatus combining the NA10/NA38/NA50 muon spectrometer and a pixel vertex telescope installed between the target and the hadron absorber. The matching of the muon tracks in the telescope and spectrometer, both in angular and momentum space, allowed considerable improvement of the dimuon mass resolution (up to $20 \text{ MeV}/c^2$ at the mass of the $\omega(782)$ meson) and the reduction of the combinatorial background from the simultaneous semileptonic decays of π and K mesons. In addition, it allowed a dedicated study of the open-charm decay contribution, identified on a statistical basis through the measurement of the dimuon offset with respect to the primary interaction vertex. After subtraction of the conventional sources from the high statistic data, NA60 has observed a strong excess of the yield of dimuon pairs in the whole invariant mass region $0.2 – 2.6 \text{ GeV}/c^2$.

More recently, the PHENIX experiment at the Relativistic Heavy Ion Collider (RHIC) has observed, in Au–Au collisions at $\sqrt{s_{\text{NN}}} = 200 \text{ GeV}$, a significant enhancement of the dielectron continuum in the invariant-mass region $0.15 – 0.75 \text{ GeV}/c^2$, increasing with the centrality of collisions. However, this measurement is controversial since STAR experiment has not observed such enhancement in the most central collisions. Therefore, more precise measurements are needed and will be important for the quantitative extraction of the excess.

1.2.4 Current Theoretical Scenario

A complete theoretical treatment of heavy-ion collisions represents an extremely complex problem. The main difficulty is due to the lack of detailed knowledge on the formation and evolution of the rapidly expanding medium, including the critical phenomena in this medium, such as the mechanism of chiral symmetry breaking/restoration. The latter cannot be accessed directly and has to be studied through the analysis of the spectral characteristics of the colourless resonances, which are created inside the medium and interact with it.

Several effective theoretical models have been developed, aiming to describe the low- and intermediate-mass dilepton spectra in high-energy heavy-ion interactions. The main qualitative conclusions that can be drawn from the analysis of the data of CERES/NA45, and especially from the very high-statistics and high-resolution data of NA60 can be summarised as follows. The (large) excess of the dilepton pairs in the region of invariant masses below $0.7 \text{ GeV}/c^2$ is essentially due to the broadening of the $\rho(770)$ meson in the interaction with medium, especially with its baryonic con-

stituents. The average width of the ρ meson as extracted from the NA60 data reaches the value of $\simeq 400 \text{ MeV}/c^2$ corresponding to a mean medium temperature of $\simeq 150 \text{ MeV}$. No visible mass shift is needed to explain the data. The broadening of the ρ meson when moving towards the critical temperature can be interpreted in the sense of a “melting” of the meson, which loses its individuality and becomes indistinguishable from the continuum. This might be interpreted as the onset of chirality restoration.

The other sources contributing to the observed excess spectra of dileptons are thermal emission from different hadronic states as well as from quark-antiquark annihilation. The contribution of these sources dominates in the mass region above $1.0 \text{ GeV}/c^2$.

At a quantitative level, the hadronic many-body model of Hees, Rapp and Wambach describes spectacularly well both CERES and NA60 data in the whole region of the observed dilepton mass values. The predictions of the other models agree with data in the region of masses $> 0.7 \text{ GeV}/c^2$, although they do not describe the experimental observations at lower masses.

The results of the experiments at CERN SPS and their interpretation demonstrate the importance of the investigation of the low and intermediate mass dilepton region at the LHC energies, where both lifetime and initial temperature of the formed medium are expected to significantly exceed those at the SPS energies, with $\sqrt{s_{NN}}$ changing from $\sim 20 \text{ GeV}$ to over $\sim 5 \text{ TeV}$. **The combination of the upgraded Muon Spectrometer with the proposed MFT will allow us to enhance the precision of the low- and intermediate-mass dimuon measurements via the improvement of both the invariant mass resolution and the signal over background ratio.** This, combined with the LHC efforts in providing the experiments with higher luminosities in all collisional systems, will enrich the physics program of ALICE and LHC with an important domain of the study of critical phenomena in dense and hot strongly interacting matter, including the pattern of the chiral symmetry restoration at the LHC energies – a unique possibility within the LHC experimental program.

1.3 Proton-Proton and Proton-Nucleus Collisions

The study of proton-proton and proton-nucleus collisions is of major importance to fully understand the appealing results of heavy ions at the LHC. In particular, the proton-nucleus collisions serve a dual purpose. They provide, on the one hand, baseline measurements for the heavy ion collisions. Experience from previous heavy ion programs (CERN SPS, RHIC) shows that a proton-nucleus baseline is essential for the interpretation of some of the main discoveries (e.g. quarkonium suppression, jet quenching, etc.). Cold nuclear matter effects, both in the initial state, like shadowing, and in the final state, like nuclear absorption or energy loss, would influence nuclear modification patterns in proton-nucleus and nucleus-nucleus collisions. It is generally expected, that these effects can be more easily isolated in proton-nucleus collisions and the knowledge obtained there will help to interpret nucleus-nucleus results and identify the medium-induced modifications. On the other hand, proton-nucleus program also offers unique possibilities for specific investigations in various domains of Quantum Chromodynamics (QCD).

In particular, it has been suggested that a new state of saturated gluon matter, theoretically described by the so-called *colour-glass condensate* models [56–60], may be the correct picture of the small momentum components of protons and nuclei. Gluon saturation would avoid problems with unitarity (i.e. violation of the Froissart bound), which could arise from an unlimited growth of gluon density following from linear DGLAP evolution. Quantitative knowledge of gluon saturation would be important for all predictions from QCD involving small- x partons. In addition, the qualitatively new features of this state of matter would make it fundamentally interesting in its own right. The most unambiguous way to identify gluon saturation phenomena is very likely via proton-nucleus collisions, where the gluon density is high and at the same time final state modifications should be

small.

Recent interest in high multiplicity proton-proton and proton-nucleus collisions stems from the expectations that the experimental data for these systems could be used to test various theoretical approaches developed for relativistic heavy-ion collisions. An interesting possibility is that the collective behaviour clearly seen in the nucleus-nucleus collisions may be present already in the p-A collisions, and even in the proton-proton (pp) collisions of highest multiplicity of the produced particles. These studies will help to answer the questions: How small may the system be and under what conditions it is still describable with hydrodynamics? Which observables are most sensitive to the collectivity?

On the experimental side, the LHCb detector will be able to perform high quality measurements in proton-proton and proton-nucleus collisions in the same rapidity domain as the MFT and ALICE muon spectrometer. In this respect, **the strongest physics motivation for the construction of the MFT consists of the ones related to heavy-ion collisions** (see previous sections in this chapter) that cannot be measured by the LHCb detector due to its limited segmentation. Nevertheless, it will be extremely profitable for the experimental systematic uncertainties to perform the same measurements with two different detectors and to perform measurements in nucleus-nucleus, proton-nucleus and proton-proton collisions with the same detector. In addition, one should note that in the last proton-nucleus run, ALICE collected almost a factor 10 more luminosity than LHCb and the next p-Pb run will possibly be scheduled after 2018. **The MFT would allow ALICE to perform high-quality heavy-flavour and quarkonium measurements in proton-nucleus collisions, with higher integrated luminosity than the one collected by the LHCb detector.**

Last but not least, MFT will be extremely useful to study high-multiplicity proton-proton and proton-nucleus collisions, which have attracted considerable interest recently. Indeed, the charged particle multiplicities measured in high-multiplicity proton-proton collisions at LHC energies reach values that are of the same order as those measured in heavy-ion collisions at lower energies (e.g. they are well above the ones observed at RHIC for peripheral Cu-Cu collisions at 200 GeV [61]). An indication for collective behaviour appearing already in high-multiplicity pp events might come from the observation of long-range, near-side angular correlations (ridge) in pp collisions at 0.9, 2.36 and 7 TeV with charged-particle multiplicities above four times the mean multiplicity [62]. J/ψ yields were measured for the first time in proton-proton collisions as a function of the charged-particle multiplicity density [63]. Recently, many preliminary analyses from the first LHC p-Pb run have shown intriguing results that can be explained by theoretical approaches developed for relativistic heavy-ion collisions.

Chapter 2

Performance Studies for the Muon Forward Tracker

2.1 MFT Simulation Strategy

The MFT performance presented in this chapter has been evaluated by means of Monte Carlo (MC) simulations. In the preliminary studies contained in the present document, we focused on the MFT as a device aiming at improving the ALICE muon physics. No simulations are presented concerning the MFT capabilities of interest for other ALICE physics areas: this will deserve an additional and dedicated effort in the future.

The first part of the simulations concerns the study of the global properties of the events, as well as the characterisation of the performance of the matching between the tracks reconstructed in the Muon Spectrometer – the “MUON tracks” – and the MFT clusters (which we will refer to as “global muon tracks” or simply “global tracks”) in central Pb–Pb collisions. In the second part of the chapter, once the details of the matching and global tracking procedure are settled, we move to the study of the MFT performance for the single-muon and dimuon channels of main interest for the ALICE muon physics (compared, when possible, to the physics performance achievable with the present Muon Spectrometer setup).

The following section introduces some technical details concerning the MC simulations, useful for understanding the results presented in the rest of the chapter.

2.1.1 A “Standard Setup” for the MFT

If not otherwise specified, all simulations presented below refer to a “Standard Setup” of the MFT. It is defined as an ensemble of 5 circular silicon pixel planes, each one having an effective thickness of $\sim 0.4\%$ of X_0 (Figure 2.1). The external radius of each plane is defined in such a way, that the MFT acceptance covers polar angles up to 10° for the tracks coming from the nominal interaction point, a bit larger than the nominal acceptance of the MUON spectrometer. The internal radius is limited

by the presence of the beam pipe, which imposes a minimum polar angle of approximately 3° . The parameters defining the MFT Standard Setup are summarised in Table 2.1.

Table 2.1: Dimensions and positions for the MFT planes in the MFT Standard Setup.

Plane	Int. radius (cm)	Ext. radius (cm)	Z location (cm)	Pixel pitch (μm)	Thickness (% of X_0)
0	2.5	11.0	-50		
1	2.5	12.3	-58		
2	3.0	13.7	-66	25	0.4
3	3.5	14.6	-72		
4	3.5	15.5	-76		

2.1.2 Full Simulations: the MFT in the AliRoot Framework

A description of the MFT geometry has been developed and implemented within the AliRoot framework (which is the ALICE offline official computing code) for a full simulation of the detector response. The entire flow of information, starting from the hits generated by the particles up to the reconstructed clusters of pixels on the MFT planes, has been described in AliRoot by means of dedicated C++ classes. The final stage of the full simulations is the creation of the global tracks by matching the MUON tracks reconstructed in the Muon Spectrometer to the clusters found in the MFT planes. Future developments will include a standalone tracking, aiming at reconstructing *all* the tracks in the MFT (MFT tracks), and a standalone vertexing, aiming to reconstruct the position of the primary interaction and secondary vertices including collision pile-up effects. Standalone tracking and vertexing in the MFT will provide additional information improving the event

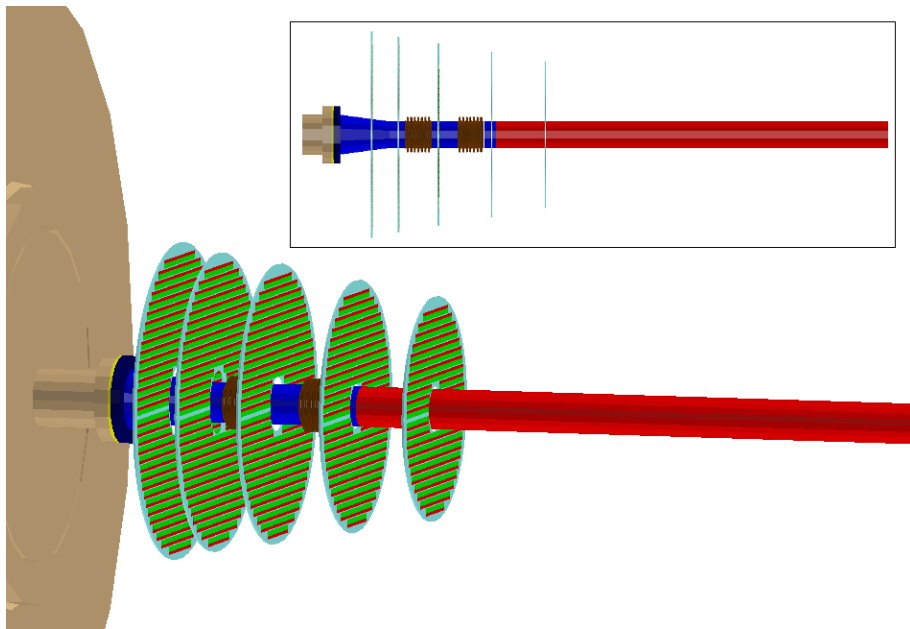


Figure 2.1: The MFT planes in a view including the beam pipe design. The Beryllium section of the pipe is shown in red, while the blue parts are the Aluminum sections connected by the Aluminum bellows (brown). Although included in the setup considered for the simulations, the VZERO detector is not shown in this figure.

characterisation, a capability of interest for the ALICE physics in general.

2.1.2.1 Plane Geometry

Each plane is composed of a disk-shaped support element, whose thickness and material can be independently set at the beginning of the simulations. The description of the support element can be found in Section 3.4. The material budget of the support planes in the performed simulations is approximately 0.3% of X_0 .

The detecting elements are designed as 8 mm high ladders of Silicon, covering the width of the support plane. The 50 μm thick Silicon sensor is made of two zones, one sensitive containing the pixels (5 mm high) and an other one inactive containing the digital part for the readout (3 mm high). The ladders are arranged in the front and back parts of the support in order to ensure a full coverage of the geometrical acceptance (see Figure 2.2). We assume the usage of CMOS technology, as discussed in Chapter 3.

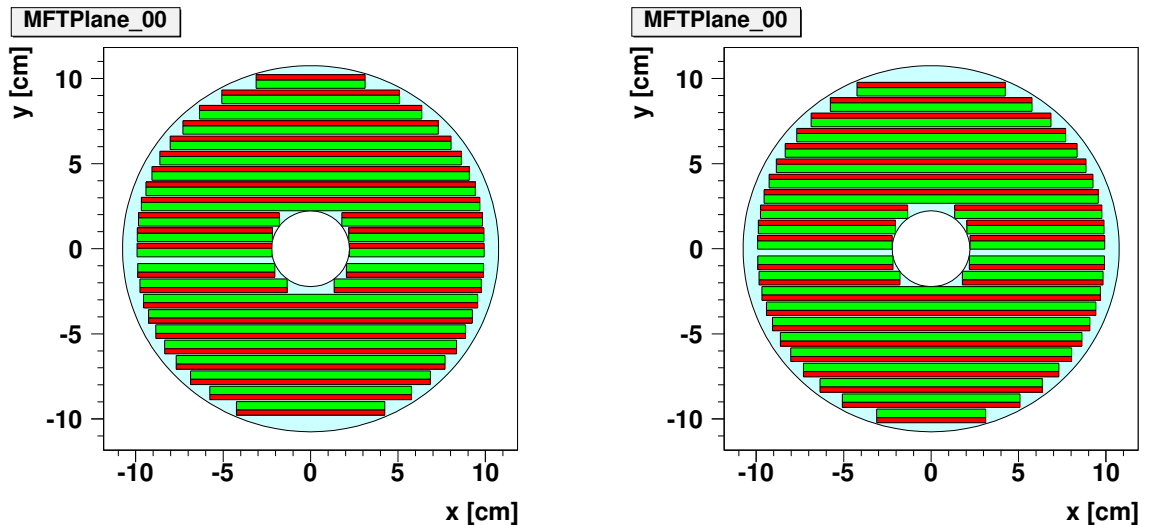


Figure 2.2: Arrangement of active (wider bands, in green) and readout (thinner bands, in red) elements in the front (left panel) and back (right panel) part of the support element.

2.1.2.2 From Hits to Clusters

A full simulation starts with the information on the position of the hits generated by each particle traversing the MFT planes. For each hit, the corresponding pixel is found by means of a virtual segmentation of the active volumes into a $x - y$ grid. Charge-sharing effects are taken into account by activating neighboring pixels – in addition to the one actually traversed by the tracked particle – whose charge collection diodes fall within a given radius from the hit (25 μm by default, resulting from preliminary investigations on the CMOS sensors). The average number of fired pixels per detected particle is 4.

Since the same pixel may be fired by more than one particle, a further stage is needed, named *digitisation*, in which the pixels' list is cleaned from multiple counting. The next stage is the *clusterisation*, in which adjacent pixels are grouped together into clusters (or reconstruction points) which will be actually exploited in reconstructing the particles' tracks. For each cluster, the centre along x and y is defined as the average between the centres of the pixels composing the cluster. The error associated with the position of the centre is defined as the RMS of the distribution of the centres of the pixels composing the cluster.

2.1.2.3 Global Fit Strategy

The tracking strategy, aiming at recovering the global muon tracks, starts from the MUON tracks reconstructed in the Muon Spectrometer. They are extrapolated back to the vertex region, taking into account both the energy loss and the multiple scattering induced by the hadron absorber. Each extrapolated track is then evaluated at the last plane of the MFT (closest to the absorber) and its compatibility with every cluster of this plane is checked according to standard track-to-cluster χ^2_{clust} . For each compatible cluster (i.e. with χ^2_{clust} not exceeding a predefined cut value), a new candidate track is created, whose parameters and their uncertainties are updated with the information given by the added cluster, by means of a Kalman filter algorithm. Each candidate track is then extrapolated back to the next MFT plane, where a search for compatible clusters is performed in the same way as before. As the extrapolation proceeds towards the vertex region, the uncertainties on the parameters of the extrapolated tracks become smaller, the number of compatible clusters decreases and the number of candidate tracks converges. If more than one final candidate is found at the last extrapolation, the best one is chosen according to the global fit quality.

2.1.3 Fast Simulations for the MFT

Fast simulations are only able to estimate the offset resolution of the muon tracks with respect to their production vertex. This approach has two main limitations:

- As long as the single muons are concerned, the impact on the physics performance in a given physics channel cannot be directly accessed: to do that, in fact, one would need to weight the performance for single muons by their expected kinematic distributions, including every possible correlation in case of dimuon signals.
- No possible effect of fake matching between the extrapolated MUON tracks and the MFT clusters can be accounted for.

Within the performance studies for the MFT, we only exploited fast simulations to compare the offset resolutions for single muons of different detector setups. This enabled us to better understand, without dealing with slow, full simulations, the role of several parameters such as the pixel size along x and y , the thickness of the MFT planes, their number and position, the thickness of the beam pipe.

2.2 Global Event Properties

In this section we focus on those global event properties having a major role in determining the MFT performance.

2.2.1 Expected Interaction Rates and Pile-up

The interaction rate currently foreseen for Pb–Pb collisions after the LHC long shutdown 2 of 2017/2018 is 50 kHz, corresponding to one minimum bias interaction every 20 μs . This translates, considering a readout time of $\sim 10 \mu\text{s}$ for the MFT planes based on the CMOS technology, to $\sim 39\%$ pile-up interactions integrated within a recorded event on top of the triggered collision.

In order to work within safety margins, the MFT performance presented in the present document is evaluated considering 2 HI JING 0–10% central Pb–Pb interactions integrated by the MFT within the same recorded event. In this case, the “main collision” is simulated with the primary vertex in the nominal interaction point, while the piled-up collision is simulated to have its primary vertex distributed according to the expected LHC parameters.

The integrated luminosity assumed in the present document is 10 nb^{-1} , expected to be achieved in few years of data taking in the high-luminosity Pb–Pb scenario after 2018. Considering a hadronic Pb–Pb cross section of 7.7 b , this corresponds to $7.7 \cdot 10^{10}$ minimum bias Pb–Pb collisions, or $7.7 \cdot 10^9$ of the 0–10 % most central Pb–Pb collisions.

2.2.2 Occupancy of MFT Planes

The occupancy of the MFT planes plays a crucial role in determining the MFT performance. A sample of 1000 central Pb–Pb events was considered in order to evaluate it. Figure 2.3 shows the observed cluster multiplicity as a function of the (absolute) z position of the MFT planes: for each point, the uncertainty corresponds to the RMS of the corresponding multiplicity distribution.

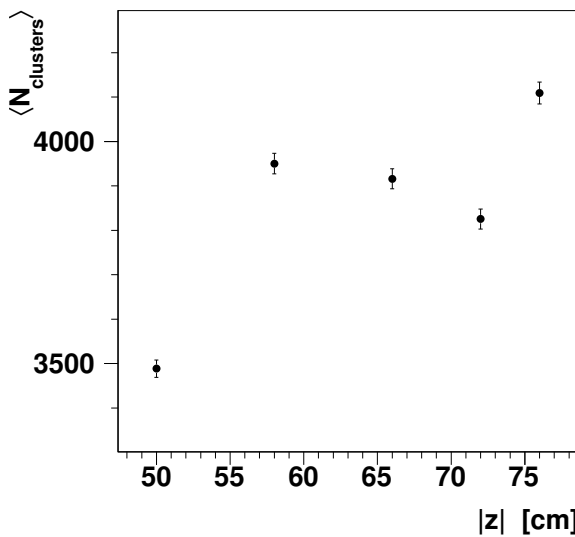


Figure 2.3: Cluster multiplicity in the MFT planes for a single central Pb–Pb interaction.

The spatial distribution of the MFT clusters is also an important aspect to be properly accounted for, its importance being evident especially in establishing and optimizing the detector design. The first MFT plane is the one having the highest cluster density. Figure 2.4 presents the spatial distribution of the cluster density for the first MFT plane as a function of the transverse (x, y) position or versus the radial position for a single central Pb–Pb interaction.

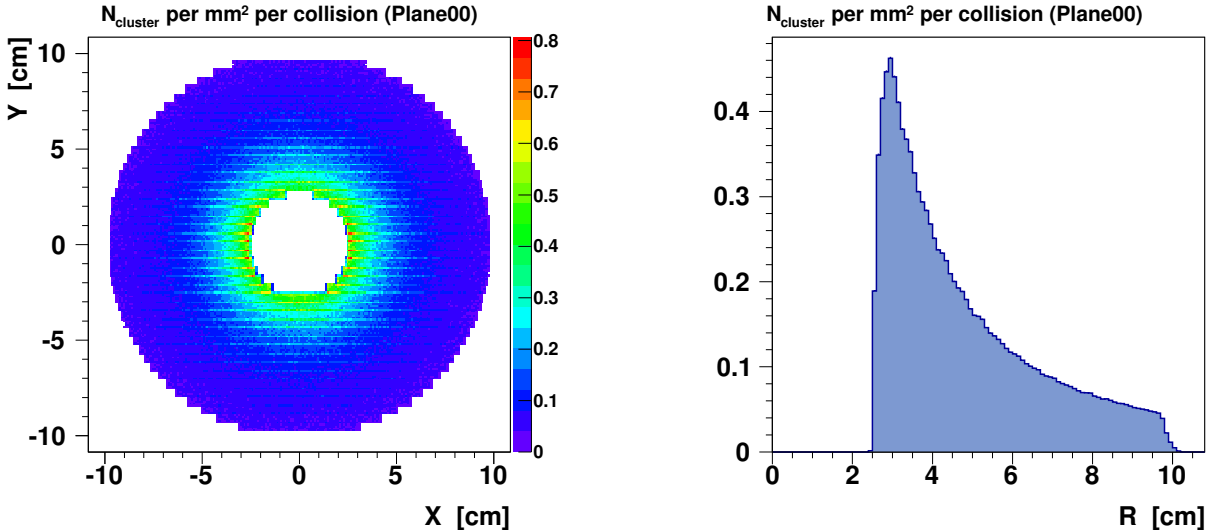


Figure 2.4: Cluster density per central Pb–Pb event in the first MFT plane as a function of the transverse (x,y) position (left) and as a function of the radial position (right). Hits from both plane sides are superimposed in the same histogram, the sensor overlaps explain the horizontal structures seen on the left panel.

2.3 Global Fit Performance for the Single Muons

Before discussing in details the MFT performance for the physics cases of major interest, we focus in this section on the characterisation of the global fit performance for single muons. Three main aspects will be considered here:

- the phase space coverage for the global muon tracks;
- the correct matching efficiency as a function of the muon kinematics;
- the pointing resolution of the global muon tracks.

2.3.1 Phase Space Available

The analysis of the $y^\mu - p_T^\mu$ phase space coverage has been performed considering both the totality of the reconstructed tracks, and the sub-sample of the tracks reconstructed with a perfectly¹ correct match between the MUON track and the MFT clusters. Positive and negative muons with uniform distribution in $-4.5 < y^\mu < -2.0$ and $0 < p_T^\mu < 10$ GeV/c were generated and embedded in two underlying central Pb–Pb events simulated using HIJING generator. The muon origin is imposed to be at the vertex $(0, 0, 0)$ of the “main collision”. The resulting reconstructed muon track distribution in the $y^\mu - p_T^\mu$ plane reflects the acceptance for the global muon tracks.

As it can be seen on Figure 2.5, the coverage of the correctly matched muon tracks is confined in the rapidity range $-3.6 < y^\mu < -2.5$, which approximately corresponds (taking absolute values for the polar angles) to $3.1^\circ < \theta < 9.4^\circ$. A minimum reachable p_T^μ of ~ 0.5 GeV/c at smaller polar angles, increasing to ~ 1 GeV/c at larger angles (lower rapidities) is resulting from the cut on the muon momentum imposed by the hadron absorber in front of the tracking chambers.

¹ The five clusters attached to the track are coming from the tracked muon.

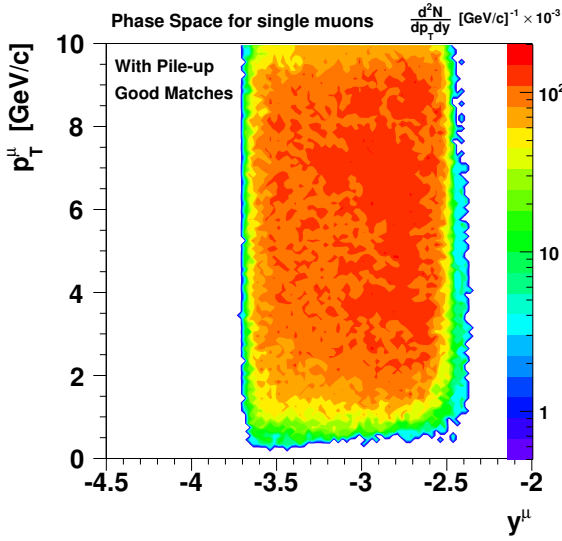


Figure 2.5: Phase space coverage of single muons having a correct match between muon track and MFT clusters. The colour scale gives, for a reconstructed muon, the probability of occurrence of the kinematics (p_T -y) per unity of p_T and rapidity.

2.3.2 Correct Matching Rate

The basic condition for the MFT to improve the physics performance of the current Muon Spectrometer, is the ability to correctly match each MUON track (or, at least, the ones composing the signals we are interested in) to its MFT clusters. For this reason, a quantity of major interest in evaluating and characterising the detector performance of the MFT is the correct matching rate between the MUON tracks and the MFT clusters.

It should be remarked that in the present study no attempt to subtract fake matches was performed: in the considered approach, fake matches are retained in the analysis as a part of the signal (and the background) having degraded kinematics. Nevertheless, the correct matching rate can be regarded as a simple and effective tool giving a crude estimate – independent of the physics process considered – of the overall quality of the MFT global performance.

The fraction of correct matches among all is shown in the top left panel of Figure 2.6, while in the top right the correct matching rate is shown as a function of p_T^μ in four slices of rapidity. As expected, the correct matching rate increases when increasing the p_T^μ and, by a lesser extent, when going from forward to more central rapidities. Independently of the rapidity, the correct matching rate falls below $\sim 50\%$ for $p_T^\mu \lesssim 1 \text{ GeV}/c$.

As can be reasonably expected, the probability for a track to be correctly matched also depends on the cluster density on the MFT planes. For this reason, the correct matching rate has been also evaluated in the case, in which no pile-up collisions are integrated in the readout time of the main one. The result for this case is shown in the centre panels of Figure 2.6. By taking the ratio between the correct matching efficiency in the cases with and without pile-up, we can evaluate the role of the cluster density on the correct matching efficiency. The result is shown in the bottom panels of Figure 2.6. Here it can be noticed that the correct matching rate varies by less than $\sim 5\%$ above $p_T^\mu \sim 3 \text{ GeV}/c$ decreases by $\sim 20\%$ for $1 \lesssim p_T^\mu \lesssim 3 \text{ GeV}/c$ and by $\gtrsim 30\%$ for $p_T^\mu \lesssim 1 \text{ GeV}/c$.

2.3.3 Pointing Accuracy

The offset with respect to the primary vertex is defined, for a single muon, as the transverse distance between the primary vertex and the muon track. The offset resolution is a crucial parameter to characterise the pointing accuracy gained by the muon global tracks thanks to the matching between the MUON tracks and the MFT clusters. A good offset resolution will allow a separation of the muons according to the processes generating them, since different muon sources typically show different offset distributions; furthermore, a good pointing accuracy will be the basis for developing reliable

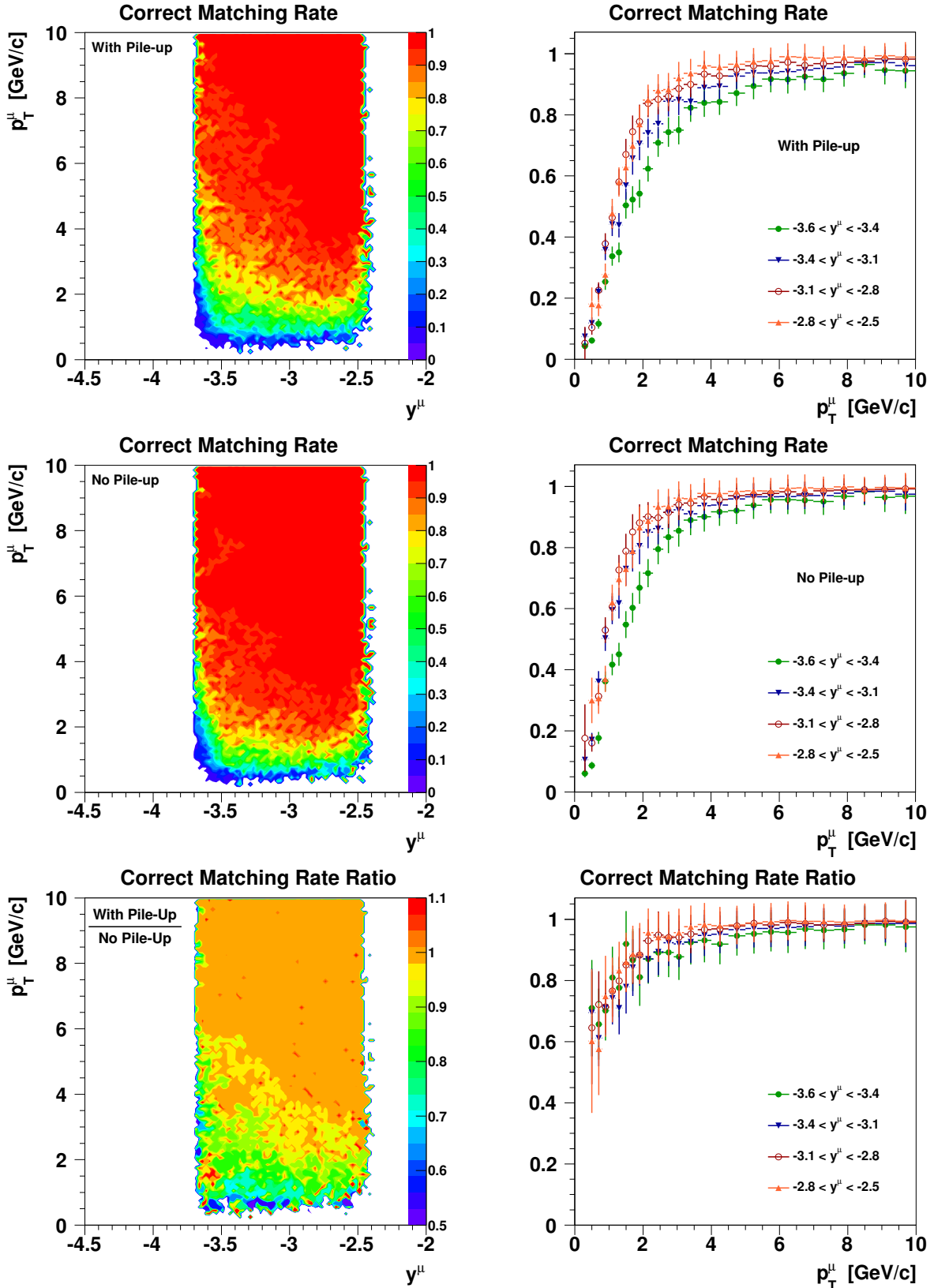


Figure 2.6: Correct matching rate for single muons in the case of two central $Pb-Pb$ events piled up (top panels) and in the case of a central $Pb-Pb$ collision without pile-up effects (centre panels). In the bottom panels, the ratio between the two scenarios is shown.

standalone MFT tracking and vertexing procedures.

To investigate the MFT performance in terms of the offset resolution for single muons, these latter were generated at a fixed position in space at $(0, 0, 0)$. The offset of the reconstructed muon tracks was then evaluated assuming the production vertex to be measured by the ALICE Internal Tracking System (ITS) with a precision of $50 \mu\text{m}$ along the x , y and z directions: this uncertainty will then propagate to the measurement of the muon offset. It should be noted that this is the most conservative estimate of the vertex position resolution for events with only a few tracks in the ITS acceptance. For central Pb–Pb collisions the ITS will provide the vertex with precision better than 5 microns.

2.3.3.1 Fast Simulations

As a first point, the offset resolution has been studied as a function of two detector parameters affecting the offset resolution of the muon tracks, namely the pixel size and the plane thickness. This study allowed us to establish a trade-off between the envisaged physics performance and the imposed technological constraints. Since various configurations of the MFT setup are concerned here, fast simulations were used to perform the analysis. Results were extracted for four combinations of p_T^μ and rapidity, ranging from low p_T^μ ($p_T^\mu \sim 0.7 \text{ GeV}/c$) and low rapidity ($y^\mu \sim -3.6$), to high p_T^μ ($p_T^\mu \sim 4.0 \text{ GeV}/c$) and high rapidity ($y^\mu \sim -2.6$). The results are shown in Figure 2.7.

The sensitivity of the offset resolution to the pixel size is small. However, a pixel size smaller than $30 \mu\text{m}$ is mandatory to keep enough pointing accuracy at low p_T^μ . This is crucial for the open heavy flavor study in single muon and our availability to measure charm and beauty to the lowest possible p_T as well as for the low mass vector meson analysis where the signal of interest is located at low p_T . The thickness of the planes plays the major role as expected because of multiple scattering. Since the offset improvement is more important for low p_T^μ , priority should be given to the minimisation of the thickness of the MFT planes. As already stated, the standard setup of the MFT, adopted throughout the present document, has a pixel size of $25 \mu\text{m}$ and a plane thickness of 0.4% of X_0 .

2.3.3.2 Full Simulations

Although fast simulations represent an effective and fast tool to easily compare the performances of various detector setups, a realistic evaluation of the offset resolution can only be performed by means of full simulations.

The observed offset resolutions are shown in Figure 2.8, plotted as a function of p_T^μ for more forward and more central rapidities. The left panel is relative to the case in which no additional Pb–Pb collision piles up on the top of the main one, and the residual misalignment of the MFT planes is equal to zero. Values as large as $110 \mu\text{m}$ are observed for $p_T^\mu \sim 0.5 \text{ GeV}/c$, while at high p_T^μ the offset resolution saturates at $\sim 50 \mu\text{m}$, i.e. determined entirely by the assumed vertex resolution. When a realistic residual misalignment of $\sim 15 \mu\text{m}$ is taken into account, these values rise by $\sim 10 \mu\text{m}$, with no significant differences observed between the scenario without and with an additional central Pb–Pb collision piled up on top of the main one.

The observed values suggest, as it will be discussed in the next sections, that the MFT is able to perform a reliable separation between muons coming from charmed and beauty mesons ($c\tau \sim 150 \mu\text{m}$ and $c\tau \sim 500 \mu\text{m}$, respectively), allowing a proper measurement of open charm and open beauty production. In the same way, identification becomes possible for charmonium production coming from b -hadrons decays. Discrimination is also provided between muons from prompt sources and muons from semi-muonic decays of pions and kaons, of capital importance in the analysis of low mass dimuons, where the signal of interest is purely prompt.

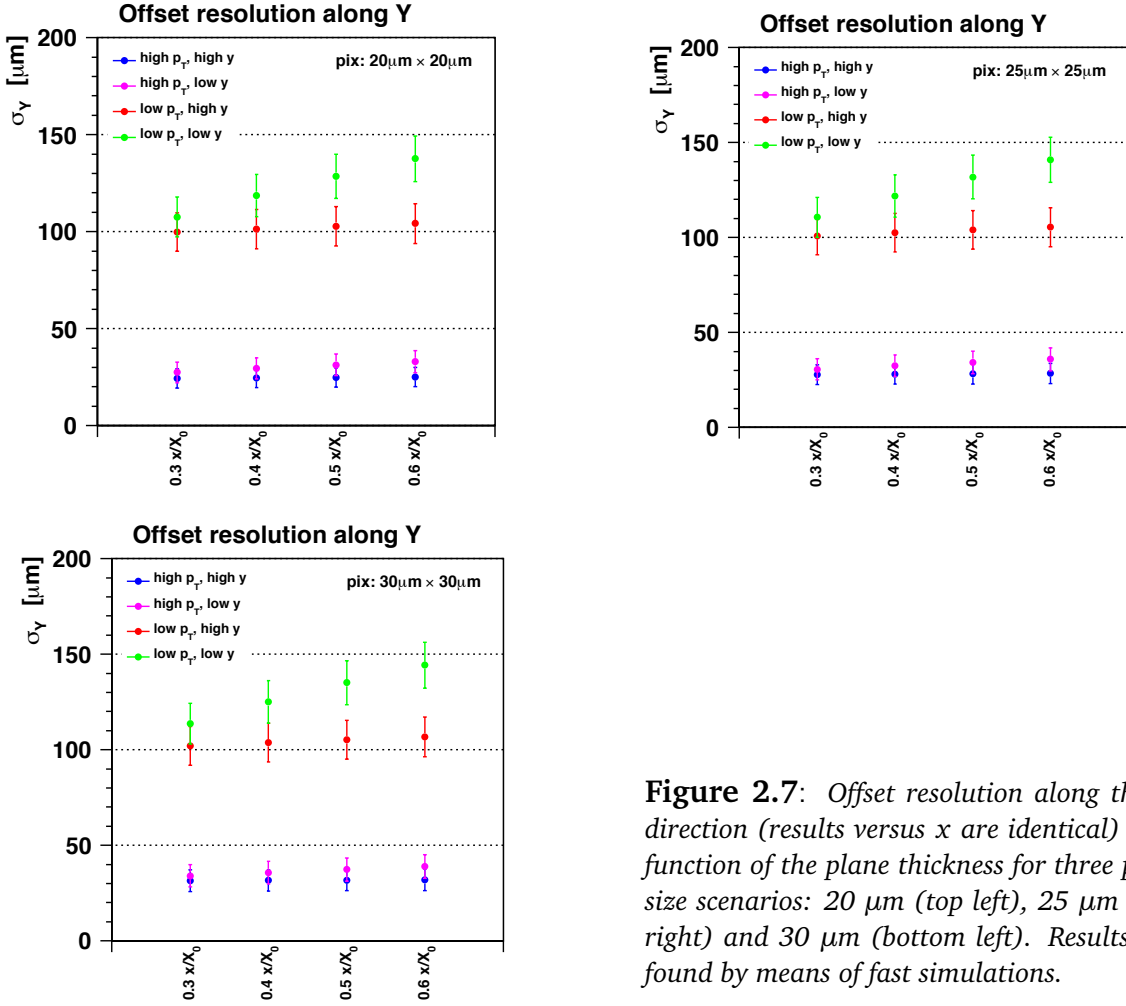


Figure 2.7: Offset resolution along the y direction (results versus x are identical) as a function of the plane thickness for three pixel size scenarios: 20 μm (top left), 25 μm (top right) and 30 μm (bottom left). Results are found by means of fast simulations.

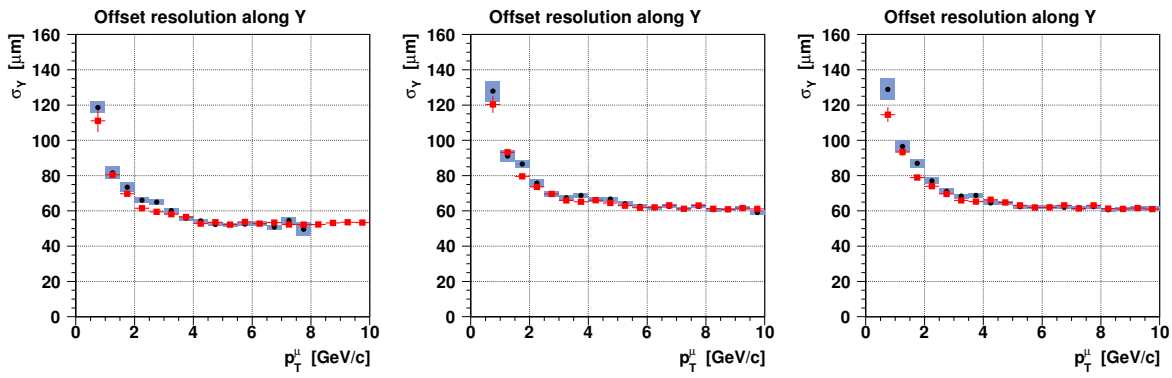


Figure 2.8: Offset resolution along the y direction (results versus x are identical) as extracted from full simulations: without pile-up and zero residual misalignment (left), without pile-up and with realistic 15 μm misalignment (centre), with pile-up and realistic 15 μm misalignment (right), no matching requirement is applied. Resolution is given for tracks with $\eta < -3.2$ (blue) and with $\eta > -3.2$ (red).

2.3.4 Prospects for the MFT Standalone Tracking

As already mentioned, every charged particle produced in the angular acceptance of the MFT will produce a hit on the tracking planes. Tracks can be then reconstructed by developing a standalone tracking strategy, based on the knowledge of the MFT clusters alone, in the same way as for the current and the future ALICE ITS.

The final standalone strategy for the MFT, expected to give a fast, efficient and reliable track reconstruction procedure, is still being defined. Various techniques are currently being investigated, in order to understand the one best suited to cope with the specific MFT requirements. Among them, we can cite at least the two most promising ones:

- The cellular automaton algorithm, developed in the framework of the HERA-B Collaboration. This algorithm has also been chosen to serve as tracking algorithm for the future CBM Experiment [64, 65], whose major experimental challenge is posed by extremely high reaction rates of up to 10^7 events per second, with the detectors integrating up to ~ 700 tracks in a central Au-Au collision.
- An adaptive method, exploiting the pattern recognition capabilities of the neural networks [66].

Apart of the possibility of performing precision multiplicity measurements at forward rapidities up to central Pb–Pb collisions, the reconstruction of the MFT standalone tracks would provide an alternative method for the global muon track finding, based on the direct match of the MFT and MUON segments of the same global track. We should however emphasise that, while providing a useful cross-check for the MUON–MFT association, this alternative tracking strategy is not expected to improve further the MUON–MFT correct matching rate presented in this document: this is due to the fact that the matching performance is already at the limit determined by the number of non-muon tracks in the vertex region, appearing in the cone of the MUON track extrapolation through the hadron absorber.

These and other applications will be investigated in detail once the final choice for the MFT standalone algorithm has been made.

2.4 Charmonium States in Central Pb–Pb

The measurement of heavy quarkonia at forward rapidities in heavy-ion collisions represents a major topic of the experimental program of the ALICE Muon spectrometer. We recall here that the ALICE capability to study J/ψ and the ψ' down to zero p_T represents a unique feature at the LHC. In this section we discuss how the introduction of the MFT in the ALICE setup may improve the analysis of charmonium states, namely the J/ψ and the ψ' resonances by:

- allowing to disentangle prompt and displaced quarkonium production;
- reducing the uncertainties on the extraction of the ψ' signal.

2.4.1 Signal and Background Simulations

Both the J/ψ and the ψ' prompt signals are simulated by means of a parametric generator. Displaced J/ψ production from b -hadrons decays is simulated using PYTHIA with the “Perugia0” tune. Simulations of complete HIJING events are used to estimate the background sources with their appropriate yields and kinematic distributions: every possible muon pair is considered, event by event,

disregarding the origin of the muons (with the exception of the muons coming from neutral resonances – i.e. the signal we are interested in – which are discarded when building the background pairs).

2.4.2 Cuts and Selections

In order to reject as much background as possible, we adopt cuts both at the single muon and dimuon levels. For single muons, we impose the matching between the muon track and a muon trigger tracklet at the *low- p_T* level ($p_T^\mu \gtrsim 1 \text{ GeV}/c$). Additionally, a sharp cut at $p_T^\mu > 1 \text{ GeV}/c$ is added, improving the quality of the matching between MUON tracks and MFT clusters. Finally, a cut on the track χ^2 (evaluated as the average χ^2 of the MUON and MFT clusters composing the track) is applied, namely $\chi^2 < 1.5$.

In addition to single muon cuts a cut at the dimuon level is applied. The Point of Closest Approach (PCA, see Figure 2.9) of the two muons is found, and the probability that both muons are coming from this point is evaluated applying a topological vertex finder method [67]. The probability $P(\vec{v})$ that the common vertex exists at location \vec{v} is evaluated by:

$$P(\vec{v}) = \sum_{i=0}^n f_i(\vec{v}) - \frac{\sum_i f_i^2(\vec{v})}{\sum_i f_i(\vec{v})}, \quad (2.1)$$

with Gaussian weight defined for each track:

$$f_i(\vec{v}) = \exp \left[-0.5(\vec{v} - \vec{r}_i)^T V_i^{-1} (\vec{v} - \vec{r}_i) \right] \quad (2.2)$$

where \vec{r}_i is the point of closest approach of track i to the PCA point \vec{v} , and V_i is its covariance matrix at point \vec{r}_i . In the following we will refer to the probability defined by Equation 2.1 as *PCA quality*.

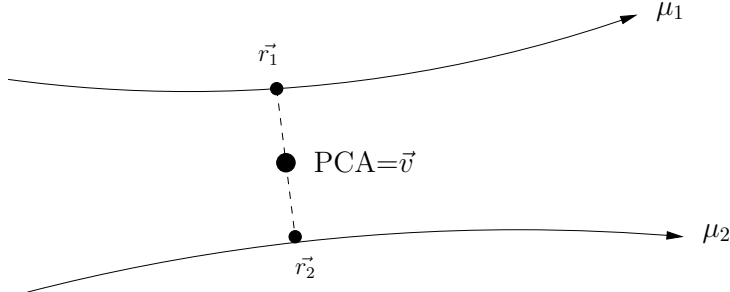


Figure 2.9: Schematic of Point of Closest Approach (PCA) definition.

For the charmonium analysis, we will use a cut on PCA quality value in order to improve the selection of dimuons coming from charmonium states, where both muons come from the same vertex, with respect to background dimuons, whose muons do not share the same origin. This cut presents a clear advantage compared with a cut on single muon or dimuon offset, because the PCA quality is independent on the relative position of the primary and charmonium vertices (which is different in the case of prompt and displaced production): this allows us to apply the same cut for both prompt and displaced charmonium analyses.

In order to establish an appropriate value for the cut on the PCA quality, we compare the PCA quality distributions (normalised to unity) for the dimuons coming from prompt J/ψ and $\psi', J/\psi$ from b -hadrons and background (top-left panel of Figure 2.10). In addition, for the three signal sources, we explicitly compare the PCA quality distributions for the full dimuon sample and for the sub-sample composed by two correctly matched muons, see top-right and bottom panels of Figure 2.10 (the

ratio between the number of good matches and the full sample is preserved in the scaling). As one can see, PCA quality proves to be a very powerful variable to remove a significant part of the background dimuons, as well as to select the fraction of the signal having two correctly matched muons. By comparing the PCA quality distributions for background, total and correctly matched signal, we decided to retain for the analysis only dimuons having their PCA quality larger than 0.6.

2.4.3 Background Rejection

The efficiency of the chosen cuts can be evaluated by comparing the fraction of rejected dimuons (the “rejection power”) for the signal and background sources. We consider the dimuon p_T dependence of the rejection power, in order to evaluate the impact on the physics topics we are interested in. The rejection power of the combined MUON spectrometer based cuts (tracker-trigger matching and

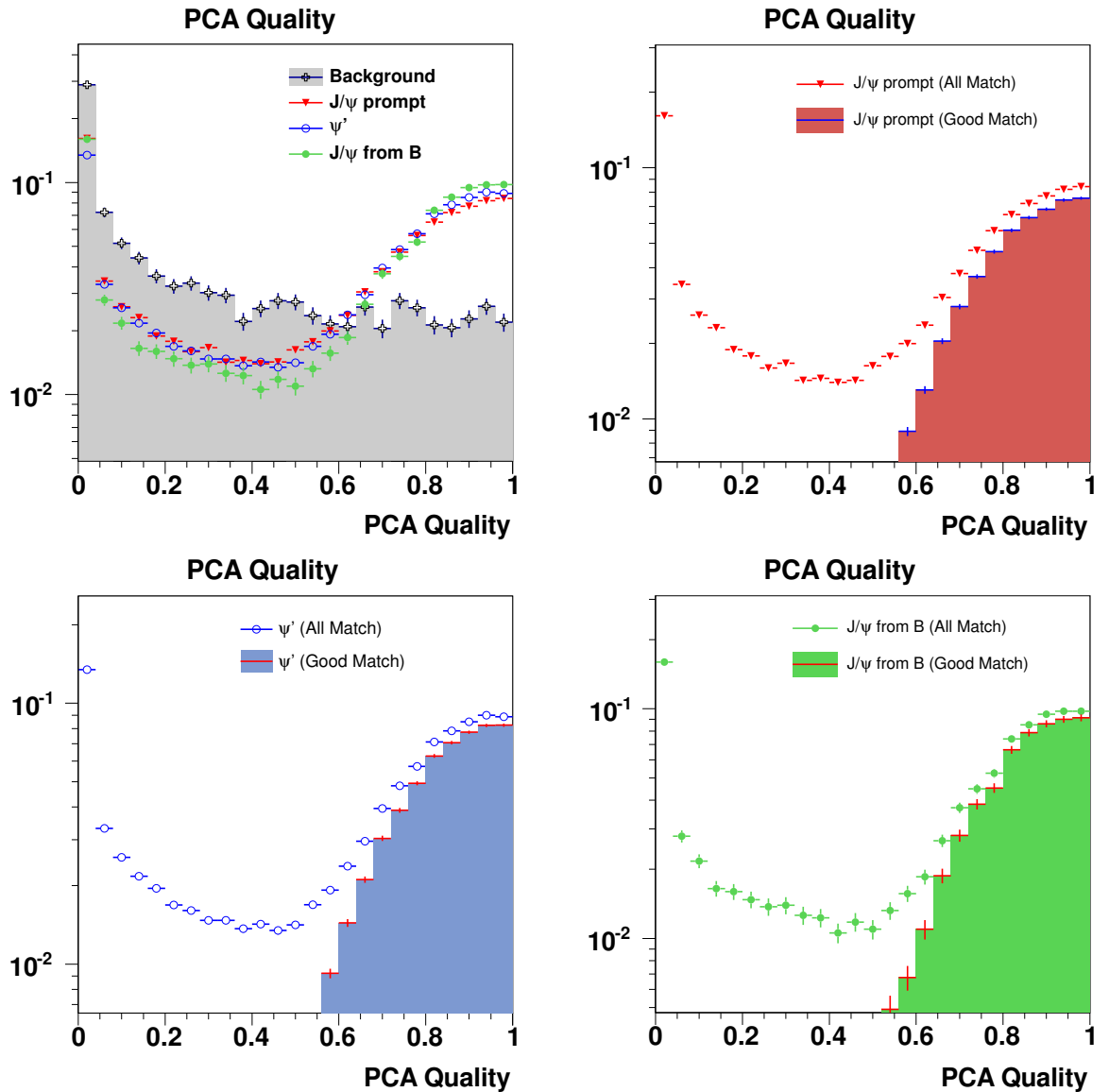


Figure 2.10: PCA quality distributions expected in 0–10 % Pb-Pb collisions at $\sqrt{s_{\text{NN}}} = 5.5 \text{ TeV}$, for background and signal dimuons. Vertical axis is always in arbitrary units. Details can be found within the text.

p_T cut) is shown in the left panel of Figure 2.11. As expected, we have a more powerful rejection for the dimuons coming from the background sources, than for the ones coming from the J/ψ and the ψ' .

The right panel of Figure 2.11 shows the additional rejection power when requesting the MFT based cuts (cut on single muons χ^2 and dimuons having a PCA quality greater than 0.6). Here, too, the rejection is found to be stronger for background than for signal dimuons.

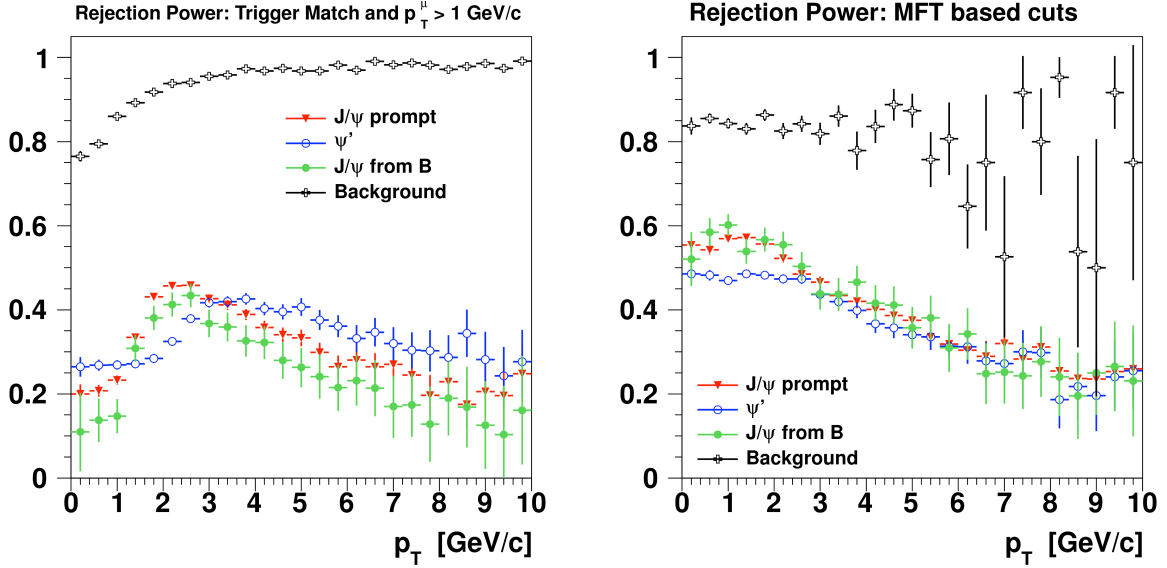


Figure 2.11: Rejection power as a function of dimuon p_T expected in 0–10% Pb–Pb collisions at $\sqrt{s_{NN}} = 5.5$ TeV, for signal and background pairs, due to the combined Muon spectrometer based cuts (left panel) on tracker-trigger matching and p_T , and the MFT based cuts (right panel) on the dimuon PCA quality and single muon χ^2 .

2.4.4 Expected Yields and Signal Extraction

In this section we summarise the expected values for the yield, the signal/background (S/B) ratio and the significance of the inclusive charmonium production. For the inclusive production the two scenarios with and without MFT are compared, while for the J/ψ production from b -hadrons the only available scenario is the one with the MFT. All estimates assume an integrated luminosity of 10 nb^{-1} and 0–10% most central Pb–Pb collisions.

2.4.4.1 Inclusive Charmonium Production

The yield of charmonia is determined to be $\sim 7.7 \cdot 10^9$ for 0–10% most central Pb–Pb events, assuming binary collision scaling (~ 1600 binary collisions in central Pb–Pb interaction [68]) with $\sim 5 \cdot 10^{-4} J/\psi$ per binary collision. The latter value corresponds to $\sim 30 \mu\text{b}$ for the J/ψ cross section in pp [69] and $\sim 60 \text{ mb}$ for the inelastic pp cross section [70]). We note that this is a rather conservative assumption, since for the J/ψ cross section in pp at $\sqrt{s} = 5.5$ TeV, values up to about $40 \mu\text{b}$ are predicted by theoretical models [71]. The yield for the ψ' is obtained by scaling the one of the J/ψ by a factor 0.14, as determined from various pp and p–A measurements [1].

These yields must be corrected for the nuclear modification factors R_{AA} expected in central Pb–Pb at $\sqrt{s_{NN}} = 5.5$ TeV. In this case, neglecting any possible dependence on p_T , the following scenario is

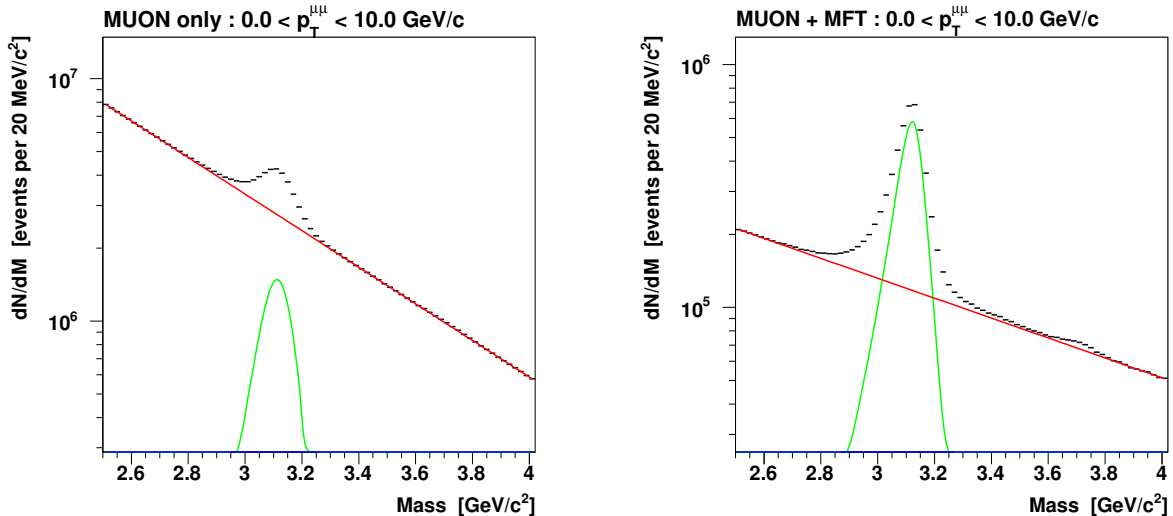


Figure 2.12: Dimuon mass distribution in the charmonium region integrated in p_T , for 0-10 % Pb-Pb collisions at $\sqrt{s_{\text{NN}}} = 5.5 \text{ TeV}$, normalised to the expected statistics in a 10 nb^{-1} integrated luminosity scenario without the MFT (left) and with the MFT (right).

assumed: $R_{\text{AA}}(J/\psi) = 0.7$ and $R_{\text{AA}}(\psi') = 0.3$;

Finally, to translate the expected 4π yields into the number of resonances observed in realistic experimental conditions, we estimate the acceptance and reconstruction efficiency factors with dedicated MC simulations, in the various p_T ranges of interest. In this case, the two scenarios with and without MFT are separately accounted for, leading to (slightly) different mass distributions and (largely) different acceptance and reconstruction efficiency factors.

The yield of background dimuons is estimated by measuring the number of dimuons per event reconstructed from the HIJING simulations. Multiplying this number by the number of events, we get the total background yield for the given integrated luminosity. Here, too, the two scenarios with and without MFT are separately considered.

The mass distributions for the signal and the background, as estimated by means of the MC simulations, are normalised to the expected yield. In order to have realistic statistical fluctuations in the final samples, the original mass distributions coming from the MC simulations are parameterised with custom functions (for the two resonances, in particular, a variable width Gaussian has been used) and new mass distributions are then created by sampling these parameterisations.

The global mass spectra in the $2.5 - 4.0 \text{ GeV}/c^2$ mass region, obtained by adding up the parameterised J/ψ and ψ' signals and the background, are shown for both scenarios without and with MFT (Figure 2.12). As one can see, adding the MFT implies two main effects:

- a global loss of statistics, both for the signal and the background;
- an improvement of the S/B ratio for both the J/ψ and the ψ' , this latter becoming visible even before any background subtraction.

To characterise more quantitatively our capability of extracting the inclusive J/ψ and ψ' signals, we isolated the two signals, separately, by subtracting the other two components from the inclusive distributions. In doing so, we propagate to the isolated signal both the statistical and systematic uncertainties on the subtracted components (i.e. on the background, the superposition between the two peaks being negligible). The profile of the signal we are looking for is “dressed” with its

appropriate uncertainties, allowing us to appreciate even by eye the sensitivity to its measurement. An example is shown for the ψ' in Figure 2.13 for the $0 - 10$ GeV/c p_T range.

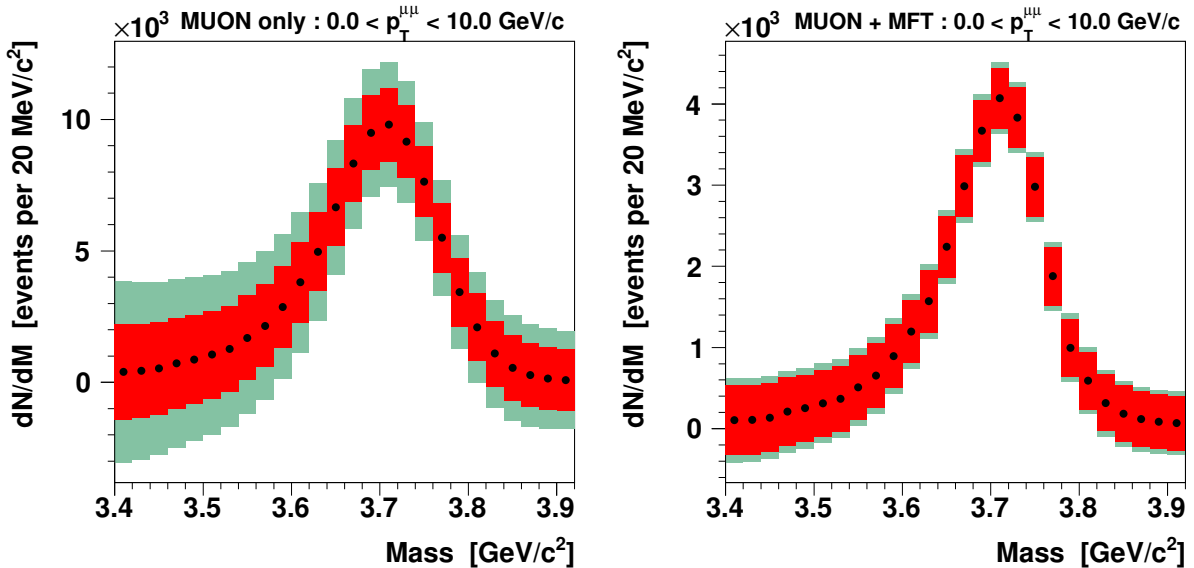


Figure 2.13: Expected uncertainties on the ψ' signal extraction in the two scenarios without (left panel) and with (right panel) the MFT, for $0-10\%$ Pb-Pb collisions at $\sqrt{s_{NN}} = 5.5$ TeV and a 10 nb^{-1} integrated luminosity scenario. The smaller red boxes account for statistical uncertainties alone; the larger green boxes represent the linear sum of statistical and systematic uncertainties.

The statistical errors are obtained combining the statistical uncertainties of the signal itself and of the subtracted background. Since these errors are *not correlated* between the bins, the statistical uncertainty on the integrated signal is estimated by fitting the mass distribution with a fixed-shape function having the normalisation as the only free parameter.

The systematic uncertainty mainly comes from the combination of three components, the first one due to the choice of the function used to describe the isolated signal, the second one given by the global systematic uncertainty on the shape and the normalisation of the background, and finally the third one given by the uncertainty on the cuts and selections. The analysis proved the last two components to be dominating over the first one, which in the following will be safely neglected. The estimation of the systematic uncertainty on the shape and the normalisation of the background was estimated to be $\sim 0.1\%$ per bin from the experience of the J/ψ analysis on the Pb-Pb data at $\sqrt{s_{NN}} = 2.76$ TeV [72]. This value is assumed to stay valid in both the scenarios with and without MFT. Since this uncertainty propagates to the signal via the S/B ratio, the only way to limit it is to increase the S/B. The background reduction made possible by the MFT, indeed, goes exactly in this direction. Contrary to the case of the statistical uncertainty, the systematical uncertainties Figure 2.13 must be regarded to be bin-per-bin *correlated*; in this case, so, the total systematic uncertainty on the extracted signal is evaluated by adding the systematic uncertainties on each bin, within the mass window of the signal.

The remaining source of systematic uncertainty is the one coming from the cuts and selections used to extract the charmonium signals. In the MUON only scenario the error on the selections has been estimated to 5 % in the light of the experience of the J/ψ analysis on the Pb-Pb data at $\sqrt{s_{NN}} = 2.76$ TeV. Concerning the MFT scenario, an additional uncertainty comes from the MFT based selection criteria, which was estimated to be 4–5 % by varying the MFT based selection cuts by $\pm 10\%$.

Table 2.2: Expected yields, S/B, significance, and statistical and systematical uncertainties for inclusive J/ψ production in the scenarios without (top) and with (bottom) the MFT.

Inclusive J/ψ ($2.80 < M_{\mu\mu} < 3.30 \text{ GeV}/c^2$) : $R_{AA} = 0.7$, without the MFT					
p_T [GeV/c]	Signal [$\times 10^3$]	S/B	$S/\sqrt{S+B}$	Stat. Err. [%]	Sys. Err. [%]
0 – 1	1710	0.15	470	0.20	5
1 – 2	3320	0.14	650	0.14	5
2 – 3	2784	0.16	610	0.16	5
3 – 4	1750	0.16	490	0.19	5
4 – 5	1055	0.18	400	0.25	5
0 – 10	12040	0.15	1 300	0.08	5

Inclusive J/ψ ($2.80 < M_{\mu\mu} < 3.30 \text{ GeV}/c^2$) : $R_{AA} = 0.7$, with the MFT					
p_T [GeV/c]	Signal [$\times 10^3$]	S/B	$S/\sqrt{S+B}$	Stat. Err. [%]	Sys. Err. [%]
0 – 1	531.6	0.50	420	0.23	7
1 – 2	851.9	0.92	640	0.15	7
2 – 3	715.3	1.28	630	0.15	7
3 – 4	544.0	2.03	600	0.17	7
4 – 5	382.2	3.25	540	0.18	7
0 – 10	3664	1.15	1 400	0.07	7

In order to clearly establish, if and by which amount the presence of the MFT actually improves the performance of the signal extraction for the inclusive charmonium production, the values of the expected yield, S/B and significance for the J/ψ and the ψ' are compiled in Tables 2.2 and 2.3, respectively. The numbers allow us to confirm, on a quantitative ground, what was already noted by direct inspection of the global plots in Figure 2.12: the MFT leads to an improvement of the S/B for both the J/ψ and the ψ' by a factor 3 to 10 depending on the p_T . Moreover, although the improvement of the S/B is obtained on the expense of a sensible statistics loss, not only the significance of the signals does not decrease when introducing the MFT, but it even increases by factors up to 2 in the case of the ψ' .

For the J/ψ analysis, the MFT will not improve the measurement, as the main source of systematics in this case is not the background subtraction uncertainty but the one coming from the selection cuts. Therefore, the slight increase of systematics due to the new MFT based selections is not compensated by the reduction of the background subtraction systematic coming from the increase of S/B ratio. We can note anyway, how in the case of the inclusive J/ψ signal the MFT allows an independent analysis having different sources of systematics than the standard ones based on the MUON only scenario, thus offering a useful cross check to the study.

For the ψ' the conclusions are the opposite, as in this case the uncertainty from the background subtraction is the dominant one in the scenario without MFT. By introducing the MFT, the systematic uncertainties coming from background subtraction are largely reduced. The total systematic

Table 2.3: Expected yields, S/B , significance, and statistical and systematical uncertainties for inclusive ψ' production in the scenario without (top) and with (bottom) the MFT.

Inclusive ψ' ($3.40 < M_{\mu\mu} < 3.90 \text{ GeV}/c^2$) : $R_{AA} = 0.3$, without the MFT					
p_T [GeV/c]	Signal [$\times 10^3$]	S/B	$S/\sqrt{S+B}$	Stat. Err. [%]	Sys. Err. [%]
0 – 1	12.8	0.0048	7.6	10.9	20.9
1 – 2	24.2	0.0039	9.7	9.5	26.5
2 – 3	20.4	0.0031	8.0	12.3	32.3
3 – 4	12.4	0.0026	5.6	17.7	39.0
4 – 5	6.9	0.0021	3.8	26.1	48.1
0 – 10	85.0	0.0030	16.1	6.0	33.3

Inclusive ψ' ($3.40 < M_{\mu\mu} < 3.90 \text{ GeV}/c^2$) : $R_{AA} = 0.3$, with the MFT					
p_T [GeV/c]	Signal [$\times 10^3$]	S/B	$S/\sqrt{S+B}$	Stat. Err. [%]	Sys. Err. [%]
0 – 1	4.47	0.014	7.8	10.7	9.9
1 – 2	8.67	0.014	11	8.5	10.1
2 – 3	6.76	0.018	11	8.7	9.0
3 – 4	4.11	0.027	10	9.0	8.0
4 – 5	2.57	0.030	8.7	10.9	7.8
0 – 10	30.3	0.017	22	4.3	9.2

uncertainties become of the order of the statistical ones, which gives us a much better precision in the measurement of the R_{AA} of the ψ' at the expected integrated luminosity of 10 nb^{-1} .

The information contained in Table 2.3 can be conveniently illustrated in the form of a plot, showing the expected uncertainties on the evaluation of the R_{AA} . These plots are shown for the ψ' as a function of p_T in Figure 2.14, where the scenarios without and with the MFT can be directly compared. As one can notice, the plots clearly show how the level of the systematic uncertainties represents a strong limit to the measurement of ψ' without the MFT.

2.4.4.2 J/ψ from Beauty Hadrons

The identification of J/ψ coming from b -hadron decays can be performed by means of the measurement of the secondary $\mu^+ \mu^-$ vertex, displaced with respect to the primary collision vertex (see Figure 2.15). The displacement vector \vec{r} , between the $\mu^+ \mu^-$ vertex and the primary vertex, is measured in the plane transverse to the beam direction. The most probable transverse decay length of the b -hadron, in the laboratory frame [73, 74], is calculated as

$$L_{xy} = \frac{\hat{u}^T S^{-1} \vec{r}}{\hat{u}^T S^{-1} \hat{u}} \approx \frac{\hat{u}^T \cdot \vec{r}}{\hat{u}^T \cdot \hat{u}}, \quad (2.3)$$

where \hat{u} is the unit vector in the direction of the J/ψ and S^{-1} is the inverse of the sum of the primary and secondary vertex covariance matrices. It should be noted that, throughout this document, the

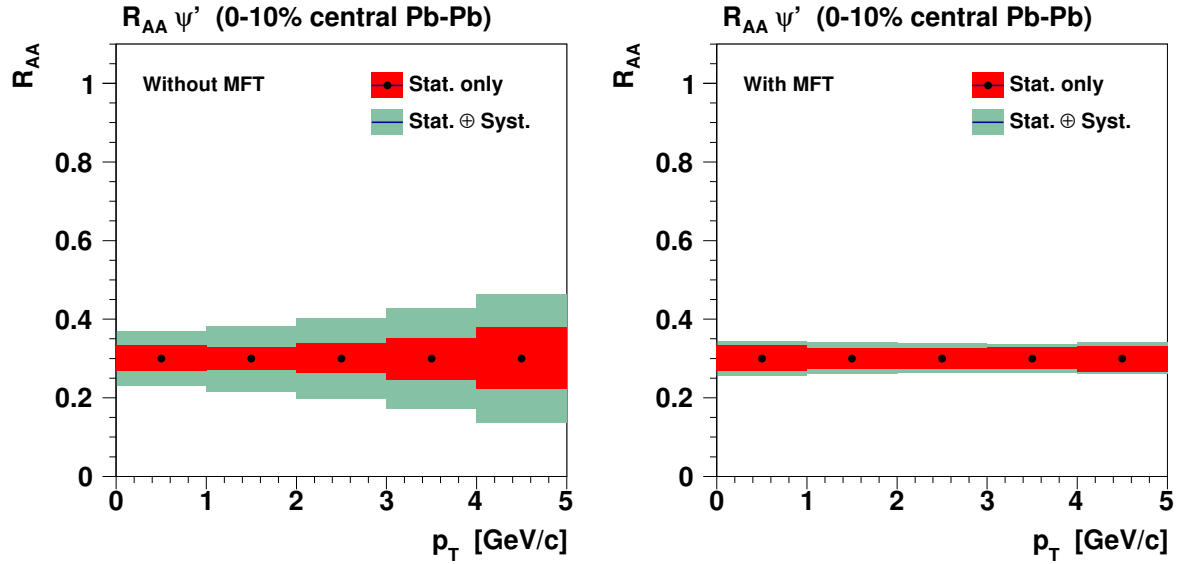


Figure 2.14: Expected uncertainties on the measurement of the p_T -integrated nuclear modification factors R_{AA} of the ψ' in the two scenarios without (left panels) and with (right panels) the MFT, for 0-10 % Pb-Pb collisions at $\sqrt{s_{NN}} = 5.5$ TeV and a 10 nb^{-1} integrated luminosity scenario. A value of $R_{AA}(\psi') = 0.3$ is considered here. The smaller red boxes account for statistical uncertainties alone; the larger green boxes represent the sum in quadrature of statistical and systematic uncertainties.

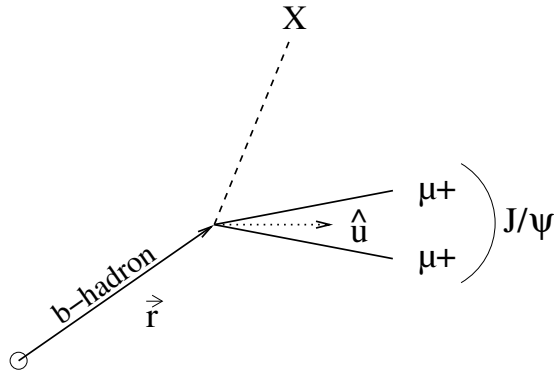


Figure 2.15: Schematic representation of a b -hadron decay into J/ψ .

approximated definition will be used, in which the covariance matrices of the vertices are assumed to be diagonal. From L_{xy} , the pseudo-proper decay length $l_{J/\psi}$ is computed as an estimate of the b -hadron decay length:

$$l_{J/\psi} = L_{xy} \frac{m_{J/\psi}}{p_T^{J/\psi}}. \quad (2.4)$$

Figure 2.16 shows the pseudo-proper decay length distributions of prompt and non-prompt J/ψ . Non-prompt J/ψ have been generated using the Perugia0 tune of PYTHIA, forcing b -hadrons to decay into J/ψ . A fit function is superimposed onto the distributions, defined as a Gaussian, whose σ varies as a function of the mass with a polynomial function of 3rd degree. The background contribution is not shown; its normalisation can be safely fixed by performing a fit on the dimuon mass spectrum in the J/ψ mass window.

The finite width of the observed distribution for prompt J/ψ comes from two contributions: (i) the spatial resolution of the MFT in reconstructing the secondary vertex (i.e. the PCA of the two

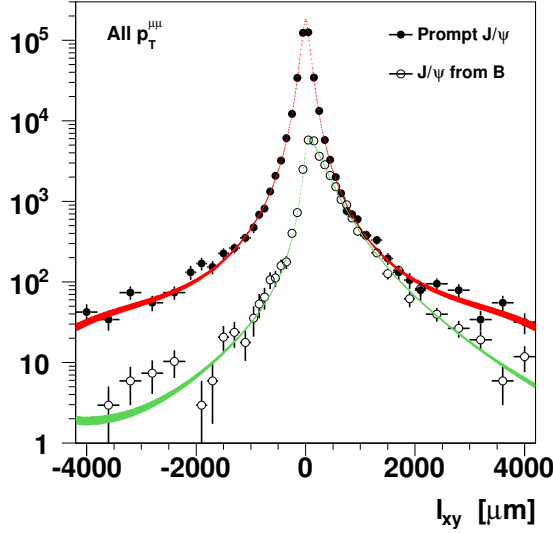


Figure 2.16: Pseudo-proper decay length distributions of prompt J/ψ and J/ψ from b -hadrons, together with their parameterisations, for 0-10% Pb-Pb collisions at $\sqrt{s_{\text{NN}}} = 5.5$ TeV. The normalisations account for a 10 nb^{-1} integrated luminosity scenario and the expected displaced/prompt ratio, see Section 2.4.4.2.

muons) and (ii) the spatial resolution of the primary vertex, assumed to be $50 \mu\text{m}$ in the three spatial directions (x , y and z).

Global pseudo-proper decay-length plots can be obtained by adding up the l_{xy} distributions of the prompt and displaced J/ψ signals and the background. The distributions obtained for dimuons inside the J/ψ mass window are parameterised as explained above; we will refer to these parameterisations as the “MC templates” of the l_{xy} distributions of the signal and background components. To establish the normalisation of the background and J/ψ components as a function of p_T , we consider the expected values for the yield of the inclusive (prompt + displaced) J/ψ signal and the S/B, reported in Table 2.2. The ratio between the displaced and prompt J/ψ components in the rapidity range of the Muon Spectrometer is taken from the LHCb measurement of J/ψ in pp collisions at $\sqrt{s} = 7$ TeV [75]. In order to reduce the contribution from the background, the mass window considered when building the pseudo-proper decay length distributions can be properly shrunk. Table 2.4 compiles the expected statistics for the background and for prompt and displaced J/ψ for three choices of the mass windows, accounting respectively for $\sim 99\%$, $\sim 95\%$ and $\sim 66\%$ of the J/ψ peak integral. Due to its more favourable S/B ratio, the last choice of the mass range is considered in what follows. Even with the loss of statistics this still allows a reliable signal extraction in a scenario with a 10 nb^{-1} integrated luminosity, as will be discussed below.

The global pseudo-proper decay-length distribution is generated for each bin of p_T from the MC templates of the three components, including fluctuations according to the expected statistics. These global distributions are then fitted with the superposition of these same MC templates, whose normalisations are in this case treated as free parameters without any specific initial assumption on their values, with the exception of the background: this latter is fixed to its “true” normalisation based on the hypothesis that it can be extracted from an independent fit of the mass spectrum. The systematic uncertainty of the evaluation of the background normalisation, expected to be $\sim 1\%$ when integrated over the J/ψ mass window, is propagated here. The information we aim to extract from the fit on the pseudo-proper decay-length distribution is conveniently expressed by the ratio between the displaced and prompt J/ψ production.

Since the MC templates are used at the same time to build the global pseudo-proper decay-length distribution and to decompose it into its components, the parameters found in this first fit (see Figure 2.17) reflect the statistical uncertainties only, related to the available population of the con-

Prompt and displaced J/ψ ($2.80 < M_{\mu\mu} < 3.30 \text{ GeV}/c^2$) : $R_{AA} = 0.7$			
p_T [GeV/c]	Prompt J/ψ	Displaced J/ψ	Background
0 – 1	489 000	39 000	1 064 000
1 – 2	775 000	70 000	926 000
2 – 3	644 000	64 000	559 000
3 – 4	484 000	53 000	268 000
4 – 5	336 000	40 000	118 000

Prompt and displaced J/ψ ($2.85 < M_{\mu\mu} < 3.25 \text{ GeV}/c^2$) : $R_{AA} = 0.7$			
p_T [GeV/c]	Prompt J/ψ	Displaced J/ψ	Background
0 – 1	472 000	37 000	892 000
1 – 2	744 000	67 000	779 000
2 – 3	618 000	62 000	469 000
3 – 4	465 000	51 000	224 000
4 – 5	323 000	38 000	98 000

Prompt and displaced J/ψ ($3.00 < M_{\mu\mu} < 3.20 \text{ GeV}/c^2$) : $R_{AA} = 0.7$			
p_T [GeV/c]	Prompt J/ψ	Displaced J/ψ	Background
0 – 1	417 000	33 000	375 000
1 – 2	677 000	61 000	357 000
2 – 3	563 000	56 000	215 000
3 – 4	430 000	47 000	101 000
4 – 5	298 000	36 000	45 000

Table 2.4: Expected statistics for prompt and displaced J/ψ production, and background in the J/ψ mass window.

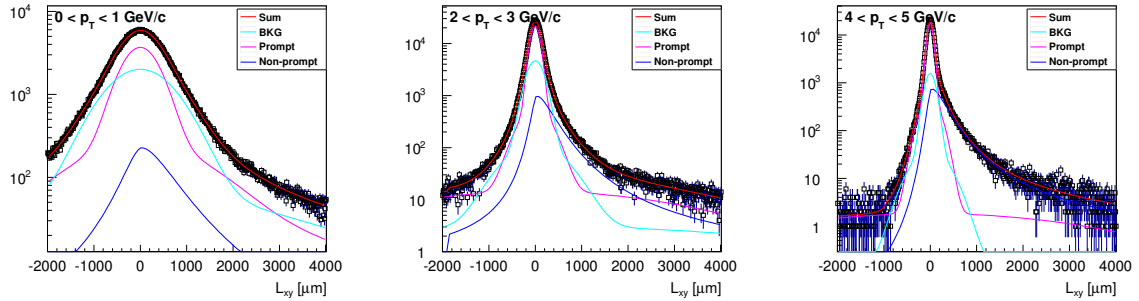


Figure 2.17: Fit of the global pseudo-proper decay-length distributions, for 0-10 % Pb-Pb collisions at $\sqrt{s_{\text{NN}}} = 5.5 \text{ TeV}$, with the superposition of the three expected contributions for three different p_{T} bins.

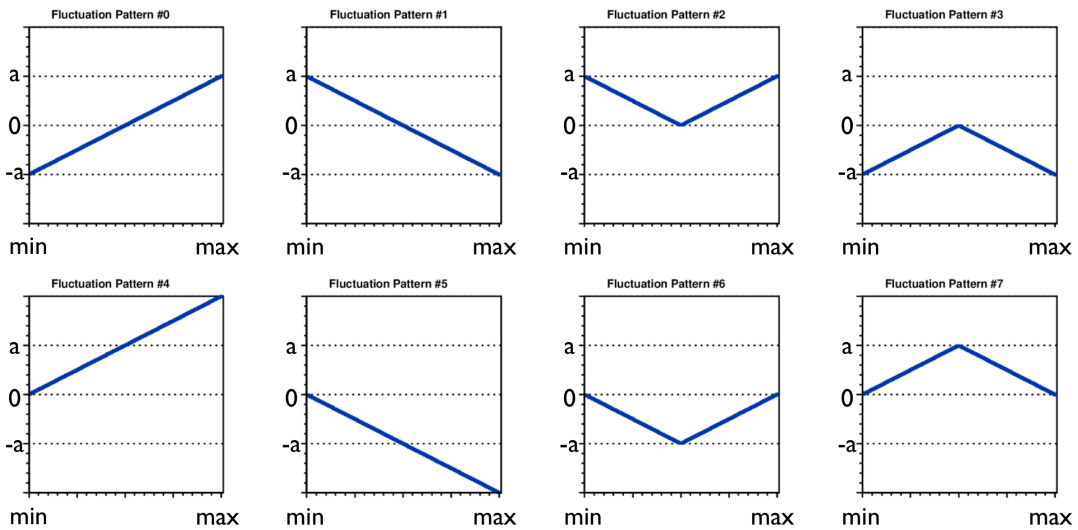


Figure 2.18: Eight distortion patterns considered to simulate the ignorance of the shape of the pseudo-proper decay-length distribution. “ a ” is the amplitude of the distortion applied.

sidered sample. This situation corresponds to having a perfect MC knowledge of the pseudo-proper decay-length distributions of each process. In the real life, however, one should expect that the MC simulations are able to reproduce the true distributions with a limited precision: this will result in a systematic uncertainty on the normalisation of the signal extracted from the fit.

A possible way to estimate this source of systematic uncertainty on the signal extraction works as follows. To the MC templates of the three components considered in the fit – the background, the prompt and displaced J/ψ signals – a distortion is applied according to some chosen pattern; a new fit of the global pseudo-proper decay length distribution is then performed, using these deformed MC templates. Defining various distortion patterns, and applying them to the three fit components considering every possible combinations, we can build for each parameter a distribution of values whose RMS can be taken as the estimator of the systematic uncertainty on the parameter due to the uncertainty on the MC pseudo-proper decay-length templates.

Table 2.5: *Expected statistical and systematic uncertainties on the evaluation of the displaced/prompt J/ψ production.*

p_T [GeV/c]	Stat. Err. [%]	Systematic Error [%]				
		$a = 1\%$	$a = 2\%$	$a = 3\%$	$a = 4\%$	$a = 5\%$
0 – 1	6.6	20.2	42.0	62.7	89.6	104
1 – 2	1.4	5.3	10.0	15.1	19.9	23.9
2 – 3	0.9	3.2	6.5	9.7	12.9	16.2
3 – 4	0.8	2.8	5.3	7.8	10.2	12.7
4 – 5	0.8	2.4	4.8	7.1	9.6	12.0

Figure 2.18 shows the distortion patterns considered in this study. As one can see, they are a mixture of simple even and odd functions, all characterised by the same parameter a representing the amplitude of the fluctuation applied. In absence of a reliable estimate of the typical amplitude a , which can be expected in a real analysis, several choices have been considered here, ranging from $a = 1\%$ to $a = 5\%$. The corresponding systematic uncertainties on the displaced/prompt J/ψ ratio estimate are shown in Figure 2.19 together with the statistical uncertainties reflecting the available statistics. The results are also compiled in Table 2.5. Not surprisingly, the systematic uncertainty on the extraction of the displaced/prompt J/ψ ratio especially affects the signal extraction below $p_T = 1$ GeV/c, which cannot be reasonably performed if the typical scale of the uncertainty on the MC templates exceeds $\sim 2\%$.

A second, independent evaluation of the systematic uncertainties coming from the MC templates has also been considered: in this case, the “MC data” obtained with the nominal MFT secondary-vertex (thus, pseudo-proper decay-length) resolution are fitted with MC templates obtained varying this resolution by 10 % up and down. The impact of this kind of uncertainty, however, can be naturally limited by treating the resolution of the pseudo-proper decay length distributions as a free parameter to be optimised by the fit, which is thus able to partially recover the error on the assumed hypothesis². The uncertainties found in this way stay below the ones compiled in the last column of Table 2.5, which are then retained as conservative estimates.

Future Improvements for the Displaced J/ψ Analysis

² In this case, the pseudo-proper decay length distribution considered in the fit is a convolution of the distribution relative to the ideal MFT resolution with a Gaussian, whose width is optimised.

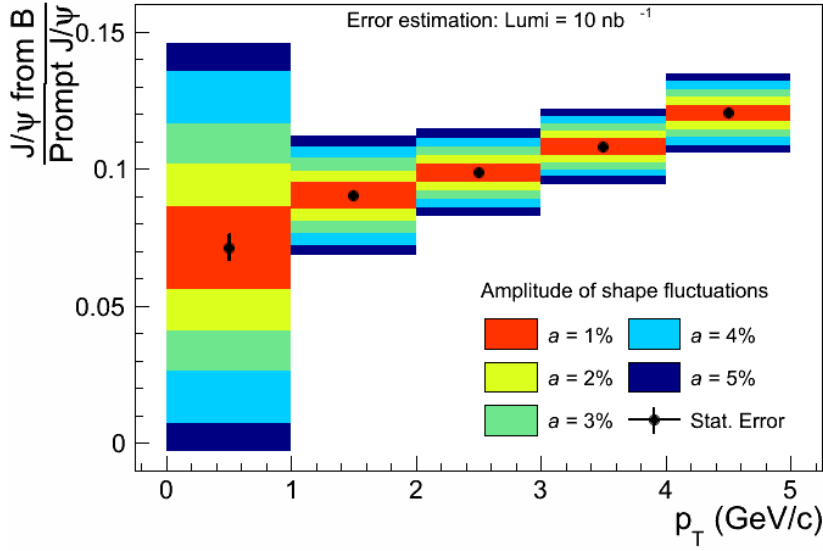


Figure 2.19: Statistical and systematical uncertainties expected in the measurement of the displaced/prompt J/ψ ratio for 0-10% Pb-Pb collisions at $\sqrt{s_{\text{NN}}} = 5.5$ TeV, in a 10 nb^{-1} integrated luminosity scenario.

In the above discussion, an analysis strategy based on the pseudo-proper decay length l_{xy} (see Equation 2.4) was presented: as it was shown, this variable is able to discriminate prompt and displaced J/ψ down to $p_T \sim 1$ GeV/c with uncertainties below $\sim 20\%$. The l_{xy} decay length, however, is found to be better suited to an experimental setup in which J/ψ dimuons are measured at mid-rapidity. When moving to forward rapidities, in fact, the measurement of the *longitudinal* separation between the primary and secondary vertices becomes the best way to discriminate prompt and displaced J/ψ : due to the geometry acceptance of the detector, in fact, the momentum of the decaying B hadron is essentially longitudinal and the decay length can be found as large as few mm (thanks to the Lorentz boost) even at low p_T .

An approach based on the measurement of the longitudinal decay length of the B mesons, was adopted by the LHCb Collaboration in performing the analysis of displaced J/ψ production in pp collisions [75]. In that case, the so called pseudo-proper decay time was considered, defined as:

$$t_z = \frac{(z_{J/\psi} - z_0) \cdot m_{J/\psi}}{p_z}, \quad (2.5)$$

where $z_{J/\psi}$ and z_0 are the longitudinal positions of the secondary and primary vertices, respectively. As recent, preliminary investigations have shown, the t_z variable (or the corresponding pseudo-proper decay length ct_z) has better performances in displaced/prompt J/ψ disentanglement also in the case of a MUON+MFT setup of the ALICE Muon Arm, with respect to the l_{xy} variable considered in the present document. In particular, reliable displaced/prompt separation should be accessible even for $0 < p_T < 1$ GeV/c by means of the analysis of the t_z . A dedicated effort is currently in place in order to obtain a precise evaluation of the performances and the expected uncertainties in the whole range $0 < p_T < 5$ GeV/c.

2.4.5 Contribution of the MFT to the ALICE Charmonia Program

Studying beauty via the golden channel $B \rightarrow J/\psi + X$ give us the possibility to go to almost zero p_T of the B meson, if one can reach p_T of the J/ψ of the order of $1 - 2$ GeV/c. An interesting

observable is the nuclear modification factor of the non-prompt J/ψ , which turns out to be an indirect measurement of beauty R_{AA} . The nuclear modification factor of non-prompt J/ψ , $R_{AA}^{J/\psi \leftarrow B}$, can be extracted using the measurements of prompt J/ψ R_{AA} and the fractions of non-prompt J/ψ in proton–proton and Pb–Pb collisions,

$$R_{AA}^{J/\psi \leftarrow B} = R_{AA}^{J/\psi \text{ prompt}} \times \frac{f_{\text{Pb-Pb}}^{J/\psi \leftarrow B}}{f_{\text{pp}}^{J/\psi \leftarrow B}}. \quad (2.6)$$

The expected performance of the MFT/MUON for the measurement of $R_{AA}^{J/\psi \leftarrow B}$ can be compared with the expected performance of the new ITS in the channel $B \rightarrow D^0$ (Figure 2.20). The MFT/MUON measurement is complementing the CMS measurement increasing the rapidity and p_T coverages to higher rapidity and lower p_T . Work in the CMS collaboration is ongoing to lower the minimum p_T , but the CMS performance won't be able to match the one of the MFT/MUON due to larger systematics coming from the small acceptance of the detector for $p_T < 3 \text{ GeV}/c$.

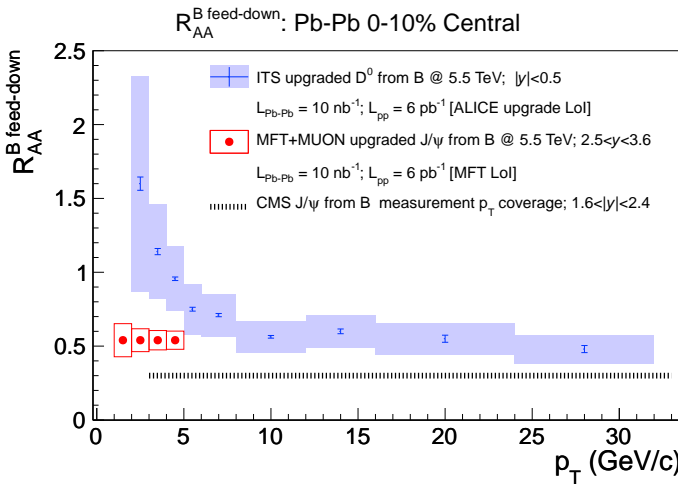


Figure 2.20: Beauty nuclear modification factor versus p_T . Comparison between the expected performance with the new ITS via the non-prompt D^0 measurement [1] (blue band) and the expected performance of the MFT/MUON via the non-prompt J/ψ identification (red points). The CMS p_T coverage via non-prompt J/ψ identification is also represented (dotted line).

We have shown that the MFT allows a more precise measurement of the ψ' production yields. The measurement of the ψ' , combined with the J/ψ measurement, offers an important tool to discriminate between different charmonium production models. Two main models are proposed. The first one is based on the idea of statistical hadronisation of charm quarks in nucleus–nucleus collisions [76–80]. In this model, all charmonium states are assumed to be fully melted in the QGP and produced, together with all other hadrons, exclusively at chemical freeze-out. The second model is based on the idea of kinetic recombination of charm and anti-charm quarks in the QGP as a quarkonium production mechanism [42, 43, 81]. In this model, a continuous dissociation and regeneration of charmonium takes place in the QGP over its entire lifetime.

Figure 2.21-left shows the experimental status for the measurement of the ratio $R_{AA}^{\psi'}/R_{AA}^{J/\psi}$. The ALICE Muon Spectrometer measurements do not allow the evaluation of this ratio for the most central Pb–Pb collisions, where the ψ' extraction is very difficult or even impossible due to the very small S/B ratio. The CMS measurements still suffer from large systematic uncertainties, mainly due to the error in the proton–proton reference at $\sqrt{s_{\text{NN}}} = 2.76 \text{ TeV}$, making any interpretation of the results difficult. We superimposed the expected uncertainties for a measurement using the Muon Spectrometer with the MFT at forward rapidity. The expected performance is also compared with

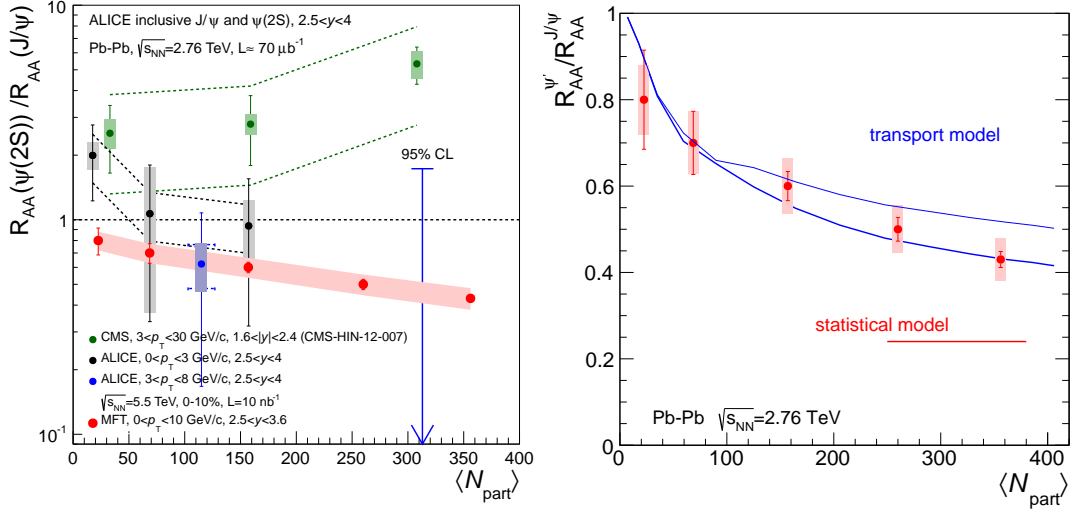


Figure 2.21: Ratio of the nuclear modification factor of ψ' and J/ψ versus the number of participants. Left: comparison of the expected uncertainties of MFT/MUON (red points) with the measurements of CMS (green points) and ALICE (blue and black points) at $\sqrt{s_{NN}} = 2.76$ TeV. The error bars represent the statistical uncertainties, the coloured area the systematical ones while the dashed lines shows the uncertainties coming from the pp reference. Right: comparison of the expected MFT/MUON performance with two charmonium production models (statistical and transport models) [42, 43, 76, 77].

the two charmonium production models cited above (Figure 2.21-right), showing the discrimination power offered by the addition of the MFT.

2.5 Open Heavy Flavour in Central Pb–Pb collisions

Due to their long lifetime, beauty and charm hadrons decays ($c\tau \sim 500 \mu\text{m}$ and $\sim 150 \mu\text{m}$, respectively) have a secondary vertex displaced in space from the primary collision vertex. The offset distribution will be helpful to discriminate muons coming from charm and beauty decays down to low transverse momentum.

In the analysis presented hereafter we will show the expected performance of the MFT setup for the measurement of single muons and dimuons from charm and beauty decays in central Pb–Pb collisions.

2.5.1 Signal and Background Simulations

Full AliRoot simulations were performed from generation to reconstruction. Open heavy-flavour hadrons are either directly produced through a fast generator of correlated heavy-flavour hadron pairs based on a parameterisation of PYTHIA or obtained through HIJING Monte Carlo simulations, assuming in both cases a pile-up scenario of two central Pb–Pb events. The fast generator allows to save CPU time and to accumulate large statistics in the high p_T region, while HIJING simulations are used to study the variety of available sources of single muons, to optimise track selection cuts and to perform background subtraction. The fast generator uses parameterised kinematics of quark pairs from the event generator PYTHIA (6.214) using CTEQ4L PDF for Pb–Pb.

Only primary particles (namely B or D hadrons generated according to the pair parameterisation) and short-lived particles ($c\tau < 0.3 \mu\text{m}$) are decayed with Alipythia. Decays of all other particles are handled by GEANT. A total number of about $2 \cdot 10^5$ events both for open charm and beauty have been produced using the fast generator and reconstructed. The number of reconstructed muons from open charm (beauty) decays in the acceptance of the spectrometer is about 10^6 (10^5). In order

to assume the worst pile-up scenario for the occupancy of the MFT planes, all generated events are merged with clusters from two central Pb–Pb events (one Pb–Pb collision at the nominal primary vertex and a second one with a vertex chosen randomly according to the beam diamond size).

About $9 \cdot 10^5$ HIJING events were also produced for the 10% most central Pb–Pb collisions at $\sqrt{s_{\text{NN}}} = 5.5$ TeV, assuming no quenching effect. Table 2.6 summarises the statistics of the different muon sources in the acceptance of the muon spectrometer as produced in the HIJING simulations.

Table 2.6: Statistics for single muon candidates from open heavy-flavour decays and other sources produced through HIJING simulations (see the text for details).

<i>b</i> -direct	<i>b</i> -chain	<i>c</i> -direct	<i>c</i> -chain	decay μ	not μ	fakes
32 412	26 929	233 005	23 326	$4.21 \cdot 10^6$	$1.10 \cdot 10^6$	$2.00 \cdot 10^6$

At the LHC, single muons are mainly produced through D-hadron, B-hadron and light hadron (mainly π , K) decays. In Table 2.6, the *b*-direct or *c*-direct channels are related to muons produced directly from B-hadron or D-hadron disintegrations, respectively. The *c*-chain (*b*-chain) takes into account muons produced after a multiple decays chain by example $B \rightarrow D \rightarrow \mu$ ($D \rightarrow \pi \rightarrow \mu$). Background muons represent a large fraction of reconstructed tracks (see Table 2.6), and can be roughly divided in three components: (i) a first component is composed of muons coming from pion or kaon decays and from resonance decays; (ii) a second one corresponds to punch-through hadrons which escape from the hadronic absorber and manage to leave a signal in the tracking chambers; (iii) the component called “fakes”, finally, contains tracks which are not associated to one single particle crossing the whole spectrometer: these tracks are the result of the association of clusters of different particles combined together by the tracking algorithm.

2.5.2 Track Selection

In this section we will describe the selection cuts defined to reject background muons, preserving as much as possible the signal components.

Figure 2.22-left presents the typical p_T distribution of reconstructed single muons from the available sample of $9 \cdot 10^5$ HIJING events, with the only request that the muons are reconstructed in the acceptance of the muon spectrometer without any cut. From these distributions one can see that fake MUON tracks are dominant over all p_T and it is difficult to separate them from real muon tracks. As expected, it is sufficient to require that the MUON tracks match with an “all- p_T ” tracklet ($p_T \gtrsim 0.5$ GeV/c) in the muon trigger stations to reject almost the totality of fake MUON tracks, as well as the hadrons reconstructed as MUON tracks: here one can appreciate the role of the iron wall filter interposed between the tracking and the trigger systems, ensuring a clean muon identification without degrading the kinematics of the retained tracks (the information of the trigger tracklet is not exploited in the evaluation of the track’s kinematics). It should be also remarked that the matching condition between MUON tracks and trigger tracklet will continue to be the standard way to identify muon tracks in ALICE even in presence of the MFT.

Another variable, which turns out to be useful in selecting the final sample of muons for the analysis, is the “Distance of Closest Approach” (DCA) between the extrapolated MUON track (from the Muon Spectrometer only) and the interaction vertex in the plane perpendicular to the beam direction and containing the vertex. This variable, largely used in the muon analyses with the current Muon Spectrometer setup, allows to reject almost all remaining fake MUON tracks and hadrons, which have survived after the matching between MUON tracks and trigger tracklets. The cut is applied on $p \times \text{DCA}$ in order to cancel the effect of the momentum dependence of the DCA length. In addition,

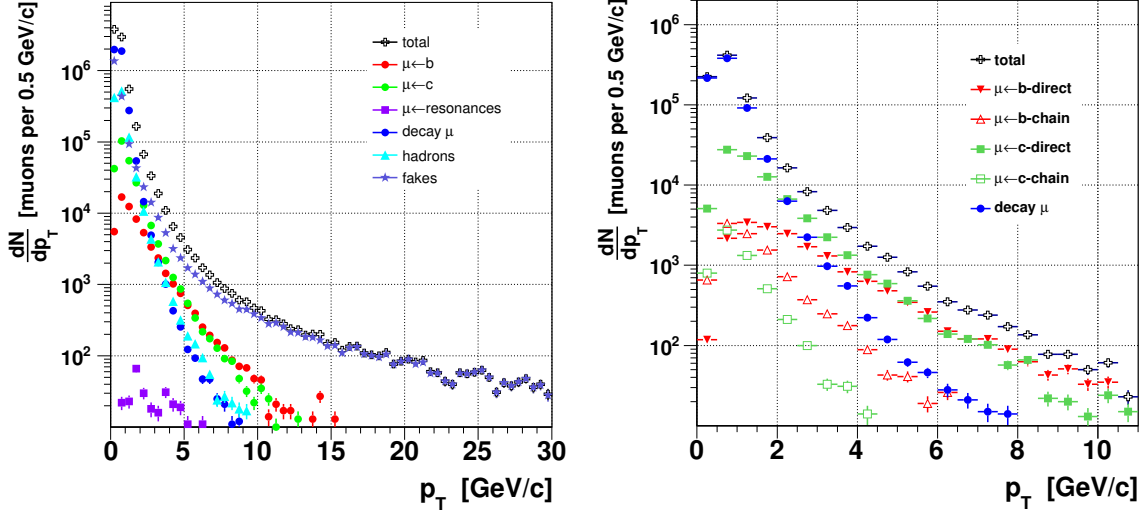


Figure 2.22: p_T distributions of reconstructed muons without any cut (left) and with all selection criteria applied (right) in the acceptance of the muon spectrometer. The different sources are displayed.

this cut turns out to be effective in removing fake matches between MUON tracks and MFT cluster: fake matches have large $p \times \text{DCA}$ values in the low p_T range compared to well-matched tracks.

Finally, a quality cut on the global track χ^2 is applied on top of the previous ones, such that only global tracks with $\chi^2 < 1.3$ are retained for the analysis.

Figure 2.22-right presents single muon p_T distributions with all cuts applied. For $p_T \gtrsim 3 \text{ GeV}/c$, the reconstructed muon distribution consists mainly of muons from open charm and beauty decays. Components of muons from resonances, fake tracks and tracks from punch-through hadrons, negligible after the cuts, are excluded from the plot. In the region $2 < p_T < 3 \text{ GeV}/c$ the charm component is the dominating one, while for $p_T < 2 \text{ GeV}/c$ the background is the largest source of muons. To summarise, the following cuts are applied in the open heavy-flavour analysis:

- All- p_T matching between MUON track and trigger tracklet ($p_T \gtrsim 0.5 \text{ GeV}/c$);
- $-3.6 < \eta < -2.5$;
- $p \times \text{DCA} < 120 \text{ cm} \cdot \text{GeV}/c$;
- $\chi^2 < 1.3$.

2.5.3 Expected Yields and Signal Extraction for Single Muons

2.5.3.1 Statistics Estimate

The normalisation of the open heavy-flavour sources is performed on the basis of the expected p_T spectra from fixed order next-to-leading-log (FONLL) calculations [82]. This allows to normalise the offset distributions of muons from open heavy-flavour decays in different p_T bins, simply extracting the normalisations from the FONLL predictions reported in Figure 2.23:

$$\frac{dN_{PbPb}^{\mu \leftarrow HF}}{dp_T} = N_{EV} \times \epsilon \times \frac{d\sigma_{pp}^{\mu \leftarrow HF}}{dp_T} (\text{FONLL}) \times \frac{N_{coll}}{\sigma_{NN}}, \quad (2.7)$$

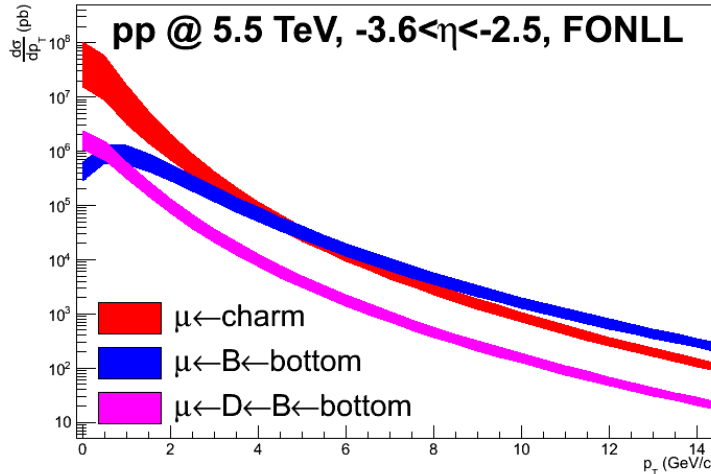


Figure 2.23: p_T distributions of muons from open charm and beauty decays from FONLL calculations.

where we assume $\sigma_{NN} = 60$ mb and $N_{coll} = 1600$ in Pb–Pb at $\sqrt{s_{NN}} = 5.5$ TeV. The factor ϵ takes the acceptance and reconstruction efficiency into account.

After applying all selection cuts, the p_T distribution of background muons is assumed to be composed of muons coming from light-hadrons decays and resonances only. The statistics available through the HIJING simulation allows to exploit the muon spectra up to about 10 GeV/c. In order to avoid fluctuations in the high- p_T region, the p_T distribution of background muons are fitted to $p_T \sim 10$ GeV/c. The background p_T spectrum is directly normalised to the expected number of events, according to the HIJING multiplicity, and added to the spectra of muons from open heavy-flavour decays normalised with the FONLL predictions. Signal and background p_T distributions, normalised to an integrated luminosity of 10 nb^{-1} and corrected for efficiency, are presented in Figure 2.24.

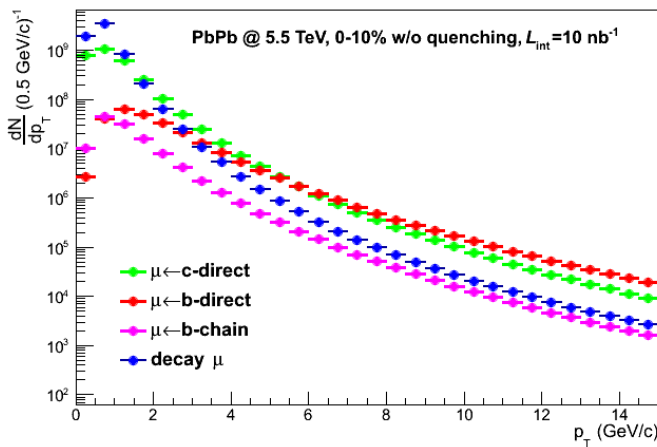


Figure 2.24: p_T distributions of reconstructed single muons from open heavy-flavour decays and background, assuming an integrated luminosity of 10 nb^{-1} in Pb–Pb central collision. All cuts described in the previous section are applied.

2.5.3.2 Analysis Strategy and Expected Performance

Once the normalisations of the signal and background components are known as a function of p_T , see Figure 2.24, global offset distributions can be built by adding up the distributions expected for the signal and the background. In doing so, we assume that our signal is composed of muons from charm and beauty decay, while all other sources (basically light mesons) are merged in the background. To summarise, we assume the following definitions of signal and background:

- Signal:

- direct open charm decay;
 - direct open beauty decay;
 - beauty decay chain.
- Background:
- muons from light mesons;
 - any other source of muons not belonging to the previous cases.

The corresponding expected statistics extracted from the distributions in Figure 2.24 are reported in Table 2.7 for an integrated luminosity scenario of 10 nb^{-1} .

Table 2.7: *Expected yields for muons from open heavy-flavour decays*

p_T [GeV/c]	Charm [$\times 10^6$]	Beauty [$\times 10^6$]
0 – 1	1860	98
1 – 2	882	159
2 – 3	154	65.4
3 – 4	37.2	25.0
4 – 5	11.6	10.4
5 – 7	6.2	7.1
0 – 10	2953	367

The resulting offset distributions obtained from the MC are then parameterised for each p_T bin up to 7 GeV/c with a variable width Gaussian, whose σ is a polynomial function of the offset. These functions define the so-called “MC templates”, which can be sampled – for each signal and background source – to build offset distributions filled with expected statistics. In this way, the originally large fluctuations due to the limited MC sample can be eliminated.

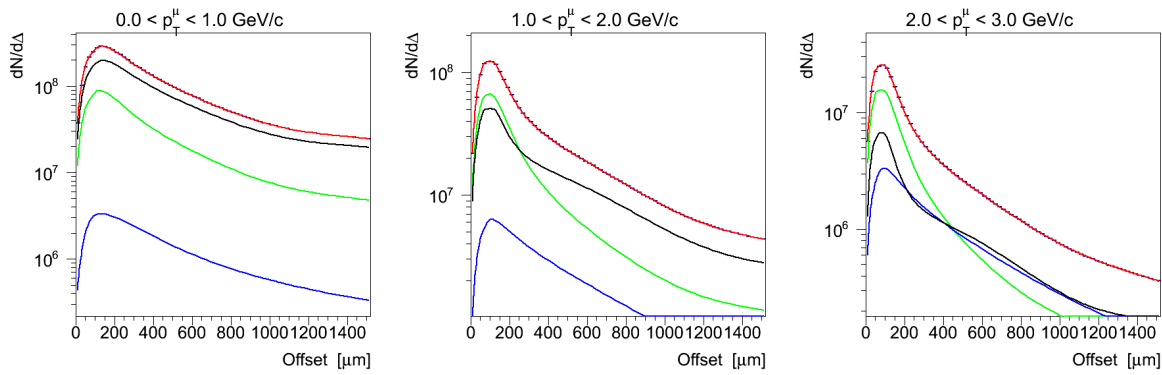


Figure 2.25: *Offset distributions of muons for three p_T bins. The red histogram is the sum of muons originating from charm decays (green), beauty decays (blue) and background (black).*

The global offset distributions are built, for each p_T bin, by adding the open charm, open beauty and background offset distributions, obtained as explained above. These global distributions are then

fitted with the superposition of the three expected contributions:

$$F = C \cdot f_c + B \cdot f_b + D \cdot f_d \quad (2.8)$$

where f_c, f_b, f_d are the MC templates for charm, beauty and background components, and C, B, D are free parameters corresponding to the normalisations of the three components.

The results of the combined fits are displayed in Figure 2.25 for three p_T bins only, although we are able to perform such studies up to the 5–7 GeV/ c p_T range. At higher p_T , the limited MC statistics limits our capability of performing any reliable parameterisation. The global distributions are well described by the three-component fits, even at low- p_T ($p_T \lesssim 1$ GeV/ c), where the background component is dominant.

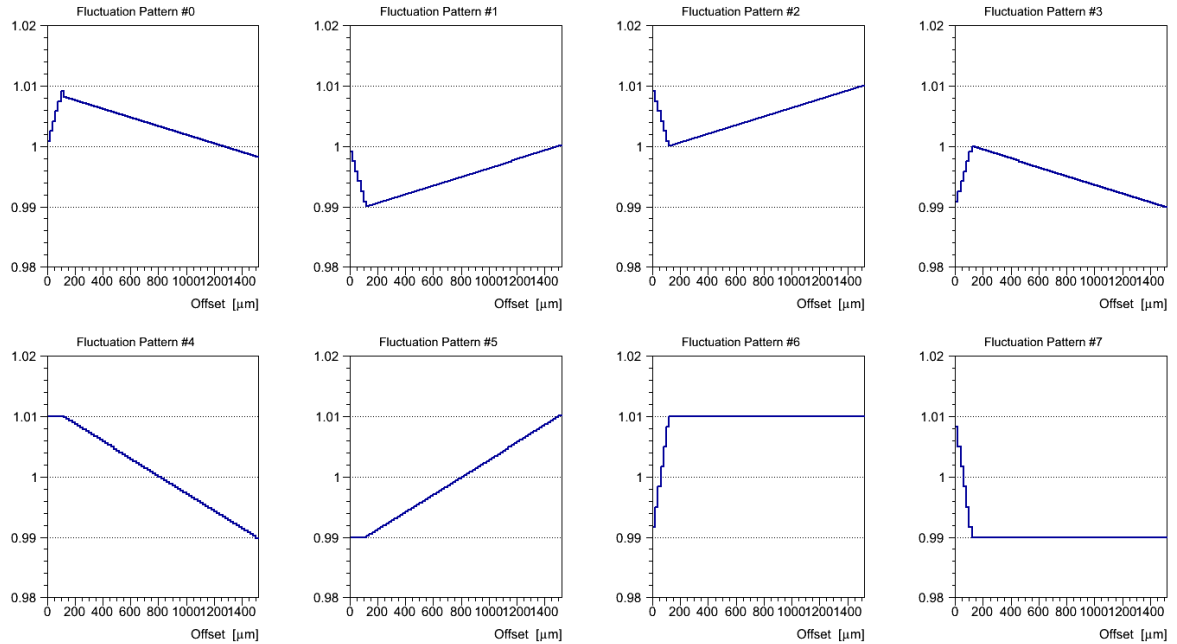


Figure 2.26: Eight distortion patterns considered to simulate the ignorance of the shape of the offset distribution. In the shown example, a 1% amplitude of the distortion is applied.

In these first fits, we assumed the MC template of each component to be perfectly known: however, as it can be easily argued, this will not be the case in a realistic experimental scenario. For example, the offset distribution of the background muons may be affected by unknown nuclear effects, not taken into account in the Monte Carlo simulations [83].

We consider three sources of systematic uncertainties, which could distort the perfect MC templates associated to the offset distributions.

The first source of systematic uncertainty is the one coming from the spatial resolution of the primary vertex, with respect to which the offset is evaluated. As pointed out earlier, we assume in these simulations a vertex resolution of 50 μm in all direction. To estimate our sensitivity to the vertex resolution, we change it by $\pm 10\%$ with respect to its nominal value: the corresponding systematic uncertainty is estimated by using the deformed MC templates, to fit the offset distributions extracted from the templates having the nominal pointing resolution.

The second source of systematic uncertainty is the one coming from the selection cuts applied to optimise the S/B ratio. In this case, we estimate the corresponding systematic uncertainty by varying

Table 2.8: Expected statistical and systematic uncertainties on the evaluation of the muon yield from open charm decays.

p_T [GeV/c]	Stat. Err. [%]	Template Syst. Err. [%]		IP Syst. Err. [%]
		$a = 1\%$	$a = 2\%$	
0 – 1	0.04	10	21	7
1 – 2	0.02	3	5	8
2 – 3	0.03	2	3	6
3 – 4	0.12	3	7	7
4 – 5	0.16	2	5	2
5 – 7	0.20	3	5	6

Table 2.9: Expected statistical and systematic uncertainties on the evaluation of the muon yield from open beauty decays.

p_T [GeV/c]	Stat. Err. [%]	Template Syst. Err. [%]		IP Syst. Err. [%]
		$a = 1\%$	$a = 2\%$	
0 – 1	2.2	79	413	500
1 – 2	0.23	25	51	65
2 – 3	0.12	6	13	30
3 – 4	0.11	4	7	14
4 – 5	0.09	2	3	7
5 – 7	0.12	2	3	6

the applied cuts within $\pm 10\%$, which induced a variation of $\pm 7\%$ on the yield of the extracted signal for both charm and beauty.

Finally, to include any other additional unknown effects, which could distort the MC templates, we distorted them according to the patterns shown in Figure 2.26. Once more, the deformed MC templates are then used to perform a new fit to the global offset distributions obtained from the nominal templates.

The results are summarised in Tables 2.8 and 2.9 for the extraction of open charm and open beauty respectively. The three sources of systematic uncertainties are added quadratically, and the final results, the yields from charm and beauty decays with resulting statistic and systematic uncertainties, are displayed in Figure 2.27.

These results clearly show that it is possible to unfold open charm decay down to zero p_T with a systematic uncertainty of the order of 20%. Even if muons from open beauty decays can be extracted down to low- p_T , the level of the systematic uncertainty limits the quality of this result (Table 2.9). The open beauty signal can be reliably unfolded only for $p_T \gtrsim 2$ GeV/c.

To conclude, we have shown that the presence of the MFT greatly improves the measurement of open heavy-flavour production in the single-muon channel, with respect to the current Muon Spectrometer setup: firstly, because it extends the signal extraction to a p_T range not accessible by the current spectrometer; secondly, because the analysis strategy based on the decomposition of the offset distributions (not affordable without the MFT) offers the possibility to separately extract charm and beauty contributions.

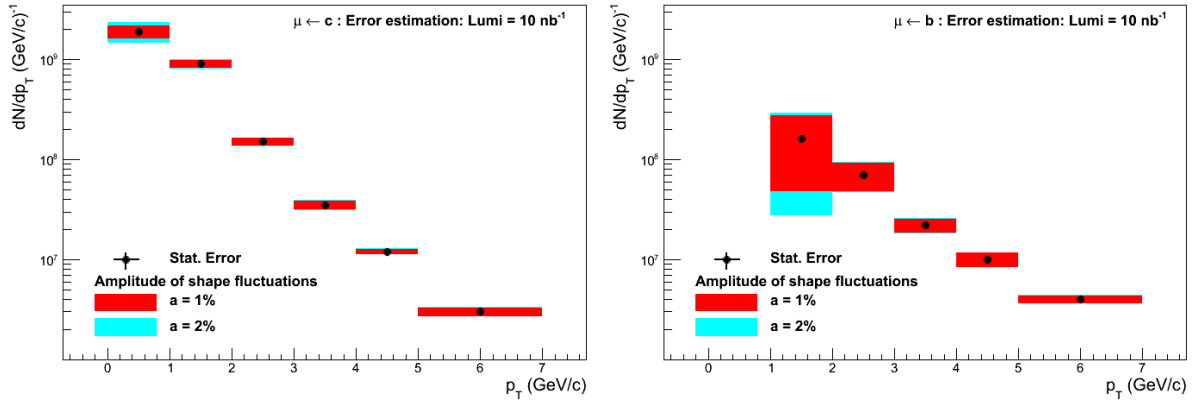


Figure 2.27: Transverse momentum distributions of single muons from charm (left) and beauty (right) decays with their respective statistical and systematical uncertainties expected in the measurement. 0-10 % Pb-Pb collisions at $\sqrt{s_{NN}} = 5.5$ TeV are considered, in a 10 nb^{-1} integrated luminosity scenario.

2.5.4 Expected Yields and Signal Extraction in Dimuons

As already explained, open heavy-flavour production can also be studied in the dimuon channel, by considering the distribution of the weighted offset of muon pairs, defined as $\Delta_{\mu\mu} = [0.5 \cdot (\Delta_{\mu 1}^2 + \Delta_{\mu 2}^2)]^{0.5}$, with $\Delta_\mu = [0.5 \cdot (\delta x^2 V_{xx}^{-1} + \delta y^2 V_{yy}^{-1} + 2\delta x \delta y V_{xy}^{-1})]^{0.5}$, where δx and δy are the x and y offset of the muon track, and V^{-1} is the inverse of the covariance matrix accounting for the combined uncertainty on the track and the vertex position. In order to stay clear of strong contaminations coming from prompt dimuons of resonances, the dimuon weighted offset distributions are projected into two mass regions ranging from the ϕ peak to the charmonium family, and from the charmonium to the bottomonium family. More precisely, we define the following mass regions:

1. “Low Mass”: $1.2 < M_{\mu\mu} < 2.8 \text{ GeV}/c^2$;
2. “High Mass”: $4.0 < M_{\mu\mu} < 9.0 \text{ GeV}/c^2$.

For each mass region the yield of direct charm, direct beauty and background dimuons is estimated by identifying these contributions in the full HIJING simulations. For the sake of clarity, we remind here, how these three components are defined:

open charm: Any pair of muons, where both muons has a D meson as their parent particle; parent D mesons are explicitly required not to come from the decay of a B meson.

open beauty: Any pair of muons, where both muons has a B meson as their parent particle;

background: Any pair of muons not satisfying the previous definitions, including in particular any possible combinations between muons from π , K, D and B mesons.

These definitions enable an easy comparison between experimental measurements and theoretical predictions. The expected dimuon yields for the direct charm, direct beauty and background contributions are reported in Table 2.10, where the estimates for the low-mass and high-mass regions are given as a function of the dimuon p_T . Work is currently in progress to include the component of beauty-charm chain decays in the beauty component, as it is done in the analysis of the single muon channel.

Table 2.10: Expected statistics for direct charm, direct beauty and background dimuons in the two mass regions of interest for the open heavy-flavour analysis in the dimuon channel.

“Low Mass Region”: $1.2 < M_{\mu\mu} < 2.8 \text{ GeV}/c^2$			
$p_T [\text{GeV}/c]$	Charm [$\times 10^3$]	Beauty [$\times 10^3$]	Background [$\times 10^3$]
0 – 1	1 400	36	15 800
1 – 2	1 940	76	24 800
2 – 3	1 300	124	19 600
3 – 4	438	118	6 900
4 – 5	155	74	2 570

“High Mass Region”: $4.0 < M_{\mu\mu} < 9.0 \text{ GeV}/c^2$			
$p_T [\text{GeV}/c]$	Charm [$\times 10^3$]	Beauty [$\times 10^3$]	Background [$\times 10^3$]
0 – 1	140	67	321
1 – 2	245	154	1 600
2 – 3	137	165	1 500
3 – 4	93	131	1 370
4 – 5	37	89	651

The global dimuon offset distributions are built, as in the case of the single-muon analysis, by weighting the MC distributions of the three components (direct charm, direct beauty and background) according to the expected yields compiled in Table 2.10. In order to get rid of the statistical fluctuations coming from the limited MC sample, the raw MC distributions are parameterised with a variable-width Gaussian. This function is found to give a satisfactory description of the MC distributions, as it can be seen in Figure 2.28, where the dimuon offset distributions for the direct charm, direct beauty and background contributions are compared with their parameterisations.

In the chosen analysis strategy the weighted offset distributions obtained for each p_T -bin are then fitted with the superposition of the three expected contributions. Each contribution is described by the MC template defined by the parameterisations of the raw MC, with the normalisations treated as free parameters without any specific initial assumption on their values.

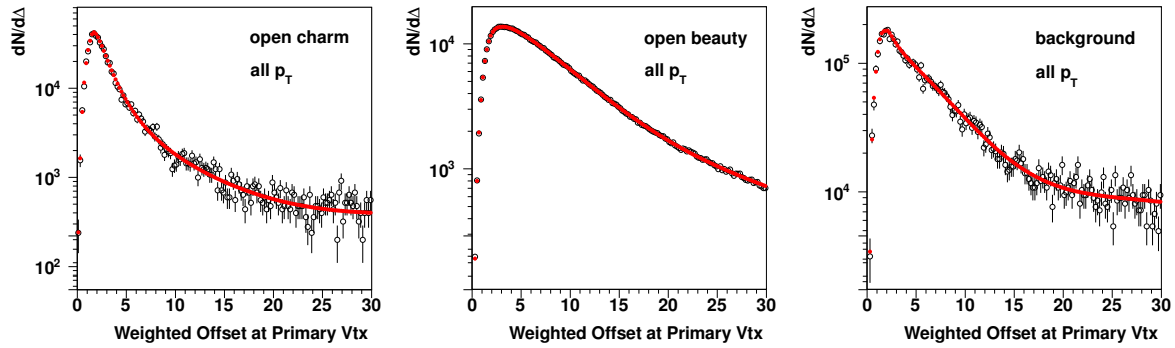


Figure 2.28: Weighted offset distributions for open heavy-flavour and background dimuons, as obtained from MC simulations (black, open circles), compared with the parameterisation given by a variable width Gaussian (red, full circles).

In order to account for using the Monte Carlo samples as fitted “data” (see Figure 2.29) and to build the templates used for the fit, we apply the same templates distortion exercise as it was done for the single muon analysis (see Figure 2.26). The estimation of the related uncertainties, currently in progress, will be part of a dedicated effort aiming to develop a common analysis strategy for the investigation of the dimuon continuum, including prompt sources not cited in this Section (QGP radiation at intermediate masses, Drell-Yan at high masses).

2.5.5 Contribution of the MFT to the ALICE Heavy-Flavour Program

The total charm-production cross section is an essential input of the charmonium models. As described above, the MFT addition to the Muon Spectrometer will allow us to perform a precise measurement of this cross section.

The charm and beauty separation opens the path towards the study of energy loss of heavy quarks in the QGP at forward rapidities. The difference in the energy loss of heavy quarks, light quarks and gluons reflects in a hierarchy of the nuclear modification factors of light, charmed and beauty hadrons as $R_{AA}^\pi < R_{AA}^D < R_{AA}^B$. In the context of the MFT, this study can be performed by measuring the ratio of the nuclear modification factors of muons from charm and beauty, R_{AA}^B/R_{AA}^D . Figure 2.30 shows a possible R_{AA}^B/R_{AA}^D measurement with the expected uncertainties using the MFT in addition to the Muon Spectrometer. The uncertainties are compared with the ones expected in the ALICE central rapidity region using the new ITS [1], where the measurement is done via the separation of prompt and non-prompt D^0 . We can see that the MFT measurement complements well the central rapidity measurement. We should note that higher p_T values can also be accessed by the MFT measurement: they do not appear in the figure, due to lack of statistics in the simulations.

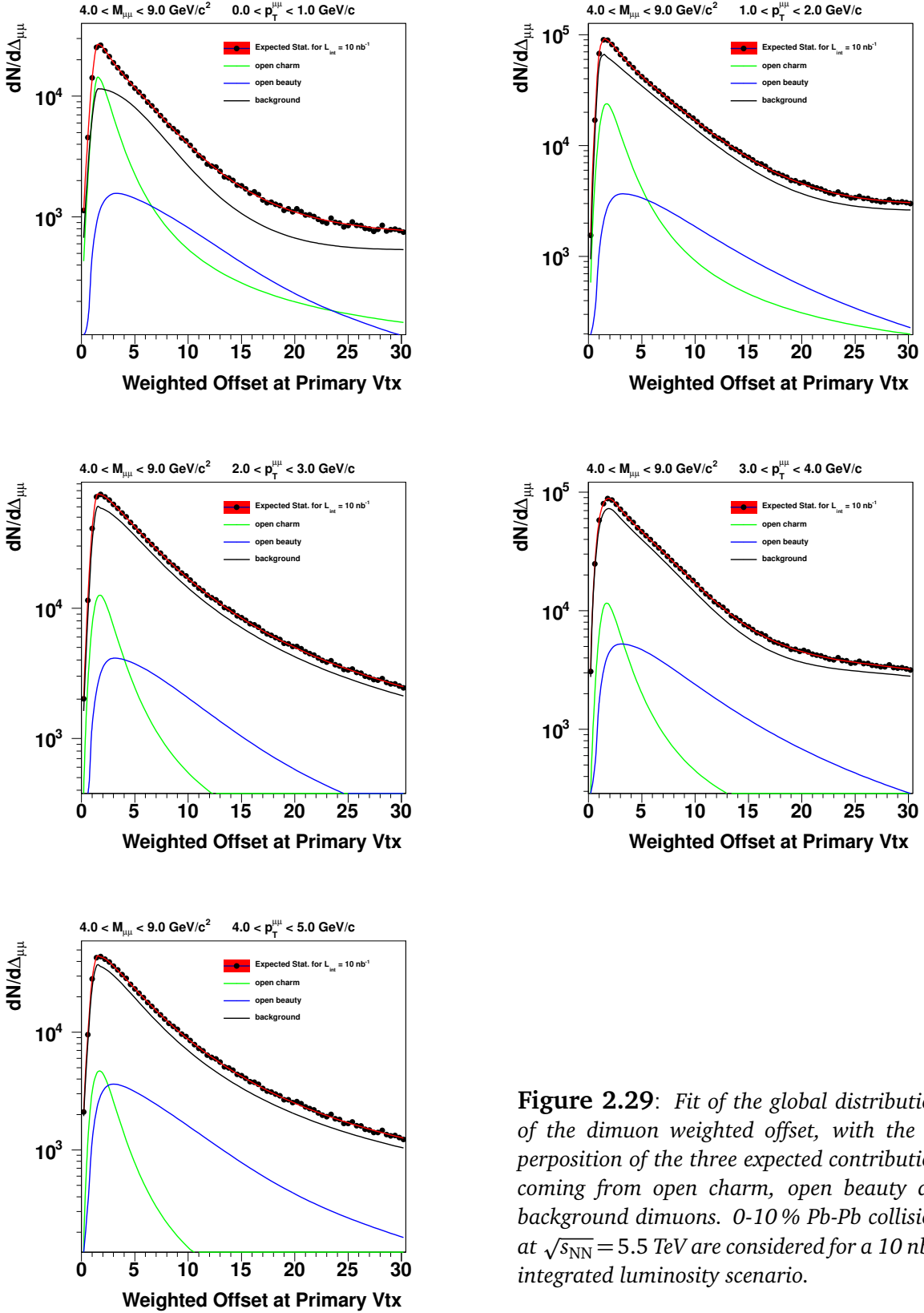


Figure 2.29: Fit of the global distributions of the dimuon weighted offset, with the superposition of the three expected contributions coming from open charm, open beauty and background dimuons. 0-10 % Pb-Pb collisions at $\sqrt{s_{NN}} = 5.5 \text{ TeV}$ are considered for a 10 nb^{-1} integrated luminosity scenario.

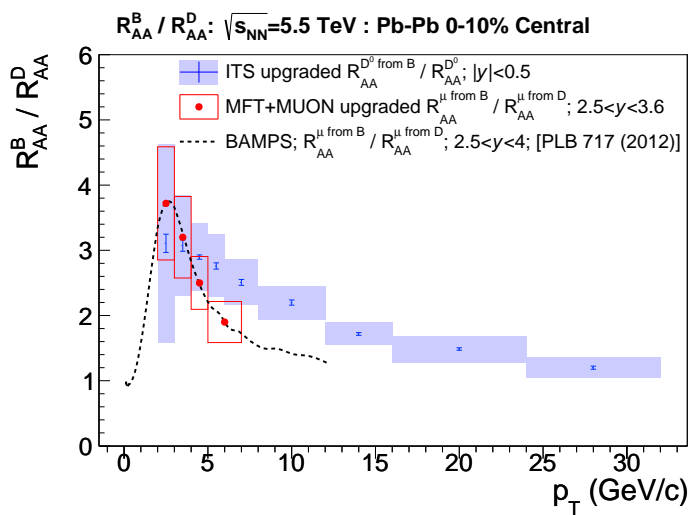


Figure 2.30: Ratio of the nuclear modification factors of open charm and beauty. Comparison between the uncertainties expected with the new ITS in the central rapidity domain using the non-prompt and prompt D^0 measurement (blue area) [1] and the ones expected using the measurement of single muon coming from open charm and beauty using the MFT and the upgraded Muon Spectrometer (red points). Error bars represent the statistical uncertainties, while the boxes show the systematics uncertainties. The central values of the MFT points are chosen according to a theoretical prediction using the partonic transport model BAMPS (Boltzmann Approach to Multi-Parton Scatterings) [84], which is also displayed directly as a dashed line.

2.6 Low Mass Dimuons in Central Pb–Pb

As discussed in the previous chapter, the low mass ($M_{\mu\mu} < 1.5 \text{ GeV}/c^2$) dimuon region results from the superposition of various sources. The most interesting signals in this region are the decays of the light neutral mesons ρ , ω and ϕ – with the line shape of the ρ meson being a major item to address –, as well as the prompt dimuons directly radiated from the QGP phase. Here, the main source of the background is represented by the combinatorial pairs of muons coming from uncorrelated semimuonic decays of light-flavoured mesons, mainly pions and kaons, copiously produced in high-energy nuclear collisions. As far as the low mass prompt dimuons are concerned, in addition, dimuons coming from the open charm and open beauty processes must also be considered and treated as a source of background.

The strategy envisaged for the analysis of the low mass dimuon spectrum, described in details in what follows, starts with the simulation of all the signal and background sources. These simulations are then exploited to identify and optimise the cuts and the selections which should at the same time:

- improve the quality of the signal (in particular by improving the correct matching rate between the MUON tracks and the MFT clusters);
- reject the largest fraction possible of background, to improve the signal to background ratio.

Once the selections and the cuts are optimised, a mass spectrum is built by adding together all the signal and background sources, each component weighted by a factor accounting for the expected yield at the given integrated luminosity, the overall reconstruction efficiency for the process, and finally the effect of the selection cuts imposed after the reconstruction.

All simulations superimpose a central HIJING Pb–Pb underlying event with overlaid specific signal, generated with the primary vertex in the nominal interaction point, to a second HIJING central Pb–Pb event generated with the primary vertex distributed according to the expected LHC parameters.

2.6.1 Signal and Background Simulations

The signal sources for the low-mass prompt dimuons, forming the so-called “hadronic cocktail”, are the 2-body and the Dalitz decays of the light neutral mesons: $\eta \rightarrow \mu\mu\gamma$, $\eta \rightarrow \mu\mu$, $\rho \rightarrow \mu\mu$, $\omega \rightarrow \mu\mu\pi^0$, $\omega \rightarrow \mu\mu$, $\eta' \rightarrow \mu\mu\gamma$, $\phi \rightarrow \mu\mu$. The Dalitz decay of the η' meson, however, represents such a small contribution that it is not considered in this case. No in-medium modification is taken into account in the simulation of the hadronic cocktail processes.

All the ingredients of the hadronic cocktail are simulated by means of a parametric generator. To speed-up the simulations, kinematic constraints are imposed to fit the geometrical and kinematic acceptance of the muon spectrometer:

- dimuon rapidity range: from -4.5 to -2.0 ;
- muon polar angle range: from -9° to -2° ;
- muon momentum range: $p > 4 \text{ GeV}/c$.

Concerning the background, we follow the same strategy as for the charmonium analysis: we extract the muons directly from the HIJING simulations, where all the background sources are naturally contained with appropriate yields and kinematic distributions. The background is evaluated, both in normalisation and kinematics, by building event by event every possible muon pair disregarding the origin of the muons (with the exception of the muons coming from neutral resonances –

i.e. the signal we are interested in – which are discarded when building the background pairs). The open charm and the open beauty processes, here treated as background sources, are also naturally contained in the complete HIJING simulations as we saw in Section 2.5 devoted to the open heavy-flavour study.

Again, the structure of the present section follows that of the previous ones. First, we describe and justify the cuts and the selections applied to our sample; then, we characterise the performance of the proposed selections in term of background rejection. Finally, we move to the discussion of the analysis strategy for the extraction of the signals, i.e. the continuum represented by the (broadened) line shape of the ρ meson and the mass spectrum of the prompt dimuons radiated from the QGP phase – this latter contribution will be referred to, in what follows, as “QGP radiation”.

2.6.2 Cuts and Selections

The natural choice of parameters one may consider to select prompt, correctly matched dimuons, is represented by the χ^2 of the global tracks and the offset of single muons and dimuons.

The cut region in the χ^2 -offset plane is chosen by (i) looking at the distributions corresponding to a pure sample of good MUON-MFT matches for the signal – to improve the matching efficiency of the selected sample – and (ii) comparing the distributions corresponding to muons from signal and background – to improve the signal/background ratio.

Taking the $\phi \rightarrow \mu\mu$ process as example, we show in Figure 2.31 the χ^2 -offset distribution for a pure sample of correctly matched muons (left panel) and for the whole sample where both good and bad matches are present (centre panel). As one can see, the distribution for the correctly matched muons is concentrated in a small corner at low χ^2 and low offset. The cut region is proposed as an elliptical cut defined by half-axes of $\chi^2 < 1.5$ and offset $< 250 \mu\text{m}$. This choice allows one to improve the fraction of correct matches in the final sample, rejecting at the same time a large fraction of tracks coming from background processes, whose χ^2 -offset distribution is shown in the right-hand panel of Figure 2.31.

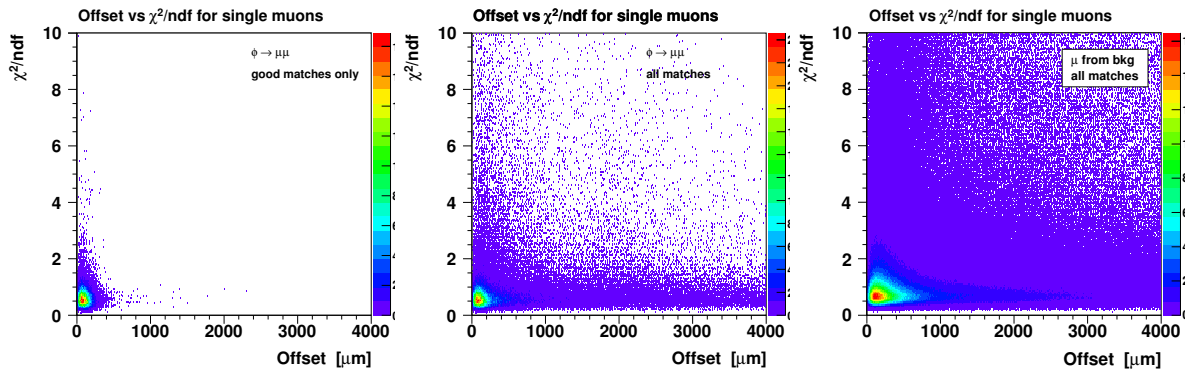


Figure 2.31: Left and centre panels: χ^2 -offset distributions for the muons of the $\phi \rightarrow \mu\mu$ process: pure sample of correctly matched muons (left) and whole sample containing good and bad matches (centre). Right panel: χ^2 -offset distributions for the muons of the low mass dimuons from HIJING. 0-10 % Pb-Pb collisions at $\sqrt{s_{\text{NN}}} = 5.5 \text{ TeV}$ are considered here.

2.6.3 Rejection Power

In order to characterise the efficiency of the chosen cuts, the fraction of rejected dimuons (the “rejection power”) is evaluated for the various sources of signal and background. In particular, the

dependence of the rejection power on the dimuon p_T is considered in order to evaluate the impact on the physics topics we are interested in. The results are shown in Figure 2.32. In the left panel we consider the rejection power of two combined Muon Spectrometer based cuts: tracker-trigger matching and $p_T > 0.7 \text{ GeV}/c$ for single muons; the impact of these cuts is evaluated on top of the geometrical acceptance cut $-3.6 < \eta - 2.5$ applied by default on single muons. As expected, we have a more powerful rejection for the muons coming from the background sources than for the muons coming from the processes of the hadronic cocktail. The right panel of Figure 2.32 shows the additional rejection power when requesting the MFT based cuts (cut on single muons $\chi^2 > 1.5$ and offset $> 250 \mu\text{m}$). Here, too, the rejection is found to be stronger for background than for signal dimuons.

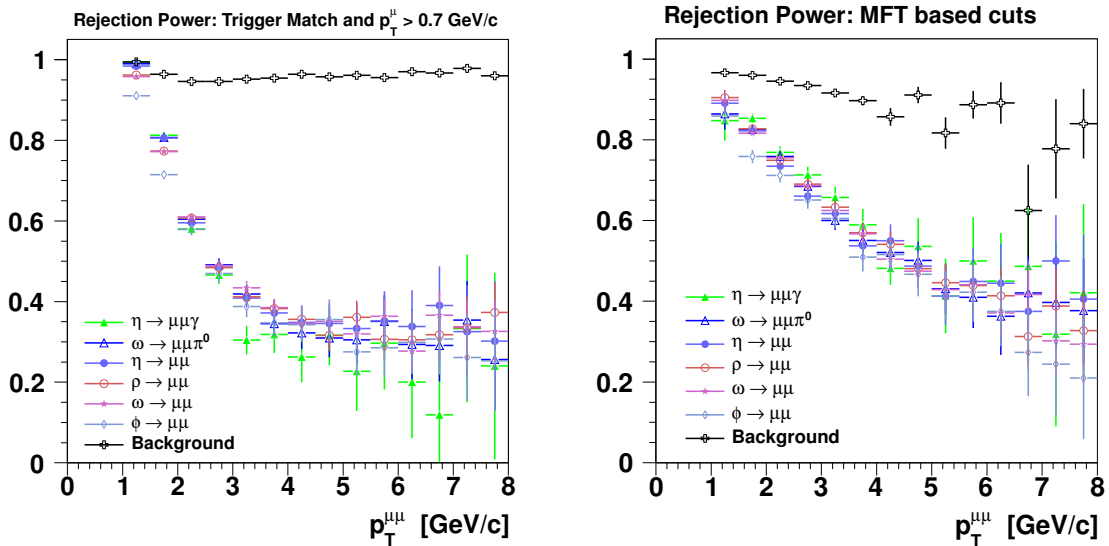


Figure 2.32: Rejection power as a function of dimuon p_T , for signal and background pairs, due to the combined Muon Spectrometer based cuts (left panel) on tracker/trigger matching and p_T , and the MFT based cuts (right panel) single muon χ^2 and offset. 0–10 % Pb-Pb collisions at $\sqrt{s_{\text{NN}}} = 5.5 \text{ TeV}$ are considered here.

We should note here that the choice of the sharp p_T cut $p_T > 0.7 \text{ GeV}/c$ for the single muons is a compromise between two major p_T -dependent factors:

1. the probability of having a correct match between the track reconstructed in the Muon Spectrometer and the clusters measured in the MFT;
2. the p_T acceptance for the reconstructed dimuons (in particular, the lowest accessible p_T).

As we already noted along the document, improving the first factor means considering higher p_T of single muons, see for example Figure 2.6. On the contrary, one can easily guess that lower p_T of single muons are needed to cover lower p_T of the muon pairs. This is particularly true for low mass dimuons, since close to the $2m_\mu$ kinematic threshold it can be shown that $p_T^{\mu_1} \sim p_T^{\mu_2} \sim 0.5 \cdot p_T^{\mu\mu}$. A direct consequence is that, while the cut $p_T > 1.0 \text{ GeV}/c$ for the single muons allows to measure J/ψ dimuons down to zero p_T , imposing this same cut to low mass dimuons would limit the analysis to transverse momenta larger than $\sim 2 \text{ GeV}/c$, see Figure 2.33.

For these reasons, the cut $p_T > 0.7 \text{ GeV}/c$ considered here for the single muons, allows to measure low mass dimuons down to $p_T \sim 1.4 \text{ GeV}/c$. Dedicated studies are ongoing, as discussed elsewhere

in the present document, for improving the MUON–MFT matching algorithm in the p_T range below 1.5 GeV/c, exploiting the bending of the track due to the L3 magnetic field.

For these very same reasons, finally, any effort should be made in the optimisation of the detector (including the choice of the pixel technology) in order the tracking quality for low p_T muons (at least down to $p_T \sim 0.5$ GeV/c) to be preserved as far as possible.

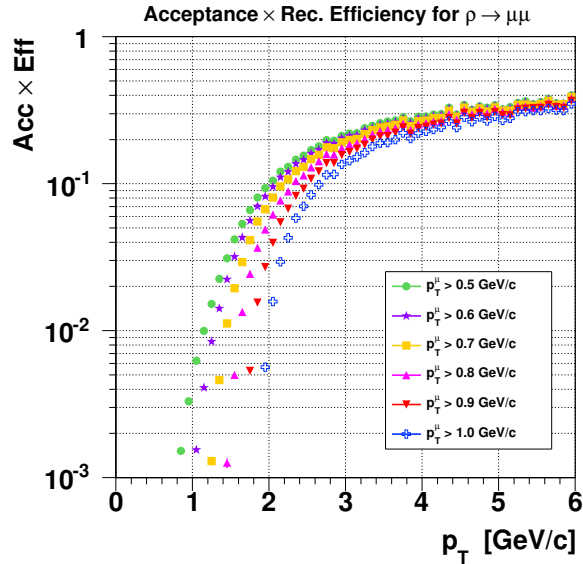


Figure 2.33: Acceptance \times efficiency for the decay $\rho \rightarrow \mu\mu$ (taken as representative of the hadronic cocktail responsible for the low mass dimuon production) as a function of the p_T of the dimuon, for various choices of the threshold imposed on the p_T of the single muons.

2.6.4 Mass Resolution

The improvement of the pointing accuracy for the muon tracks by means of the matching between the MUON tracks and the MFT clusters also offers a more precise measurement of the opening angle for prompt dimuons, and thus improves their mass resolution. The invariant mass of a dimuon can in fact be expressed for small opening angles θ between muons of momenta p_1 and p_2 as:

$$M_{\mu\mu} = \sqrt{2p_1 p_2 (1 - \cos \theta)} \approx \sqrt{p_1 p_2 \theta^2}, \quad (2.9)$$

For the low-mass pairs the error on the measured mass is dominated by the angular error due to the multiple scattering in the absorber. For this reason, the measurement of muon angles by the MFT before they enter into the absorber allows to strongly improve the dimuon mass resolution. We recall once more, on the contrary, that the MFT will not improve the measurement of the two momenta p_1 and p_2 (dominant contribution to the mass resolution for high mass dimuons), due to the low transverse field of the ALICE solenoid in the MFT region.

The left plot of Figure 2.34 compares the reconstructed $\omega \rightarrow \mu\mu$ mass distributions with and without matching in the MFT, while the matched spectrum fitted by a superposition of Gaussian and “Crystal Ball” parameterisations is shown in the right plot. We note that the wider Gaussian contribution corresponds to dimuons with one or both muons incorrectly matched³.

³ The treatment of this “fake-match” contribution is especially important in the analysis of the low mass dimuons, since the probability to have a fake match is higher for softer muons. Here, two strategies can be envisaged: either the dimuon component containing one or two fake matches is separately evaluated by means of an appropriate event mixing technique, or the component is retained in the analysis, as a part of the signal having a degraded kinematics. This latter approach, already considered in the case of the analyses of the open heavy-flavour and the charmonium states, is

In Figure 2.35 we furthermore show the effect of the p_T range on the proportion between signal (Crystal Ball) and background (Gaussian). The left and right panels refer to the dimuon p_T ranges $1 < p_T < 2 \text{ GeV}/c$ and $3 < p_T < 4 \text{ GeV}/c$, respectively: as expected, the contribution from fake matches is larger at low p_T . It is worth to note, that these results have been obtained in the case of two central Pb–Pb pile-up events corresponding to very high background conditions.

The relevant fit parameters for the η , ω and ϕ resonances are compiled in Table 2.11, where their dependence as a function of p_T is also considered.

p_T [GeV/c]	σ_m [MeV/c 2]					
	$\eta \rightarrow \mu\mu$		$\omega \rightarrow \mu\mu$		$\phi \rightarrow \mu\mu$	
	w/o MFT	w/ MFT	w/o MFT	w/ MFT	w/o MFT	w/ MFT
All p_T	44	8	46	12	51	15
1 – 2	44	11	47	16	51	16
2 – 3	41	6	45	10	49	15
3 – 4	41	6	45	11	48	14

Table 2.11: Mass resolution (σ of Crystal Ball fit) for two-body decays of the η , ω and ϕ mesons with and without the MFT.

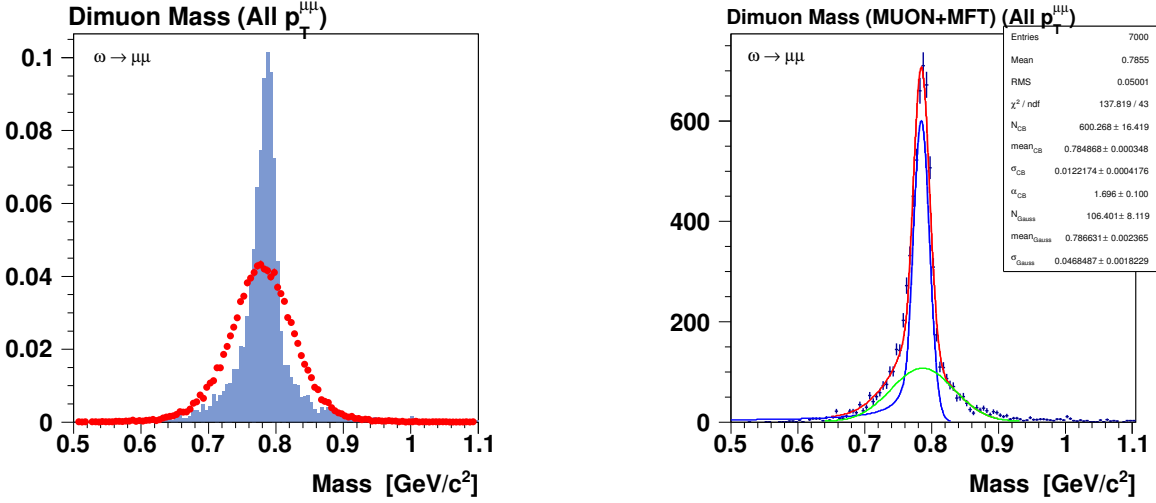


Figure 2.34: Left: Comparison between the normalised mass distributions for the $\omega \rightarrow \mu\mu$ process, before (red points) and after (blue profile) the introduction of the MFT and the MFT-based selections. Right: Fit of the MFT mass distributions using a superposition of a Crystal Ball and a Gaussian. 0–10% Pb–Pb collisions at $\sqrt{s_{\text{NN}}} = 5.5 \text{ TeV}$ are considered.

also adopted here; the advantage is that Monte Carlo simulations performed in an appropriate multiplicity environment automatically give the shape and the normalisation of this component: the corresponding systematic uncertainties can be safely kept under control by adopting reconstruction settings giving a stable performance of the correct matching rate, as discussed in Section 2.3.2.

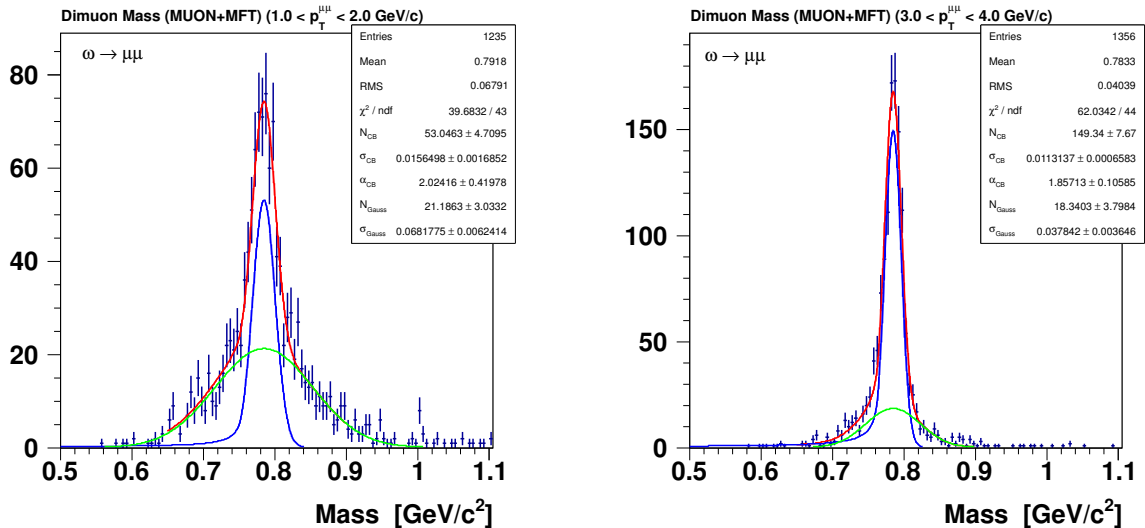


Figure 2.35: Mass distribution for the two-body decay of the ω meson for two different p_T bins: $1 < p_T < 2 \text{ GeV}/c$ (left) and $3 < p_T < 4 \text{ GeV}/c$ (right). The importance of the contribution described by the Gaussian (green, broader curve) increases at low p_T , due to worse MUON-MFT matching for the single muons. 0-10 % Pb-Pb collisions at $\sqrt{s_{\text{NN}}} = 5.5 \text{ TeV}$ are considered.

2.6.5 Expected Yields and Signal Extraction

Once the various signal and background sources have been simulated, they can be combined together according to the expected yields, in order to build the mass spectrum relative to the foreseen 10 nb^{-1} integrated luminosity. In particular, we are interested in building such a spectrum in the two scenarios in which the MFT is excluded and included in the analysis.

When evaluating the performance expected for the low-mass dimuon physics, all the cuts and selections described above have been applied. In addition, the kinematic cut $p_T > 1 \text{ GeV}/c$ as defined by the lowest reach of the ALICE Muon Spectrometer is applied on the dimuon sample. The theoretical predictions for the QGP radiation and the in-medium modified line shapes for the ρ and ω , available from [85], also account for these cuts and selections. The superposition of the expected sources is shown in Figure 2.36 for the two scenarios with and without MFT. The contributions taken into account are:

- The hadronic cocktail of the “vacuum” processes described in Section 2.6.1, without the $\rho \rightarrow \mu\mu$ contribution.
- The open charm contribution, being the major component of the physics (i.e. correlated) continuum in the low mass dimuon region.
- The sum of the ρ and ω in-medium modified line shapes.
- The thermal radiation of dimuons (virtual photons) from the QGP

The evaluation of the last two contributions is based on a hadronic many-body approach, which allows an estimate of the perturbative emission rates and allows to model thermal dilepton radiation from the hadronic phase and the QGP including medium-modified spectral functions and a realistic space-time evolution. This approach provides a reasonably good quantitative description of dilepton

data over a wide range of collision energies [86–88]. As one can see, if its predictions will stay valid for the LHC energies, the reconstructed mass spectrum should contain measurable contributions from the QGP radiation and in-medium effects on the ρ - ω line shape, even taking into account the non-negligible p_T cut imposed by the detector on the dimuons.

The data samples presented in Figure 2.36 are normalised to the statistics expected with 10 nb^{-1} ; the associated errors, shown on top of the data points, are dominated by the systematic and statistical uncertainties coming from the subtraction of the combinatorial background. The improvement of the S/B given by the MFT-based cuts, then, allows us to reduce the uncertainties coming from the subtraction of the background. For the 2-body decays of the resonances, the S/B is further increased by the dramatic improvement of the mass resolution. A precise evaluation of the expected systematic error on the combinatorial background subtraction is still undergoing, needing a significant computational effort. A realistic target value is represented by the 0.25 % precision considered in what follows, which would translate to a 3 % uncertainty on the extracted signal at masses of $0.5 \text{ GeV}/c^2$.

In order to isolate the “QGP signatures” represented by the thermal dimuon radiation and the in-medium modified line shapes of the ρ (and ω) mesons, the known and well identifiable sources of the hadronic cocktail – for which no in-medium effect is expected – must be subtracted from the superposition of the correlated dimuon signals presented in Figure 2.36. This identification will be performed by means of a fit on the mass spectrum; again, systematics uncertainties on the shape and normalisation of the subtracted sources must be evaluated and propagated: in the present evaluation, we estimated an overall 10 % systematic uncertainty. This same uncertainty is applied to the subtraction of the open charm contribution.

The remaining continuum, presented in Figure 2.37 dressed with the uncertainties coming from the subtraction of the combinatorial background, the hadronic cocktail and the open charm contributions, will be described in terms of the processes predicted by the theoretical models. Eventually, this continuum being corrected for the acceptance and reconstruction efficiency effects, a direct comparison with the theoretical predictions could be established. The typical uncertainties expected for such a measurement in an upgraded scenario with the MFT are of the order of $\sim 20\%$ at $M_{\mu\mu} \sim 0.5 \text{ GeV}/c^2$; without the MFT, the current Muon Spectrometer setup would be hardly able to identify the QGP signatures, the typical uncertainty at $M_{\mu\mu} \sim 0.5 \text{ GeV}/c^2$ being estimated of the order of $\sim 70\%$.

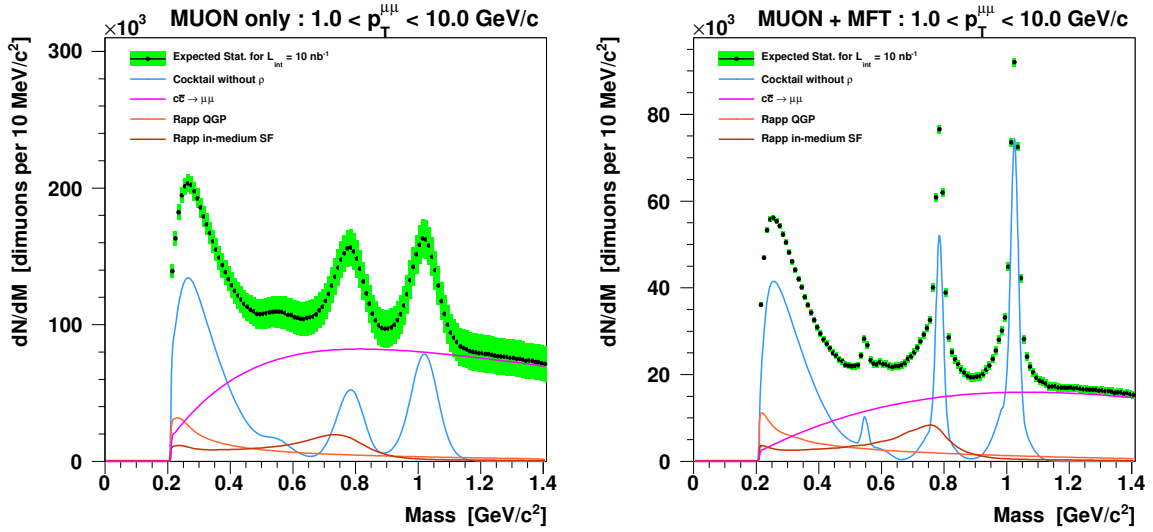


Figure 2.36: Expected low mass dimuon spectrum in 0-10 % central Pb–Pb collisions at $\sqrt{s_{\text{NN}}} = 5.5 \text{ TeV}$ after subtraction of the combinatorial background, normalised to an integrated luminosity of 10 nb^{-1} without (left panel) and with (right panel) the addition of the MFT to the ALICE Muon Spectrometer.

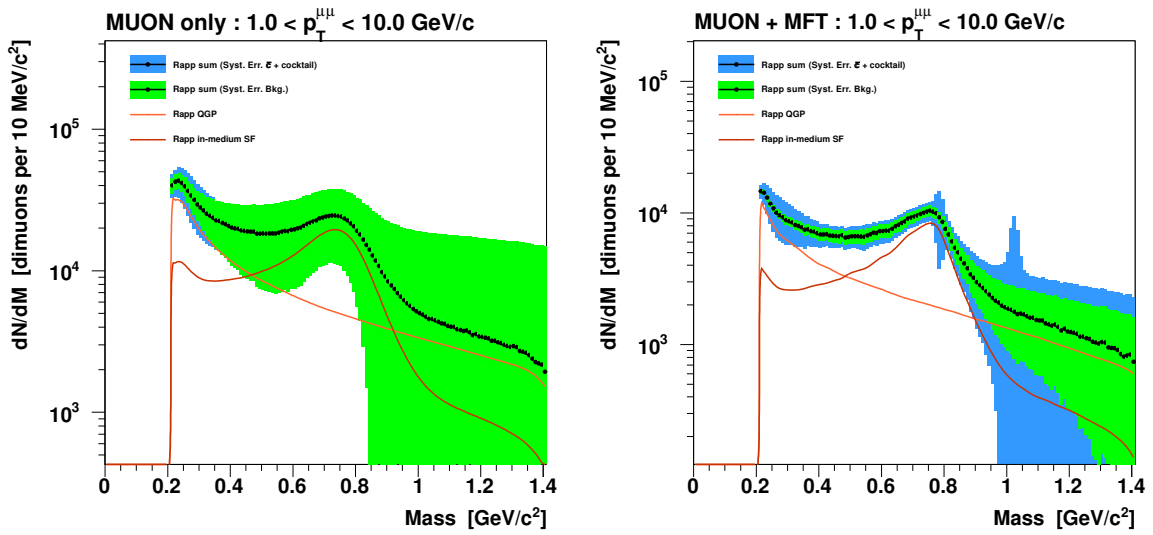


Figure 2.37: Expected sensitivity to the measurement of QGP signatures in 0-10 % central Pb–Pb collisions at $\sqrt{s_{\text{NN}}} = 5.5 \text{ TeV}$ in a $L_{\text{int}} = 10 \text{ nb}^{-1}$ scenario without (left panel) and with (right panel) the MFT.

Chapter 3

Detector Technology and Integration

The Muon Forward Tracker requirements imply a pixel detector with high granularity (pixel pitch $< 30 \mu\text{m}$) and correspondingly very small spatial resolution allowing to separate different tracks in the high density environment of Pb–Pb collisions. In addition, low material budget of the order of $\langle x \rangle / X_0 \sim 0.4\%$ per plane is mandatory to avoid multiple scattering effects and a deterioration of the resolution. The MFT should also be able to support collisions rates expected for ALICE at the HL-LHC, i.e. 200 kHz in pp and 50 kHz in Pb–Pb collisions, translating into additional requirements for the sensitive devices: high readout speed ($t_{r/o} < 30 \mu\text{s}$) and adequate radiation-tolerant behaviour. The low power consumption of pixel sensors is also crucial, as the MFT is located in a sealed cage, with limited space to implement the cooling system. From the beginning of the project design studies, CMOS monolithic pixel sensor technology was chosen as the reference technology for the MFT for several reasons: this technology provides interesting performance fulfilling the cited requirements, the micro-electronic engineers working on the MFT have a long expertise in the design of binary CMOS pixels sensors, and finally this technology is also the choice made by the ITS upgrade for its inner layers, which allows some cost reduction and technical exchanges during the R&D phase of the project.

3.1 CMOS Monolithic Pixel Sensor Technology

The detection principle of the monolithic pixel detector is already described in the ALICE LoI (section 3.3.3) [1]. The sensitive volume and the front-end read-out electronics are integrated into the same substrate. This technology is also cost effective because it is available through many commercial micro-electronics foundries. The reference architecture studied for the MFT is based on the improved group rolling shutter system to reduce the power consumption. The main blocks of the sensor are: in-pixel amplification close to the sensing N-well/P-epi diode, high-precision and fast front-end electronics and auto-zeroing techniques in every stage of the readout path [89], followed by zero-suppression logic circuitry [90]. Other smaller blocks and modules, such as row sequencer, DACs, memories, etc. are necessary for the sensor operation. The MFT CMOS sensor block diagrams are illustrated on Figure 3.1. The square pixels have a pitch of $25 \mu\text{m}$ to respect spatial resolution requirements in the x - y directions. In order to cope with the material budget requirement, the

sensors have to be thinned down to $50\ \mu\text{m}$ in thickness. The R&D on monolithic pixel detectors is ongoing in a common effort with the ITS R&D program. Recently, the TowerJazz $0.18\ \mu\text{m}$ CIS (CMOS Image Sensor) technology, which offers smaller feature size and several intrinsic advantages (improvement of readout time and better radiation tolerance) has been chosen. This technology has been used for a few prototypes since the end of 2011 to demonstrate the feasibility of the optimised architecture and its radiation resistance to the levels expected for the MFT planes. Results of prototypes are encouraging for the needs of the ITS and MFT [91, 92]. For a detailed presentation of the detector conceptual design and the architectures under consideration, the MFT Internal Report [91] is a reference document, as well as the ITS Upgrade Conceptual Design report [92].

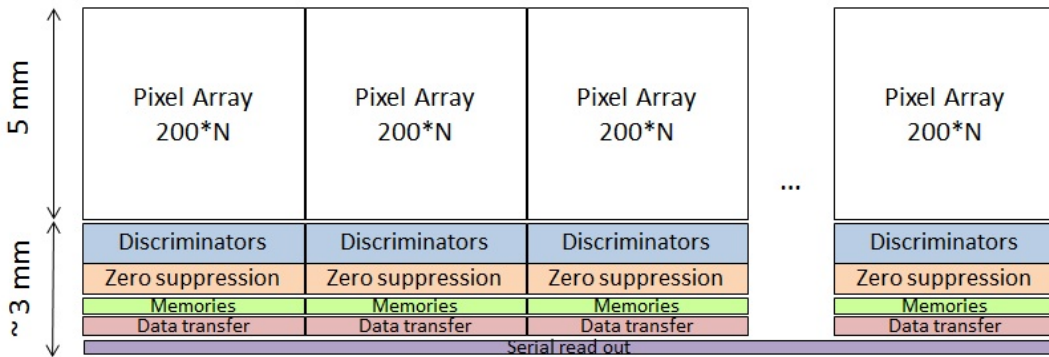


Figure 3.1: MFT CMOS sensor block diagram.

3.2 Data Flow and Readout Architecture

The conceptual readout architecture proposed for the MFT is divided into two parts: the readout located on-detector at the edges of the ladders, out of the detection acceptance, and the back-end readout located in the counting room. The readout and control systems will fit into the ALICE infrastructure and will interface with the existing (or upgraded) central system. For the local readout on-detector, the communication is proposed to be performed by the GBT (GigaBit Transceiver) versatile link developed and validated [93]. In order to assess the requirement for the MFT data flow we have considered the occupancy estimated in fig.2.3 for 0-10% central Pb-Pb collisions. This is a conservative estimation since the average occupancy is expected to be around a factor 3 smaller than that in 0-10% central collisions. A Pb-Pb collision rate of $100\ \text{kHz}$ is assumed as it is expected at the peak of the luminosity. If a conservative noisy pixel rate of 10^{-4} is assumed, this estimation leads to a requirement of 184 GBTs for the MFT configuration with 5 planes. In case of noisy pixels rate reduction to 10^{-5} (as it has been assumed in the CDR of the ITS project of ALICE), the number of GBTs could be decreased to 150. In the event of the addition of a 6th plane to the setup, an increase of about 20% in the number of GBTs is foreseen.

3.3 General Layout

The mechanical and integration design of the MFT is constrained by requirements expressed by ALICE and the LHC, which are listed hereafter. In order to minimise the material thickness in the central rapidity region covered by the ITS and TPC among others, the services should be distributed as much as possible from the C-side, which means along the front absorber. The MFT, which will replace the FMD, must hold the beam pipe. Being located in a confined region, the MFT should not introduce thermal and mechanical perturbations to other surrounding detectors. The design of the

MFT should allow a removal for maintenance without moving the TPC. The time dedicated to this operation should be as low as possible, in order to be done during a LHC winter shutdown.

The MFT has a conical shape surrounding the beam pipe and is placed between the interaction point and the hadron absorber. A general view of a half of the MFT is shown in Figure 3.2. The MFT is divided into five disks of active area covering the acceptance in rapidity $-3.7 < \eta < -2.5$. The plane dimensions and locations are given in Table 2.1. The final geometry of the planes could still change due to integration constraints, mainly related to the beam pipe. The MFT collaboration is in contact with the ALICE technical coordination and the LHC vacuum group in order to optimise the geometry of the MFT for its physics program.

3.4 MFT Design

3.4.1 Global Design

The basic element of the MFT is the sensor. The CMOS pixel sensors described at the beginning of this chapter are assembled in a linear arrangement on flexible circuits to form ladders. The ladders are then assembled on supports and connected to boards located at the periphery in order to form half-disks. The five half-disks are installed into a half-cone made of carbon fibre (see Figure 3.2). Each half-cone is hermetically closed by kapton films around the structure to avoid heat dissipation to other detectors and a carbon fibre cover around the beam pipe support.

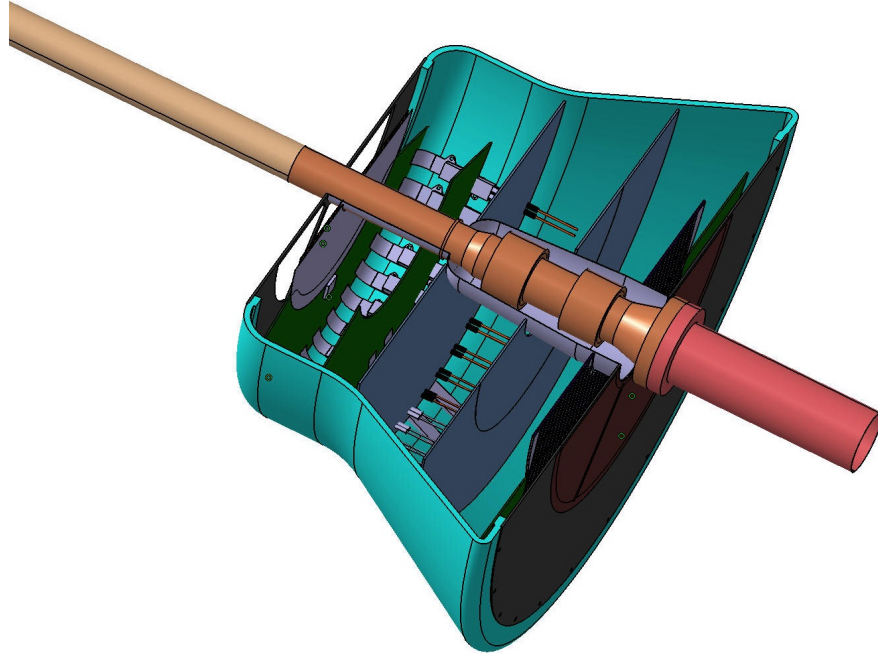


Figure 3.2: General view of one half of the Muon Forward Tracker.

3.4.2 Design of the Ladders

Even though the final sensor is not fully designed yet, some realistic characteristics of main building blocks have been taken into account as a starting point for the mechanical design of a ladder and for the cooling studies. The final size of the sensor is motivated by the readout time which fixed the number of rows and consequently the height of the sensor (i.e. 8 mm^2 in our case with 200 rows and including the digital part, in order to have a readout time within specifications $< 25 \mu\text{s}$) and the maximum width of the Tower Jazz reticule which is 30 mm, which corresponds to 1200 columns

with a pixel size of $25 \times 25 \mu\text{m}^2$. The usual way to integrate thinned pixels sensors on a support is to use flexible printed circuits which have a double function: mechanical support, signals transmission and power supplies distribution to all pixels sensors. To fulfil the function of powering and data transmission, the number of electrical lines has been evaluated. Per sensor, there are 6 lines for powering, 5 for data readout and temperature monitoring. In addition, 10 lines per ladder are used for JTAG configuration and clocks. These numbers imply that the flexible circuits should contain from 21 up to 76 electrical lines. In order to minimise their effective thickness, flexible circuits are made of 1 to 3 layers of 150 μm wide and 10 μm or 20 μm thick aluminium strips separated by 250 μm polyimide. In addition, the width of one ladder is 9.27 mm and there is 0.1 mm of interspace between two adjacent ladders. Consequently, one ladder maximally corresponds to an average thickness of 0.141% of X_0 (see Table 3.1).

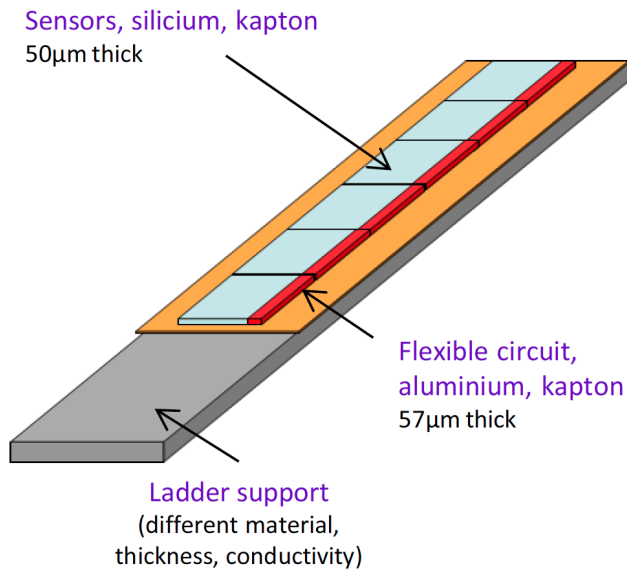


Figure 3.3: Schematics of a ladder.

3.4.3 Design of a Half Disk

The ladders are glued onto a support (the appropriate raw material is under study). The requirements concern its rigidity, its effective material thickness, but also its capability to drain the heat produced by the sensors. For the time being, materials like beryllium and carbon fibre are under consideration; they both have interesting stiffness and radiation-length properties. Table 3.2 reports the effective thickness of disks for the two considered materials; in both cases it is close to the requirement (0.4% of X_0) with a relative uncertainty of about 10% on the thickness of materials. The capability of these materials to extract heat is studied in Section 3.5.

The orientation of the ladders has been chosen to be perpendicular to the half cone structure inner border (Figure 3.4). The reasons are threefold: (i) the number of sensors per ladder is minimised; (ii) the number of ladder types is minimised; (iii) the connection to the read-out board is not in the areas of the cooling system inlet and outlet. In order to cover the full area, 586 ladders of 1 to 5 sensors with a total number of 2212 sensors are necessary (Tables 3.3 and 3.4). An overlap of 50 μm has been introduced for the alignment between sensors on opposite sides of a half-disk in order to minimise dead areas.

Two planes formed by one support and its ladders are assembled with an interspace of 2 mm and with the ladders on the outside located on a half-crown shaped PCB. The flexible cables are connected to this PCB, which is used as a read-out board. The purpose of this board is to concentrate

Layer	X_0 (mm)	Thickness (mm)	% of X_0	width (mm)	Norm. % of X_0
Sensor (Si)	93.3	0.050	0.0536	8	0.0458
Polyimide cover layer	281	0.012	0.0043	9.27	0.0042
Epoxy glue	456	0.012	0.0026	9.27	0.0026
Al (60% of flex surf.)	88.9	0.010	0.0068	9.27	0.0067
Polyimide substrate	281	0.025	0.0089	9.27	0.0088
Al (60% of flex surf.)	88.9	0.020	0.0135	9.27	0.0134
Polyimide substrate	281	0.025	0.0089	9.27	0.0088
Al (60% of flex surf.)	88.9	0.020	0.0135	9.27	0.0134
Polyimide substrate	281	0.025	0.0089	9.27	0.0088
Al (60% of flex surf.)	88.9	0.010	0.0068	9.27	0.0067
Epoxy glue	456	0.012	0.0026	9.27	0.0026
Polyimide cover layer	281	0.012	0.0043	9.27	0.0042
CMS components					0.0150
Total		0.233			0.141

Table 3.1: Estimate of the material thickness (expressed in units of radiation length) of a ladder (in case of 4 layers of strip lines). The thickness is averaged over the pitch of the ladders, which is 9.37 mm (9.27 mm of width plus 0.1 mm of interspace).

readout signals and to distribute power, triggers and configuration signals to the sensors. The GBT components used to communicate with the xTCA crate are located on these boards. Figure 3.4 shows the general structure of the half-disks.

Support Material	Layer	X_0 (mm)	Thickness	
			(mm)	(% of X_0)
Carbon	Flex + Sensor	165	0.23	0.141
	Support ($\times 2$)	312	0.40	0.128
	Flex + Sensor	165	0.23	0.141
			Total	0.410
Beryllium	Flex + Sensor	165	0.23	0.141
	Support ($\times 2$)	353	0.40	0.113
	Flex + Sensor	165	0.23	0.141
			Total	0.395

Table 3.2: Estimate of the material thickness (in units of radiation length) of one half-disk with two different materials for the ladder support.

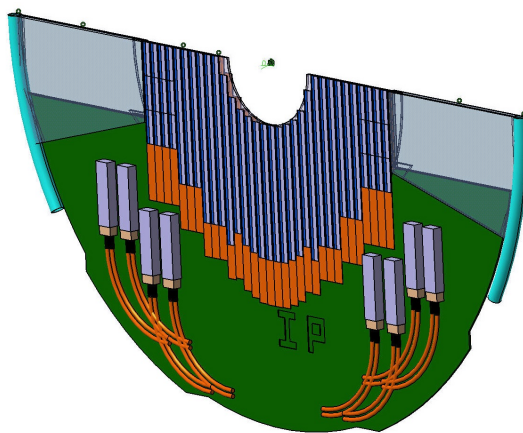


Figure 3.4: Example of the structure of a half disk (i.e. number 4). The green part is the read-out PCB; the optical links are also represented with their optical fibres. The IP label indicates the side facing the interaction point.

Nb of Sensors per ladder	Nb of ladders	Nb of wires	Nb of cable layers
1	8	21	1
2	48	32	2
3	108	43	2
4	326	54	2
5	96	64	3
Total	586		

Table 3.3: Estimate of the number of ladder types, and related number of wire layers.

Disk	Silicon Area (cm ²)	Nb of Sensors	Heat production (W)	Current (A)
0	364.9	318	159	88.3
1	460.1	386	193	107.2
2	520.3	454	227	126.1
3	584.7	502	251	139.4
4	669.8	552	276	153.3
Total	2599.8	2212	1106	614.4

Table 3.4: Estimate of the power consumption of the MFT sensors.

Disk	Nb of GBT	Heat production (W)	Current (A)
0	30	75	23
1	34	85	26
2	36	90	27
3	40	100	30
4	44	110	33
Total	184	460	139

Table 3.5: Estimate of the power consumption of the GBTs.

3.5 MFT Cooling

3.5.1 Cooling System

3.5.1.1 Power Dissipation

Several components of the MFT will produce some heat that requires to be extracted in order to avoid any damage to the sensors and any thermal disturbance to the surrounding detectors (namely ITS, TPC, VZERO and T0). The sources of heat are the sensors and the read-out electronics. Tables 3.4 and 3.5 report an estimate of the heat dissipated by the sensors and the GBTs. Assuming that 0.5 W is dissipated by each sensor, the detection part of the MFT is dissipating in total 1.1 kW, to which the power consumption of the read-out electronics must be added. It is evaluated to about 460 W, mainly coming from the GBT chip (2.5 W per chip). The total heat to extract would be about 1.7 kW, taking into account a safety margin of about 10 %.

3.5.1.2 Cooling System Design

Several options have been studied for the MFT cooling system and their thermal efficiency has been simulated. Two kinds of support have been considered and confronted on the basis of their effective thickness (in terms of radiation length) and their thermal properties. The first solution consists in a plain support made out of a low density material; the second solution is a set of two planes of smaller thickness and greater density separated by a small gap. The evaluated cooling processes are either by convection, blowing directly over the sensors, or by conduction by the means of cooling the support outside the detection acceptance, or by both processes (see Figure 3.5).

The solution using a plain disk has been finally excluded, because the low thermal conductivity of materials with large radiation length results in an inefficient evacuation of the heat produced by the pixel sensors. On the contrary, the solution using two planes allows air circulation within the gap. This additional air flow increases the heat extraction with a lower total material budget. It is worthwhile to notice that thin layers cannot extract much heat by conduction even with high heat conductivity. Therefore, it would be useless to design an additional cooling system on the outer side of the support. The second consequence is that it is not necessary to use materials with very high heat conductivity.

According to the pre-design studies, the solution proposed as a reference for the MFT cooling is the following: A disk is composed of two thin planes (0.2 mm thick). The sensors are cooled down by convection by means of three air flows, one between the two planes and the two others over the sensors. Air has been chosen as cooling fluid to simplify as much as possible the distribution of services, and this seems to be good enough to maintain the sensors at an acceptable operating temperature of about 35°C.

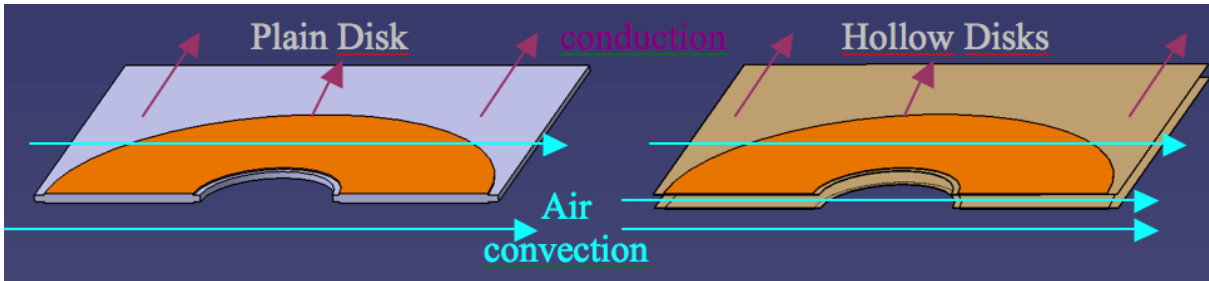


Figure 3.5: Two models used to study the cooling performances. On the left side, the plain disk version and, on the right, the two planes separated by an air gap.

3.5.2 Cooling Simulations

A first simulation taking into account the full geometry of the MFT has been performed to estimate the heat transfer coefficients (HTC). The input parameters were an air flow of 3000 l/min (velocity of about 10 m.s^{-1}) and an inlet temperature of 15°C . The mean HTC were $50 \text{ W}\cdot\text{m}^{-2}\cdot\text{K}^{-1}$ over the disks and $30 \text{ W}\cdot\text{m}^{-2}\cdot\text{K}^{-1}$ within. Those results were used to perform the thermal simulations of disks. In a near future, the new simulations will include some stiffeners between the planes which will be used also as channelling fins.

Another thermal simulation of one fourth of a half-disk with more conservative input parameters has been performed, because the environment of the simulated object is not completely defined yet. For example, the PCB and its electronics, which will also produce heat and introduce air flow disturbance, are not included. For this simulation, the ladders have been modelled by finite elements as precisely as possible taking into accounts the supports, the sensors and the flexible cables. The input parameters of this simulation were an inlet temperature of 22°C , heat transfer coefficients of $40 \text{ W}\cdot\text{m}^{-2}\cdot\text{K}^{-1}$ and $25 \text{ W}\cdot\text{m}^{-2}\cdot\text{K}^{-1}$ along the planes and between planes respectively.

This model allows evaluating the quality of the cooling for a large number of sensors assembled on a half-disk. The simulation shows that these conditions lead to a maximum temperature of the sensors of 30°C (see Figure 3.6). Further simulations with the final geometries of other disks and then the whole MFT are foreseen as the next steps.

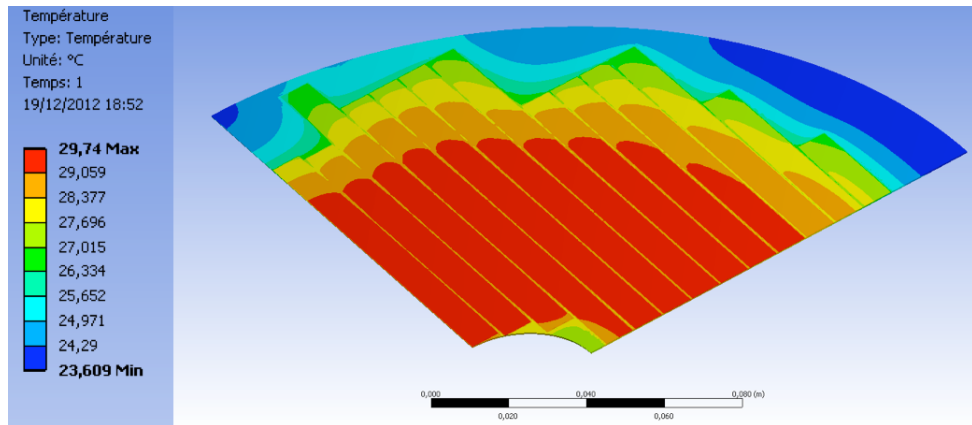


Figure 3.6: Simulation of the cooling of a plane with 0.2 mm thick beryllium support.

These first simulations allow us to define a possible and realistic cooling of the MFT sensors. The proposed solution is to use only dry air flow at 22°C and therefore simplify the design and services for this detector. Moreover, the use of quite thin supports (beryllium planes 0.2 mm thick) allows reaching the required effective thickness (see Table 3.2).

The next step of these simulations is to add the read-out electronics, which is located closed to the ladders. This electronics will be cooled by the same air flow, but the constraints on thickness and maximally allowed temperature are less stringent. At the level of the sensors the air flow could introduce vibrations, which could worsen the spatial resolution of the MFT – this will be studied further.

A mock-up of a half-plane is planned to be built in order to validate the design of the cooling and the mechanical structure.

3.6 Assembly Procedure

A precise study of the assembly procedure of the MFT has not been performed yet. In this paragraph the envisaged assembly procedure is reported based on our previous experience on silicon detectors, namely on the ALICE ITS (SSD and SDD) and the STAR SSD. Also contacts with people from the STAR HFT, which shares the same kind of problems, have been established.

During the production, some basic rules have to be followed. At each step of the production, a specific database for the construction is filled in order to store information relevant to the mounting and the corrections of the MFT data (alignment, noisy channels, etc.). From the chip production to the mounting of the full half MFT, the different steps are the following.

The CMOS pixel sensors corresponding to the validated design are tested and qualified with a probe station. After validation, a serial number is given; it could ideally be electrically coded in the chip, if the technology allows it. This serial number could then be readout through the data acquisition system. Based on the test results stored in the construction database, the chips are selected and assembled on a dedicated bench. The chips are positioned and glued on a flexible circuit and placed on a temporary stiffener for bonding. The different chips of one ladder are wire bonded and then tested again for validation. Still using the database, the ladders are selected before the disk assembly. They are removed from their temporary support and positioned with the help of a 3-D machine and glued onto the support corresponding to one fourth of a disk. The two parts of one half-disk are assembled with the read-out boards and the other mechanical pieces. The half-disk is tested for validation with the full data acquisition chain, which will require another test bench. When all half-disks corresponding to one half-MFT are produced, they are assembled in one MFT half-cone support; their positions are carefully measured and the results are stored in the database in order to have a starting point for the alignment procedure.

The assembly of the MFT requires the design of different tools and test benches, such as: a construction database, assembly benches, positioning tools, and test benches for the CMOS sensors qualification, the ladders, the quarter-disks and the half-disks. A common effort with the ITS collaboration would be profitable for the design of tools, use of a specific production facility or assembly machine and test benches, even if the final geometry of the detectors are different. The synopsis of the mounting and testing is represented in Figure 3.7.

3.7 Integrations Aspects

3.7.1 The Services

The distribution of services is constrained by their effective thickness and the available space to bring them to the MFT. The required services are threefold: electrical power for the sensors and the front end electronics, the optical fibres for the slow control and data transfer to DAQ and finally the air flow for the cooling.

3.7.1.1 Power Distribution

The large current needed to power the MFT requires a large cross section of copper. Due to the small radiation length of copper, the cabling cannot pass via the central rapidity region of the experiment, but has to be brought from the C-side along the hadronic absorber.

According to Tables 3.4 and 3.5, the amount of current is 615 A for the 1.8 V power supply and 139 A for the 3.3 V one. The quantity of cables has been evaluated [91]. It represents a total of copper cross section of 41.7 cm^2 at maximum and requires 3 trays along the hadron absorber.

The other issue to solve concerning the power distribution is the connection of the power lines to

MFT assembly scenario

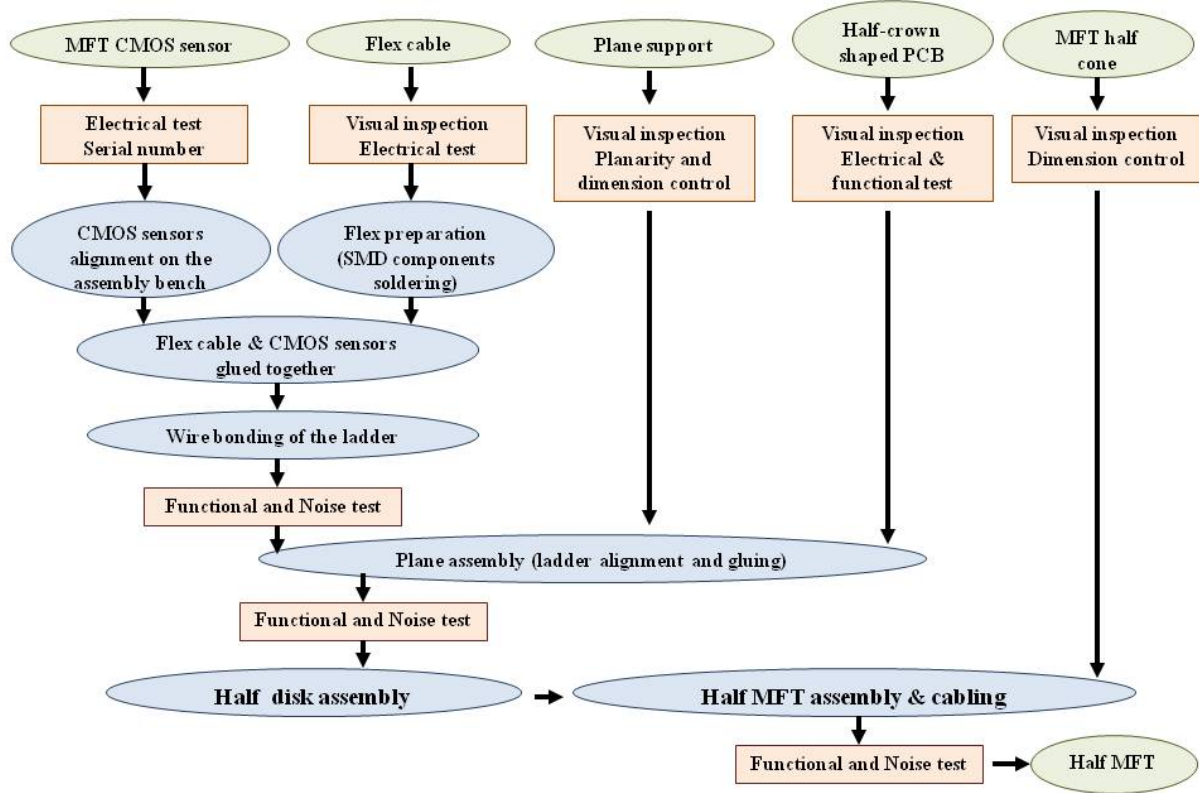


Figure 3.7: Synoptic of the mounting and the testing procedure proposed for the MFT.

the MFT. The detector needs to be extracted from the A-side in a short period corresponding to the winter shutdown of the LHC. Therefore one possibility for this connection is to use ZIF (Zero Insertion Force) connectors such as those from Samtec [94]. The calculation of the number of 20 pins connector gives 28 connectors for the power supply voltages (1.8 V and 3.3 V) and 28 connectors for the ground. Those connectors will be located at the rear end plate of the MFT cone and will be pressed with a pressure of 125 kg against a printed circuit board distributing the power [91].

3.7.1.2 Distribution of the Optical Fibres

For the slow control of the CMOS sensors and the data transfer to the DAQ, the MFT requires 184 optical fibres (one per GBT link). Their effective thickness is small enough so that they can pass through the central rapidity region (between the ITS and the TPC). The GBTs and their optical converters are located on the PCBs of the discs (see Figure 3.4). The optical fibres go towards the back of the MFT along the carbon fibre main structure. Then they are bent in order to pass along the insertion cage of the MFT towards the A-side. The optical fibres are represented in orange in Figure 3.8.

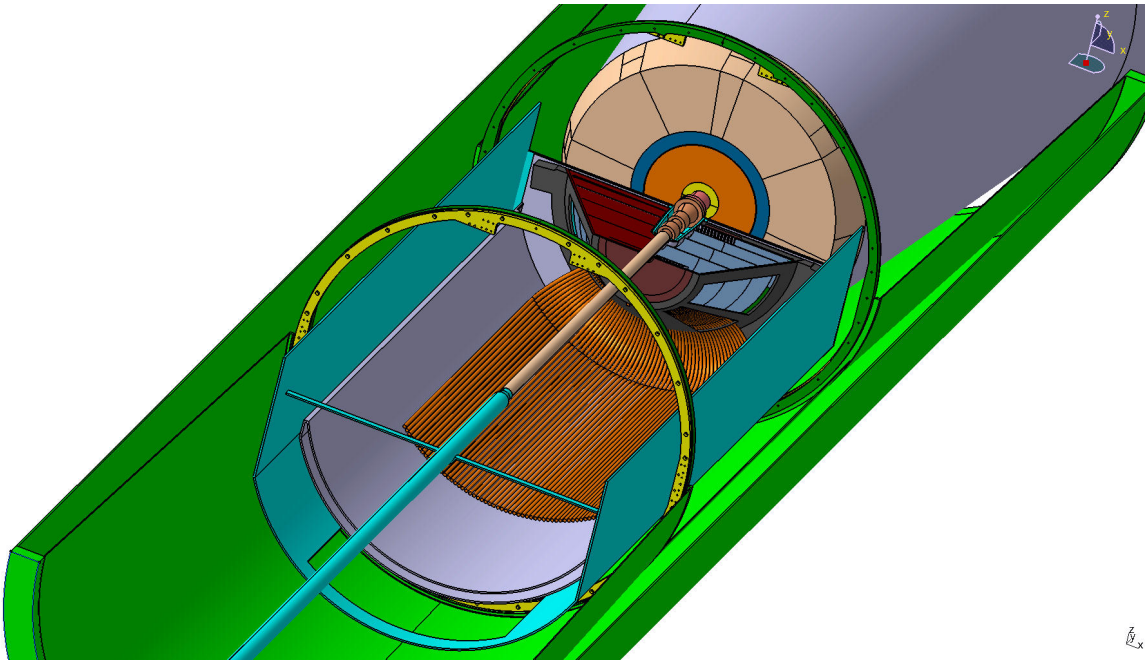


Figure 3.8: Half MFT and its frame in their nominal position. The optical fibres are represented in orange (they are not represented in their full length to see the structure).

3.7.1.3 Distribution of the Air Cooling

The idea is to use the hollow part of the support cage and to connect it to the distribution system inside the MFT cone. That implies to create some tubing made of carbon fibre in the insertion cage for the ingoing and outgoing flows. The temperature of the ingoing air could be either at 15°C or at room temperature (about 22°C). As seen in Section 3.5.2, the current simulation are done with an air flow of 3000 l/min. Final simulations and bench tests with the full heat production and final geometry will be necessary to fix the inlet air temperature and the air flow.

3.7.2 The Mechanical Supports

This section describes the different mechanical structures that are planned to hold the MFT and the beam-pipe (one of the functionality that the MFT must fulfil). Those structures have been designed in close collaboration with the ALICE Technical Coordination and the LHC vacuum groups.

3.7.2.1 The Support Cage

At the location of the MFT, the beam pipe should be held permanently even during installation and maintenance of the MFT. The solution is represented in Figure 3.9. At the back of the cage designed to act as a support of the inner detectors (new ITS and MFT), a plate is added and a cylinder, surrounding the bellows, to hold the beam pipe at the junction between the beryllium and the aluminum parts. Some clearance is required to allow the deformation of the bellows due to the displacement of the hadron absorber when the solenoid is turned on and also during the transfer of the support cage from the insertion rails to the TPC cage. The clearance values are reported in Table 3.6 and concern the planes 2 to 4 only (planes 0 and 1 are located around the beryllium part of the tube). These values would modify the geometry of the MFT planes (internal radii and locations along the beam direction). In addition, a bake-out system is planned to be used at the level of the bellows. For geometrical acceptance reasons, this system should be removable, which implies to

possibly modify the support of the beam pipe. Solutions have been proposed and discussions with the LHC vacuum group and the ALICE technical coordination are underway.

Location	Clearance (mm)
Front of first bellows	4
Rear of first bellows	10
Front of second bellows	10
Rear of second bellows	10

Table 3.6: Clearance constraints around the beam pipe. The value of 10 mm at the rear of the second bellows is due to the front absorber displacement.

The cables used to power the MFT will be connected on the back plane of the support cage to a copper plate, on which the ZIF connectors of the MFT cone are maintained in contact. These cables should be flexible enough not to add constraints on the support cage in situations, where the hadronic absorber moves, when the magnetic fields of the solenoid and the dipole are switched on.

3.7.2.2 The Insertion Cage

The two halves of the MFT cone are fixed on two specific half cages in order to be inserted, positioned and fixed to the support cage. One half of the insertion cage can be seen in Figure 3.10. The half cages are inserted from the A-side and positioned by the mean of wheels sliding on guides which are part of the support cage.

The other functionality of this insertion cage is to bring the remaining services (air flow and optical fibres) to the MFT. As discussed above, these services will be located in between the two shells of each insertion half-cages. The available space is about 3 cm at an angle of approximatively 45° (see Figure 3.8).

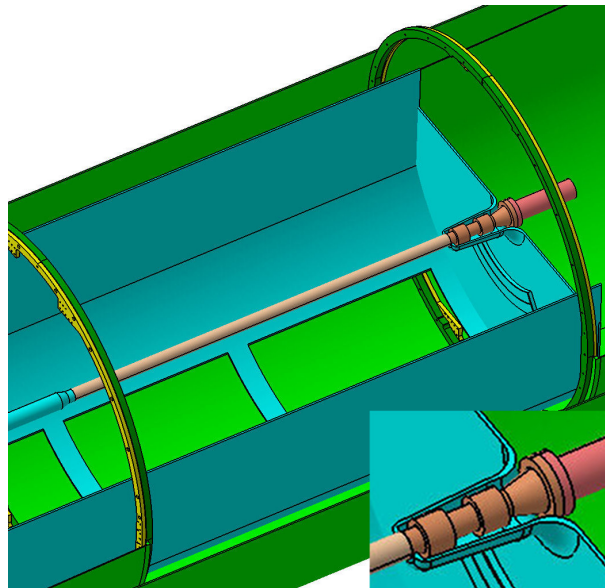


Figure 3.9: Support cage in position once fixed to the TPC cage. The bottom left picture is an enlarged view of the cylinder designed to hold the beam pipe on the C-side.

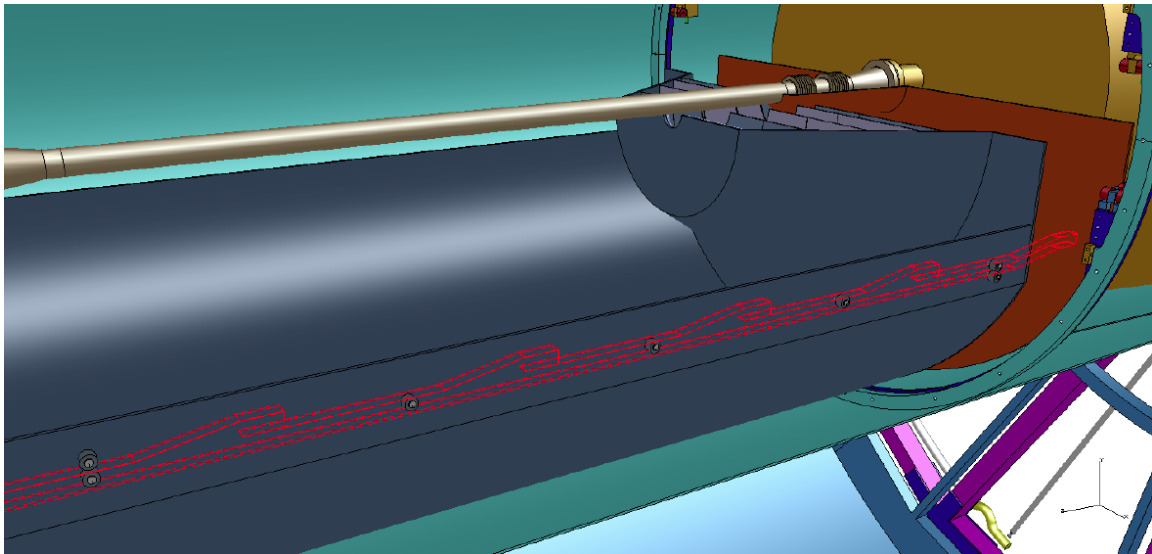


Figure 3.10: Insertion guides (represented in red) used to position the MFT in its nominal location. Those guides are part of the support cage.

3.7.3 Integration Constraints from Other Forward Detectors

In this section the constraints from existing forward detectors (T0, VZERO, and FMD) are investigated.

Signals from the T0 detector are used as a reference time for the TOF measurement and to create the L0 trigger. The T0 generates signals with a time resolution of 50 ps. Its efficiency is high for central heavy-ion collisions, but smaller for pp or peripheral collisions. The detector uses a quartz radiator and photomultipliers. The VZERO provides trigger information for minimum bias collisions in pp and Pb–Pb, gives information on collision centrality and participates in the rejection of beam–gas interactions. The VZERO detector is made of two scintillator arrays. The FMD contributes to the determination of the reaction plane of the collision and to multiplicity measurements.

The installation of the MFT requires to remove the FMD. The measurements done by the FMD, i.e. charged particle multiplicity measurement and reaction plane determination, would be possible with the new MFT. Therefore, the physics capabilities of the ALICE experiment concerning those topics will be kept and possibly even enhanced by the presence of the MFT. Specific simulation studies should be performed in order to fully characterize the MFT capabilities on these topics.

The current VZERO will not be able to handle the high luminosity of the LHC foreseen after the Long Shutdown 2. The plan of the ALICE collaboration is to develop a single detector replacing the current VZERO and T0 detectors. It should provide the capabilities of these two detectors, namely a highly efficient minimum bias trigger, precise collision time measurement, centrality trigger and estimator, event plane measurement, and luminosity monitor. The foreseen detector will use the technology of the actual T0 detector (quartz radiator) together with MCP-PMT detectors [95]. The relevant parameter concerning the MFT integration is the thickness of this new detector along the beam axis and its location in the z direction. The foreseen scenario is to have a 20 mm thick quartz radiator in front of XP85012 MCP-PMT from Hamamatsu, which in turn have a thickness of about 30 mm. Therefore the new T0 detector would have a total thickness of about 50 mm, which can easily be fitted in the space between the MFT box and the front of the absorber.

3.8 Alignment Strategy

The alignment strategy for the MFT is divided into two parts: the survey measurements and the reconstruction of straight tracks once in nominal position within ALICE, with magnets switched off. The MFT is made of hundreds of separate ladders equipped with CMOS sensors, whose position is different from the ideal one due to diverse limitations associated with the mechanical and assembly tolerances, and integration of the different components to form the planes. In order to achieve the required high precision on the track parameters, the relative position (location and orientation) of every sensor needs to be determined with high precision ($< 10 \mu\text{m}$ for the sensors).

The survey measurement strategy is divided into several steps. The first step of the alignment procedure uses the positioning survey measurements of each sensor during the sensors assembly on the flexible circuits to form a ladder (reference markers are engraved on the sensor surface). The relative position of each sensor of one ladder will be measured precisely and stored in a database. The ladder will be equipped with reference targets and the second step consists to align precisely the ladders on the half-disk. The third step consists to measure and align the position of the half-disk inside the MFT cage. As a half-MFT inside its cage can be assembled and prepared completely and independently in the laboratory, a global survey of the sphere of mirror targets can also be done within a local coordinate system before integration in ALICE, e.g. using a laser tracker (see Figure 3.11). The MFT cage can then be integrated inside the experiment, with the local coordinate frame transposed into cavern to make links with the global coordinate system of ALICE.

All the measurements of misalignment obtained during the construction and installation of the MFT will be used as a starting point to determine the precise position and orientation of the sensors. The final alignment will be performed by using particle tracking. While it is possible in principle, a first alignment using cosmic muons might not be useful for two reasons: first, because the half-cones should be put vertically in order to optimise the rate, which could be of the order of few hundredth of Hertz; second, this set-up would correspond to different temperature conditions than the ones expected during the data taking, because of the low acquisition rate and the vertical orientation of the half cones. The final, precise alignment of the MFT will then be performed by means of straight track measurements coming from beam-beam collisions: for this purpose, ALICE would request a dedicated fill of the LHC with the solenoid and the dipole magnets switched off. The necessary amount of data to achieve the $\lesssim 10 \mu\text{m}$ precision has not been evaluated yet.

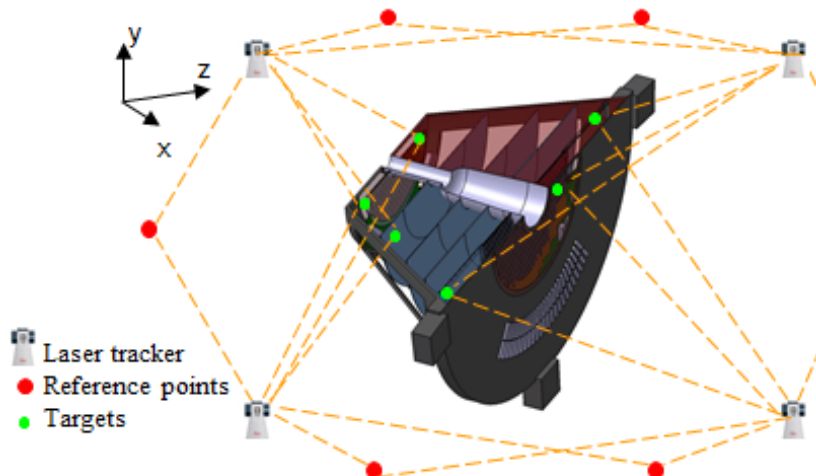


Figure 3.11: Survey measurements of a half-MFT (only few targets are represented for illustration).

Chapter 4

Project Organisation

The MFT is a device to be installed in the acceptance of the current ALICE Muon Spectrometer – in fact the MFT operation relies on an operational Muon Spectrometer. Consequently, upgrading of the full system dedicated to the muon physics in ALICE will include two operations: the construction and installation of the MFT and the upgrade of the present front-end readout electronics of the Muon Spectrometer (tracking and trigger). The spectrometer upgrade strategy is described in the Letter of Intent for the upgrade of the ALICE experiment [1]. The MFT project is strongly supported by the ALICE Muon collaboration.

4.1 Project Management

Figure 4.1 represents the proposed organisation of the MFT project, which will be led by the MFT Institutional Board composed by the group leaders of the participating institutes.

The MFT project is managed by a project coordination team composed of a Project Coordinator and his deputy, and a Project Technical Coordinator, who are in charge of the coordination of the relevant physics studies and the technical activities of the project (from R&D phase up to the integration of the MFT inside ALICE). Contributions and responsibilities of the participating institutes are being discussed according to their competence, experience and manpower. The funding resources are discussed and will be established with the funding agencies in parallel with discussions in the approval process of the project.

The technology chosen for the MFT, CMOS Monolithic Active Pixel Sensors, is the same as for the new ALICE ITS detector. Therefore, the R&D studies related to the pixel sensor and its assembly techniques as well as to data transmission are performed in a joint effort by the two projects. In addition, the physics case of the MFT is directly linked to the one of the current Muon Spectrometer, as presented in this document. As a consequence, the eight Working Groups into which the MFT project will be divided, will work in close collaboration with the corresponding working groups of either the ITS or MUON projects (see Figure 4.1). In particular, the physics simulation working group (WG1) is a common working group with the Muon Spectrometer project, while both WG2 and WG8 are in common with the ITS project. The other working groups will work in synergy with the Muon Spectrometer and ITS projects.

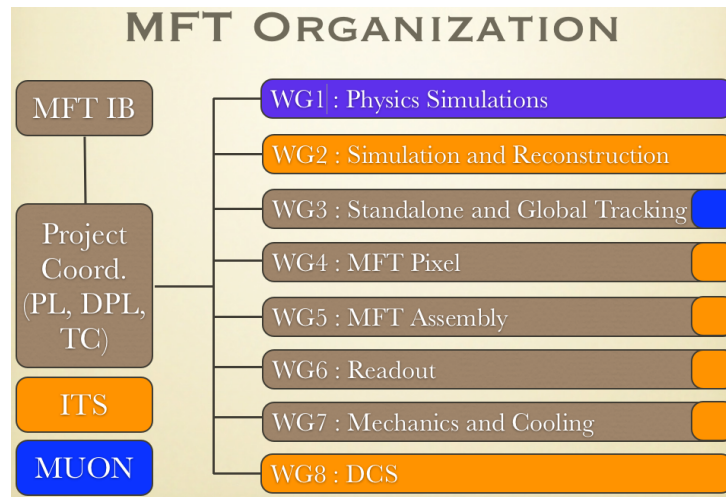


Figure 4.1: Schematics of the proposed MFT organisation. The colour code of the working groups shows the WG in common (fully coloured) or in synergy (partly coloured) with the corresponding working groups of MUON (blue) or ITS (orange) projects.

4.2 Participating Institutes

Each institute has specific expertise thanks to their previous contributions to similar activities related to detector construction. The list of the already involved institutes is given in Table 4.1. Others institutes have expressed their interest in participating in the MFT project. Thanks to the important synergies between the MFT project and the MUON and ITS projects, laboratories are involved indirectly to the MFT project. These laboratories are listed as “contributing institutes” in Table 4.2.

The targeted installation window of the MFT is the LHC Long Shutdown 2, which is currently sched-

Table 4.1: List of institutes participating to the MFT project.

COUNTRY	CITY	LABORATORY
Collaborating Institutes		
France	Clermont-Ferrand	LPC
	Lyon	IPN
	Nantes	SUBATECH
	Saclay	IRFU
India	Calcutta	SINP
	Aligarh	AMU
Russia	Gatchina	PNPI
Interested Institutes		
South Africa	Cape Town	UCT
	Cape Town	iThemba
Russia	Dubna	JINR
Armenia	Yerevan	ANSL

Table 4.2: List of institutes involved in the MUON or ITS projects in synergy with the MFT project.

Contributing Institutes (via ITS/MFT synergy)			
COUNTRY	CITY	LAB.	DOMAIN
France	Orsay	IPN	Physics and heat extraction studies
	Strasbourg	IPHC	Sensor simulation and reconstruction
Italy	Cagliari	INFN	Physics and standalone tracking
	Torino	INFN	Physics and Sensor simulation and reconstruction
XXX	To be determined	XXX	Common assembly site of ITS and MFT

Table 4.3: MFT project timeline.

Year	Activity
2013 – 2014	R&D
2013	Prototypes of the sensor Selection of CMOS architecture First flex cable prototype Engineering design for mechanics, cooling and services
2014	Full scale CMOS prototype Final flex prototype MFT plane demonstrator
2015 – 2018	Construction and Installation
2015 – 2016	Preproduction of CMOS sensors CMOS series production CMOS qualifications tests Flex cable series production
2017	Ladders assembly and pre-commissioning Full MFT assembly
2018	Installation in the cavern

uled for 2018. A rough time schedule of the project, with activities for main components and main milestones, is given by Table 4.3.

4.3 Cost Estimate

As the MFT project is in a very early stage, only preliminary cost estimates can be given, which are largely based on previous experience. Uncertainties are in particular related to the future choice of the technology for the CMOS sensors.

The cost of R&D is estimated to 0.95 MCHF.

The production cost is estimated for two options with respect to the assembly technique and qualification tests of the CMOS sensors:

Table 4.4: Estimate of the production cost for the ALICE-MFT. See text for detail of two options (a) and (b).

Item	Cost (MCHF)
CMOS	0.65
Thinning, dicing and mounting	$0.43^{(b)} - 1.27^{(a)}$
MCM	0.33
Flex cables, FEE	0.49
Cables, connectors	0.49
Mechanics, cooling	0.52
Low voltage regulation	0.15
Power supply	0.25
Total	$3.31^{(b)} - 4.15^{(a)}$

- (a) The more expensive option is based on using wire bonding technique and on subcontracting the CMOS qualification tests and their assembly on flexible circuits.
- (b) The less expansive option is based on the estimates made by the ITS upgrade project, including a laser flip-chip mounting technique [96], and CMOS qualification tests and their assembly on flexible circuits performed in laboratories.

Taking into account these two options, the production cost of the MFT is estimated to range from 3.31 MCHF to 4.15 MCHF. Table 4.4 lists the production cost breakdown.

Appendix A

The ALICE Collaboration

B. Abelev⁷³, J. Adam³⁷, D. Adamová⁸¹, A.M. Adare¹³¹, M.M. Aggarwal⁸⁵, G. Aglieri Rinella³⁴, M. Agnello^{91,108}, A.G. Agocs¹³⁰, A. Agostinelli²⁶, Z. Ahammed¹²⁶, N. Ahmad¹⁷, A. Ahmad Masoodi¹⁷, I. Ahmed¹⁵, S.U. Ahn⁶⁶, S.A. Ahn⁶⁶, I. Aimo^{108,91}, S. Aiola¹³¹, M. Ajaz¹⁵, A. Akindinov⁵⁶, D. Aleksandrov⁹⁷, B. Alessandro¹⁰⁸, D. Alexandre⁹⁹, A. Alici^{12,102}, A. Alkin³, J. Alme³⁵, T. Alt³⁹, V. Altini³¹, S. Altinpinar¹⁸, I. Altsybeev¹²⁵, C. Alves Garcia Prado¹¹⁵, C. Andrei⁷⁶, A. Andronic⁹⁴, V. Anguelov⁹⁰, J. Anielski⁵¹, T. Antičić⁹⁵, F. Antinori¹⁰⁵, P. Antonioli¹⁰², L. Aphecetche¹⁰⁹, H. Appelshäuser⁴⁹, N. Arbor⁶⁹, S. Arcelli²⁶, N. Armesto¹⁶, R. Arnaldi¹⁰⁸, T. Aronsson¹³¹, I.C. Arsene⁹⁴, M. Arslanbekov⁴⁹, A. Augustinus³⁴, R. Averbeck⁹⁴, T.C. Awes⁸², M.D. Azmi^{87,17}, M. Bach³⁹, A. Badalà¹⁰⁴, Y.W. Baek^{40,68}, S. Bagnasco¹⁰⁸, R. Bailhache⁴⁹, V. Bairathi⁸⁹, R. Bala⁸⁸, A. Baldissari¹⁴, F. Baltasar Dos Santos Pedrosa³⁴, J. Bán⁵⁷, R.C. Baral⁵⁹, R. Barbera²⁷, F. Barile³¹, G.G. Barnaföldi¹³⁰, L.S. Barnby⁹⁹, V. Barret⁶⁸, J. Bartke¹¹², M. Basile²⁶, N. Bastid⁶⁸, S. Basu¹²⁶, B. Bathan⁵¹, G. Batigne¹⁰⁹, B. Batyunya⁶⁴, P.C. Batzing²¹, C. Baumann⁴⁹, I.G. Bearden⁷⁸, H. Beck⁴⁹, N.K. Behera⁴⁴, I. Belikov⁵², F. Bellini²⁶, R. Bellwied¹¹⁷, E. Belmont-Moreno⁶², G. Bencedi¹³⁰, S. Beole²⁵, I. Berceanu⁷⁶, A. Bercuci⁷⁶, Y. Berdnikov⁸³, D. Berenji¹³⁰, A.A.E. Bergognon¹⁰⁹, R.A. Bertens⁵⁵, D. Berzana²⁵, L. Betev³⁴, A. Bhasin⁸⁸, A.K. Bhati⁸⁵, B. Bhattacharjee⁴¹, J. Bhom¹²², L. Bianchi²⁵, N. Bianchi⁷⁰, J. Bielčík³⁷, J. Bielčíková⁸¹, A. Bilandžić⁷⁸, S. Bjelogrlic⁵⁵, F. Blanco¹⁰, D. Blau⁹⁷, C. Blume⁴⁹, F. Bock^{72,90}, A. Bogdanov⁷⁴, H. Bøggild⁷⁸, M. Bogolyubsky⁵³, L. Boldizsár¹³⁰, M. Bombara³⁸, J. Book⁴⁹, H. Borel¹⁴, A. Borissov^{93,129}, J. Bornschein³⁹, F. Bossú⁶³, M. Botje⁷⁹, E. Botta²⁵, S. Böttger⁴⁸, S. Bouvier¹⁰⁹, P. Braun-Munzinger⁹⁴, M. Bregant^{115,109}, T. Breitner⁴⁸, T.A. Broker⁴⁹, T.A. Browning⁹², M. Broz³⁶, E. Bruna¹⁰⁸, G.E. Bruno³¹, D. Budnikov⁹⁶, H. Buesching⁴⁹, S. Bufalino¹⁰⁸, J.M. Buhour¹⁰⁹, P. Buncic³⁴, O. Busch⁹⁰, Z. Buthelezi⁶³, D. Caffarri²⁸, X. Cai⁷, H. Caines¹³¹, A. Caliva⁵⁵, E. Calvo Villar¹⁰⁰, P. Camerini²⁴, V. Canoa Roman³⁴, F. Carena³⁴, W. Carena³⁴, F. Carminati³⁴, A. Casanova Díaz⁷⁰, J. Castillo Castellanos¹⁴, E.A.R. Casula²³, V. Catanescu⁷⁶, C. Cavicchioli³⁴, C. Ceballos Sanchez⁹, J. Cepila³⁷, P. Cerello¹⁰⁸, B. Chang¹¹⁸, S. Chapelard³⁴, J.L. Charvet¹⁴, S. Chattopadhyay¹²⁶, S. Chattopadhyay⁹⁸, M. Cherney⁸⁴, C. Cheshkov¹²⁴, B. Cheynis¹²⁴, V. Chibante Barroso³⁴, D.D. Chinellato^{117,116}, P. Chochula³⁴, M. Chojnacki⁷⁸, S. Choudhury¹²⁶, P. Christakoglou⁷⁹, C.H. Christensen⁷⁸, P. Christiansen³², T. Chujo¹²², S.U. Chung⁹³, C. Cicalo¹⁰³, L. Cifarelli^{12,26}, F. Cindolo¹⁰², J. Cleymans⁸⁷, F. Colamaria³¹, D. Colella³¹, A. Collu²³, M. Colocci²⁶, G. Conesa Balbastre⁶⁹, Z. Conesa del Valle^{47,34}, M.E. Connors¹³¹, G. Contin²⁴, J.G. Contreras¹¹, T.M. Cormier^{82,129}, Y. Corrales Morales²⁵, P. Cortese³⁰, I. Cortés Maldonado², M.R. Cosentino^{72,115}, F. Costa³⁴, P. Crochet⁶⁸, R. Cruz Albino¹¹, E. Cuautle⁶¹, L. Cunqueiro^{70,34}, A. Dainese¹⁰⁵, R. Dang⁷, A. Danu⁶⁰, D. Das⁹⁸, I. Das⁴⁷, K. Das⁹⁸, S. Das⁴, A. Dash¹¹⁶, S. Dash⁴⁴, S. De¹²⁶, Y. Degerli¹⁴, H. Delagrange¹⁰⁹, A. Deloff⁷⁵, E. Dénes¹³⁰, G. D'Erasmo³¹, G.O.V. de Barros¹¹⁵, A. De Caro^{12,29}, G. de Cataldo¹⁰¹, J. de Cuveland³⁹, A. De Falco²³, D. De Gruttola^{29,12}, N. De Marco¹⁰⁸,

S. De Pasquale²⁹, R. de Rooij⁵⁵, M.A. Diaz Corchero¹⁰, T. Dietel^{51,87}, R. Divià³⁴, D. Di Bari³¹, S. Di Liberto¹⁰⁶, A. Di Mauro³⁴, P. Di Nezza⁷⁰, Ø. Djupsland¹⁸, A. Dobrin^{55,129}, T. Dobrowolski⁷⁵, D. Domenicis Gimenez¹¹⁵, B. Dönigus⁴⁹, O. Dordic²¹, A.K. Dubey¹²⁶, A. Dubla⁵⁵, L. Ducroux¹²⁴, P. Dupieux⁶⁸, A.K. Dutta Majumdar⁹⁸, D. Elia¹⁰¹, H. Engel⁴⁸, B. Erazmus^{34,109}, H.A. Erdal³⁵, D. Eschweiler³⁹, B. Espagnon⁴⁷, M. Estienne¹⁰⁹, S. Esumi¹²², D. Evans⁹⁹, S. Evdokimov⁵³, G. Eyyubova²¹, D. Fabris¹⁰⁵, J. Faivre⁶⁹, D. Falchieri²⁶, A. Fantoni⁷⁰, M. Fasel⁹⁰, D. Fehlker¹⁸, L. Feldkamp⁵¹, D. Felea⁶⁰, A. Feliciello¹⁰⁸, G. Feofilov¹²⁵, J. Ferencei⁸¹, A. Fernández Téllez², E.G. Ferreiro¹⁶, A. Ferretti²⁵, A. Festanti²⁸, J. Figiel¹¹², M.A.S. Figueiredo^{115,119}, S. Filchagin⁹⁶, D. Finogeev⁵⁴, F.M. Fionda³¹, E.M. Fiore³¹, E. Floratos⁸⁶, M. Floris³⁴, C. Flouzat¹⁴, S. Foertsch⁶³, P. Foka⁹⁴, S. Fokin⁹⁷, E. Fragiacomo¹⁰⁷, A. Francescon^{28,34}, U. Frankenfeld⁹⁴, U. Fuchs³⁴, C. Furget⁶⁹, M. Fusco Girard²⁹, J.J. Gaardhøje⁷⁸, M. Gagliardi²⁵, M. Gallio²⁵, D.R. Gangadharan^{19,72}, P. Ganoti^{82,86}, C. Garabatos⁹⁴, E. Garcia-Solis¹³, C. Gargiulo³⁴, I. Garishvili⁷³, J. Gerhard³⁹, M. Germain¹⁰⁹, A. Gheata³⁴, M. Gheata^{60,34}, B. Ghidini³¹, P. Ghosh¹²⁶, S.K. Ghosh⁴, P. Gianotti⁷⁰, P. Giubellino³⁴, E. Gladysz-Dziadus¹¹², P. Glässel⁹⁰, R. Gomez^{114,11}, P. González-Zamora¹⁰, S. Gorbunov³⁹, L. Görlich¹¹², S. Gotovac¹¹¹, L.K. Graczykowski¹²⁸, R. Grajcarek⁹⁰, A. Grelli⁵⁵, A. Grigoras³⁴, C. Grigoras³⁴, V. Grigoriev⁷⁴, A. Grigoryan¹, S. Grigoryan⁶⁴, B. Grinyov³, N. Grion¹⁰⁷, J.F. Grosse-Oetringhaus³⁴, J.-Y. Grossiord¹²⁴, R. Grossos³⁴, F. Guber⁵⁴, C. Guérin¹²⁴, R. Guernane⁶⁹, B. Guerzoni²⁶, M. Guilbaud¹²⁴, F. Guilloux¹⁴, G. Guilloux¹⁰⁹, K. Gulbrandsen⁷⁸, H. Gulkanyan¹, T. Gunji¹²¹, A. Gupta⁸⁸, R. Gupta⁸⁸, K. H. Khan¹⁵, R. Haake⁵¹, Ø. Haaland¹⁸, C. Hadjidakis⁴⁷, M. Haiduc⁶⁰, H. Hamagaki¹²¹, G. Hamar¹³⁰, L.D. Hanratty⁹⁹, A. Hansen⁷⁸, J.W. Harris¹³¹, H. Hartmann³⁹, A. Harton¹³, D. Hatzifotiadou¹⁰², S. Hayashi¹²¹, A. Hayrapetyan^{34,1}, S.T. Heckel⁴⁹, M. Heide⁵¹, H. Helstrup³⁵, A. Hergelegiu⁷⁶, G. Herrera Corral¹¹, B.A. Hess³³, K.F. Hetland³⁵, B. Hicks¹³¹, B. Hippolyte⁵², J. Hladky⁵⁸, Y. Hori¹²¹, P. Hristov³⁴, M. Huang¹⁸, T.J. Humanic¹⁹, D. Hutter³⁹, D.S. Hwang²⁰, J.C. Ianigro¹²⁴, R. Ilkaev⁹⁶, I. Ilkiv⁷⁵, M. Inaba¹²², E. Incani²³, G.M. Innocenti²⁵, C. Insa⁶⁸, C. Ionita³⁴, M. Ippolitov⁹⁷, M. Irfan¹⁷, M. Ivanov⁹⁴, V. Ivanov⁸³, O. Ivanytskyi³, C. Jahnke¹¹⁵, H.J. Jang⁶⁶, M.A. Janik¹²⁸, P.H.S.Y. Jayarathna¹¹⁷, S. Jena^{44,117}, R.T. Jimenez Bustamante⁶¹, PG. Jones⁹⁹, H. Jung⁴⁰, A. Jusko⁹⁹, S. Kalcher³⁹, P. Kalinak⁵⁷, A. Kalweit³⁴, J. Kamin⁴⁹, J.H. Kang¹³², V. Kaplin⁷⁴, S. Kar¹²⁶, A. Karasu Uysal⁶⁷, O. Karavichev⁵⁴, T. Karavicheva⁵⁴, E. Karpechev⁵⁴, U. Kebschull⁴⁸, R. Keidel¹³³, M. Mohisin. Khan^{17,I}, P. Khan⁹⁸, S.A. Khan¹²⁶, A. Khanzadeev⁸³, Y. Kharlov⁵³, B. Kileng³⁵, B. Kim¹³², D.W. Kim^{66,40}, D.J. Kim¹¹⁸, J.S. Kim⁴⁰, M. Kim⁴⁰, M. Kim¹³², S. Kim²⁰, T. Kim¹³², S. Kirsch³⁹, I. Kisiel³⁹, S. Kiselev⁵⁶, A. Kisiel¹²⁸, G. Kiss¹³⁰, J.L. Klay⁶, J. Klein⁹⁰, C. Klein-Bösing⁵¹, A. Kluge³⁴, M.L. Knichel⁹⁴, A.G. Knospe¹¹³, C. Kobdaj^{34,110}, M.K. Köhler⁹⁴, T. Kollegger³⁹, A. Kolojvari¹²⁵, V. Kondratiev¹²⁵, N. Kondratyeva⁷⁴, A. Konevskikh⁵⁴, V. Kovalenko¹²⁵, M. Kowalski¹¹², S. Kox⁶⁹, G. Koyithatta Meethaleevedu⁴⁴, J. Kral¹¹⁸, I. Králik⁵⁷, F. Kramer⁴⁹, A. Kravčáková³⁸, M. Krelina³⁷, M. Kretz³⁹, M. Krivda^{57,99}, F. Krizek^{81,42}, M. Krus³⁷, E. Kryshen⁸³, M. Krzewicki⁹⁴, V. Kučera⁸¹, Y. Kucheriaev⁹⁷, T. Kugathasan³⁴, C. Kuhn⁵², PG. Kuijer⁷⁹, I. Kulakov⁴⁹, J. Kumar⁴⁴, P. Kurashvili⁷⁵, A. Kurepin⁵⁴, A.B. Kurepin⁵⁴, A. Kuryakin⁹⁶, S. Kushpil⁸¹, V. Kushpil⁸¹, M.J. Kweon^{46,90}, Y. Kwon¹³², P. Ladron de Guevara⁶¹, C. Lagana Fernandes¹¹⁵, I. Lakomov⁴⁷, R. Langoy¹²⁷, C. Lara⁴⁸, A. Lardeux¹⁰⁹, A. Lattuca²⁵, S.L. La Pointe^{55,108}, P. La Rocca²⁷, R. Lea²⁴, G.R. Lee⁹⁹, I. Legrand³⁴, J. Lehnert⁴⁹, R.C. Lemmon⁸⁰, M. Lenhardt⁹⁴, V. Lenti¹⁰¹, E. Leogrande⁵⁵, M. Leoncino²⁵, I. León Monzón¹¹⁴, P. Lévai¹³⁰, S. Li^{68,II,7}, J. Lien^{18,127}, R. Lietava⁹⁹, S. Lindal²¹, V. Lindenstruth³⁹, C. Lippmann⁹⁴, M.A. Lisa¹⁹, H.M. Ljunggren³², D.F. Lodato⁵⁵, P.I. Loenne¹⁸, V.R. Loggins¹²⁹, V. Loginov⁷⁴, D. Lohner⁹⁰, C. Loizides⁷², X. Lopez⁶⁸, E. López Torres⁹, X.-G. Lu⁹⁰, P. Luettig⁴⁹, M. Lunardon²⁸, J. Luo⁷, G. Luparello⁵⁵, C. Luzzi³⁴, A. M. Gago¹⁰⁰, P. M. Jacobs⁷², R. Ma¹³¹, A. Maevskaia⁵⁴, M. Mager³⁴, D.P. Mahapatra⁵⁹, A. Maire^{90,52}, M. Malaev⁸³, I. Maldonado Cervantes⁶¹, L. Malinina^{64,III}, D. Mal'Kevich⁵⁶, P. Malzacher⁹⁴, A. Mamonov⁹⁶, L. Manceau¹⁰⁸, V. Manko⁹⁷, F. Manso⁶⁸, V. Manzari^{101,34}, M. Marchisone^{68,25}, J. Mareš⁵⁸, G.V. Margagliotti²⁴, A. Margotti¹⁰², A. Marín⁹⁴, C. Markert^{34,113}, M. Marquard⁴⁹, I. Martashvili¹²⁰, N.A. Martin⁹⁴, P. Martinengo³⁴, M.I. Martínez²,

G. Martínez García¹⁰⁹, J. Martin Blanco¹⁰⁹, Y. Martynov³, A. Mas¹⁰⁹, S. Masciocchi⁹⁴, M. Masera²⁵, A. Masoni¹⁰³, L. Massacrier¹⁰⁹, A. Mastroserio³¹, H. Mathez¹²⁴, A. Matyja¹¹², C. Mayer¹¹², J. Mazer¹²⁰, R. Mazumder⁴⁵, M.A. Mazzoni¹⁰⁶, F. Meddi²², A. Menchaca-Rocha⁶², J. Mercado Pérez⁹⁰, M. Meres³⁶, Y. Miake¹²², K. Mikhaylov^{56,64}, L. Milano³⁴, J. Milosevic^{21,IV}, A. Mischke⁵⁵, A.N. Mishra⁴⁵, D. Miśkowiec⁹⁴, C.M. Mitu⁶⁰, J. Mlynarz¹²⁹, B. Mohanty^{126,77}, L. Molnar⁵², L. Montaño Zetina¹¹, E. Montes¹⁰, M. Morando²⁸, D.A. Moreira De Godoy¹¹⁵, S. Moretto²⁸, A. Morreale^{118,109}, A. Morsch³⁴, V. Muccifora⁷⁰, E. Mudnic¹¹¹, S. Muhuri¹²⁶, M. Mukherjee¹²⁶, H. Müller³⁴, M.G. Munhoz¹¹⁵, S. Murray^{87,63}, L. Musa³⁴, J. Musinsky⁵⁷, B.K. Nandi⁴⁴, R. Nania¹⁰², E. Nappi¹⁰¹, C. Natrass¹²⁰, T.K. Nayak¹²⁶, S. Nazarenko⁹⁶, A. Nedosekin⁵⁶, M. Nicassio⁹⁴, M. Niculescu^{34,60}, B.S. Nielsen⁷⁸, S. Nikolaev⁹⁷, S. Nikulin⁹⁷, V. Nikulin⁸³, B.S. Nilsen⁸⁴, F. Noferini^{12,102}, P. Nomokonov⁶⁴, G. Nooren⁵⁵, A. Nyanin⁹⁷, A. Nyatha⁴⁴, J. Nystrand¹⁸, H. Oeschler^{50,90}, S. Oh¹³¹, S.K. Oh^{65,V,40}, L. Olah¹³⁰, J. Oleniacz¹²⁸, A.C. Oliveira Da Silva¹¹⁵, J. Onderwaater⁹⁴, C. Oppedisano¹⁰⁸, F. Orsini¹⁴, A. Ortiz Velasquez³², A. Oskarsson³², J. Otwinowski⁹⁴, K. Oyama⁹⁰, Y. Pachmayer⁹⁰, M. Pachr³⁷, P. Pagano²⁹, G. Pać⁶¹, F. Painke³⁹, C. Pajares¹⁶, S.K. Pal¹²⁶, A. Palaha⁹⁹, A. Palmeri¹⁰⁴, D. Pant⁴⁴, V. Papikyan¹, G.S. Pappalardo¹⁰⁴, W.J. Park⁹⁴, A. Passfeld⁵¹, D.I. Patalakha⁵³, V. Paticchio¹⁰¹, B. Paul⁹⁸, T. Pawlak¹²⁸, T. Peitzmann⁵⁵, H. Pereira Da Costa¹⁴, E. Pereira De Oliveira Filho¹¹⁵, D. Peresunko⁹⁷, C.E. Pérez Lara⁷⁹, W. Peryt^{128,VI}, A. Pesci¹⁰², Y. Pestov⁵, V. Petráček³⁷, M. Petran³⁷, M. Petris⁷⁶, P. Petrov⁹⁹, M. Petrovici⁷⁶, C. Petta²⁷, S. Piano¹⁰⁷, M. Pikna³⁶, P. Pillot¹⁰⁹, O. Pinazza^{102,34}, L. Pinsky¹¹⁷, N. Pitz⁴⁹, D.B. Piyarathna¹¹⁷, M. Planinic^{95,123}, M. Płoskon⁷², J. Pluta¹²⁸, S. Pochybova¹³⁰, P.L.M. Podesta-Lerma¹¹⁴, M.G. Poghosyan³⁴, E.H.O. Pohjoisaho⁴², B. Polichtchouk⁵³, A. Pop⁷⁶, S. Porteboeuf-Houssais⁶⁸, J. Porter⁷², V. Posp³⁷, B. Potukuchi⁸⁸, S.K. Prasad¹²⁹, R. Preghenella^{12,102}, F. Prino¹⁰⁸, C.A. Pruneau¹²⁹, I. Pshenichnov⁵⁴, G. Puddu²³, P. Pujahari^{129,44}, V. Punin⁹⁶, J. Putschke¹²⁹, H. Qvigstad²¹, A. Rachevski¹⁰⁷, S. Raha⁴, J. Rak¹¹⁸, A. Rakotozafindrabe¹⁴, L. Ramello³⁰, R. Raniwala⁸⁹, S. Raniwala⁸⁹, S.S. Räsänen⁴², B.T. Rascanu⁴⁹, D. Rathee⁸⁵, A.W. Rauf¹⁵, V. Razazi²³, K.F. Read¹²⁰, J.S. Real⁶⁹, K. Redlich^{75,VII}, R.J. Reed¹³¹, A. Rehman¹⁸, P. Reichelt⁴⁹, M. Reicher⁵⁵, F. Reidt^{34,90}, C. Renard¹⁰⁹, R. Renfordt⁴⁹, A.R. Reolon⁷⁰, A. Reshetin⁵⁴, F. Rettig³⁹, J.-P. Revol³⁴, K. Reygers⁹⁰, R.A. Ricci⁷¹, T. Richert³², M. Richter²¹, P. Riedler³⁴, W. Riegler³⁴, F. Riggi²⁷, A. Rivetti¹⁰⁸, M. Rodríguez Cahuantzi², A. Rodriguez Manso⁷⁹, K. Røed²¹, E. Rogochaya⁶⁴, S. Rohni⁸⁸, D. Rohr³⁹, D. Röhrich¹⁸, R. Romita^{119,80}, F. Ronchetti⁷⁰, P. Rosnet⁶⁸, S. Rossegger³⁴, A. Rossi³⁴, A. Roy⁴⁵, C. Roy⁵², P. Roy⁹⁸, A.J. Rubio Montero¹⁰, R. Rui²⁴, R. Russo²⁵, E. Ryabinkin⁹⁷, A. Rybicki¹¹², S. Sadovsky⁵³, K. Šafařík³⁴, B. Sahlmuller⁴⁹, R. Sahoo⁴⁵, P.K. Sahu⁵⁹, J. Saini¹²⁶, H. Sakaguchi⁴³, D. Sakata¹²², C.A. Salgado¹⁶, J. Salzwedel¹⁹, S. Sambyal⁸⁸, V. Samsonov⁸³, X. Sanchez Castro^{52,61}, L. Šándor⁵⁷, A. Sandoval⁶², M. Sano¹²², G. Santagati²⁷, R. Santoro^{12,34}, D. Sarkar¹²⁶, E. Scapparone¹⁰², F. Scarlassara²⁸, R.P. Scharenberg⁹², C. Schiaua⁷⁶, E. Schibler¹²⁴, R. Schicker⁹⁰, C. Schmidt⁹⁴, H.R. Schmidt³³, S. Schuchmann⁴⁹, J. Schukraft³⁴, M. Schulc³⁷, T. Schuster¹³¹, Y. Schutz^{34,109}, K. Schwarz⁹⁴, K. Schweda⁹⁴, G. Scioli²⁶, E. Scomparin¹⁰⁸, P.A. Scott⁹⁹, R. Scott¹²⁰, G. Segato²⁸, J.E. Seger⁸⁴, I. Selyuzhenkov⁹⁴, J. Seo⁹³, E. Serradilla^{10,62}, A. Sevcenco⁶⁰, A. Shabetai¹⁰⁹, G. Shabratova⁶⁴, R. Shahoyan³⁴, A. Shangaraev⁵³, N. Sharma¹²⁰, S. Sharma⁸⁸, K. Shigaki⁴³, K. Shtejer²⁵, Y. Sibiriak⁹⁷, S. Siddhanta¹⁰³, T. Siemarczuk⁷⁵, D. Silvermyr⁸², C. Silvestre⁶⁹, G. Simatovic¹²³, R. Singaraju¹²⁶, R. Singh⁸⁸, S. Singha^{77,126}, V. Singhal¹²⁶, B.C. Sinha¹²⁶, T. Sinha⁹⁸, B. Sitar³⁶, M. Sitta³⁰, T.B. Skaali²¹, K. Skjerdal¹⁸, R. Smakal³⁷, N. Smirnov¹³¹, R.J.M. Snellings⁵⁵, C. Søgaard³², R. Soltz⁷³, J. Song⁹³, M. Song¹³², F. Soramel²⁸, S. Sorensen¹²⁰, M. Spacek³⁷, I. Sputowska¹¹², M. Spyropoulou-Stassinaki⁸⁶, B.K. Srivastava⁹², J. Stachel⁹⁰, I. Stan⁶⁰, G. Stefanek⁷⁵, M. Steinpreis¹⁹, E. Stenlund³², G. Steyn⁶³, J.H. Stiller⁹⁰, D. Stocco¹⁰⁹, M. Stolpovskiy⁵³, P. Strmen³⁶, A.A.P. Suaiide¹¹⁵, M.A. Subieta Vasquez²⁵, T. Sugitate⁴³, C. Suire⁴⁷, M. Suleymanov¹⁵, R. Sultanov⁵⁶, M. Šumbera⁸¹, T. Susa⁹⁵, T.J.M. Symons⁷², A. Szanto de Toledo¹¹⁵, I. Szarka³⁶, A. Szczepankiewicz³⁴, M. Szymanski¹²⁸, J. Takahashi¹¹⁶, M.A. Tangaro³¹, J.D. Tapia Takaki⁴⁷, A. Tarantola Peloni⁴⁹, A. Tarazona Martinez³⁴, A. Tauro³⁴, G. Tejeda Muñoz², A. Telesca³⁴,

C. Terrevoli³¹, A. Ter Minasyan^{97,74}, J. Thäder⁹⁴, D. Thomas⁵⁵, R. Tieulent¹²⁴, A.R. Timmins¹¹⁷, A. Toia^{105,49}, H. Torii¹²¹, V. Trubnikov³, W.H. Trzaska¹¹⁸, T. Tsuji¹²¹, A. Tumkin⁹⁶, R. Turrisi¹⁰⁵, T.S. Tveter²¹, J. Ulery⁴⁹, K. Ullaland¹⁸, J. Ulrich⁴⁸, A. Uras¹²⁴, G.L. Usai²³, M. Vajzer⁸¹, M. Vala^{57,64}, L. Valencia Palomo⁴⁷, P. Vande Vyvre³⁴, L. Vannucci⁷¹, J.W. Van Hoorn³⁴, M. van Leeuwen⁵⁵, A. Vargas², R. Varma⁴⁴, M. Vasileiou⁸⁶, A. Vasiliev⁹⁷, V. Vechernin¹²⁵, M. Veldhoen⁵⁵, M. Venaruzzo²⁴, P. Venault¹⁴, E. Vercellin²⁵, S. Vergara², R. Vernet⁸, M. Verweij^{129,55}, L. Vickovic¹¹¹, G. Viesti²⁸, J. Viinikainen¹¹⁸, Z. Vilakazi⁶³, O. Villalobos Baillie⁹⁹, A. Vinogradov⁹⁷, L. Vinogradov¹²⁵, Y. Vinogradov⁹⁶, T. Virgili²⁹, Y.P. Viyogi¹²⁶, A. Vodopyanov⁶⁴, M.A. Völk⁹⁰, K. Voloshin⁵⁶, S.A. Voloshin¹²⁹, G. Volpe³⁴, B. von Haller³⁴, I. Vorobyev¹²⁵, D. Vranic^{34,94}, J. Vrláková³⁸, B. Vulpescu⁶⁸, A. Vyushin⁹⁶, B. Wagner¹⁸, J. Wagner⁹⁴, V. Wagner³⁷, M. Wang^{7,VIII,109}, Y. Wang⁹⁰, D. Watanabe¹²², K. Watanabe¹²², M. Weber¹¹⁷, J.P. Wessels⁵¹, U. Westerhoff⁵¹, J. Wiechula³³, J. Wikne²¹, M. Wilde⁵¹, G. Wilk⁷⁵, J. Wilkinson⁹⁰, M.C.S. Williams¹⁰², B. Windelband⁹⁰, M. Winn⁹⁰, C. Xiang⁷, C.G. Yaldo¹²⁹, Y. Yamaguchi¹²¹, H. Yang^{14,55}, P. Yang⁷, S. Yang¹⁸, S. Yano⁴³, S. Yasnopolskiy⁹⁷, J. Yi⁹³, Z. Yin⁷, I.-K. Yoo⁹³, I. Yushmanov⁹⁷, V. Zaccolo⁷⁸, C. Zach³⁷, A. Zaman¹⁵, C. Zampolli¹⁰², S. Zaporozhets⁶⁴, A. Zarochentsev¹²⁵, P. Závada⁵⁸, N. Zaviyalov⁹⁶, H. Zbroszczyk¹²⁸, P. Zelnicek⁴⁸, I.S. Zgura⁶⁰, M. Zhalov⁸³, F. Zhang⁷, H. Zhang⁷, X. Zhang^{72,68,7}, Y. Zhang⁷, C. Zhao²¹, D. Zhou⁷, F. Zhou⁷, Y. Zhou⁵⁵, H. Zhu⁷, J. Zhu⁷, J. Zhu⁷, X. Zhu⁷, A. Zichichi^{12,26}, A. Zimmermann⁹⁰, M.B. Zimmermann^{34,51}, G. Zinovjev³, Y. Zoccarato¹²⁴, M. Zynovyev³, M. Zyzak⁴⁹

Affiliation Notes

^I Department of Applied Physics, Aligarh Muslim University, Aligarh, India

^{II} (1)CCNU;(2)also at LPC/Clermont Ferrand

^{III} Also at M.V.Lomonosov Moscow State University, D.V.Skobeltsyn Institute of Nuclear Physics, Moscow, Russia

^{IV} Also at University of Belgrade, Faculty of Physics and Vinča Institute of Nuclear Sciences, Belgrade, Serbia

^V Permanent address: Konkuk University, Seoul, Korea

^{VI} Deceased

^{VII} Also at Institute of Theoretical Physics, University of Wrocław, Wrocław, Poland

^{VIII} [(1)CCNU;(2)also at Subatech/Nantes]

Collaboration Institutes

¹ A. I. Alikhanyan National Science Laboratory (Yerevan Physics Institute) Foundation, Yerevan, Armenia

² Benemérita Universidad Autónoma de Puebla, Puebla, Mexico

³ Bogolyubov Institute for Theoretical Physics, Kiev, Ukraine

⁴ Bose Institute, Department of Physics and Centre for Astroparticle Physics and Space Science (CAPSS), Kolkata, India

⁵ Budker Institute for Nuclear Physics, Novosibirsk, Russia

⁶ California Polytechnic State University, San Luis Obispo, California, USA

⁷ Central China Normal University, Wuhan, China

⁸ Centre de Calcul de l

⁹ Centro de Aplicaciones Tecnológicas y Desarrollo Nuclear (CEADEN), Havana, Cuba

¹⁰ Centro de Investigaciones Energéticas Medioambientales y Tecnológicas (CIEMAT), Madrid, Spain

- ¹¹ Centro de Investigación y de Estudios Avanzados (CINVESTAV), Mexico City and Mérida, Mexico
¹² Centro Fermi - Museo Storico della Fisica e Centro Studi e Ricerche “Enrico Fermi”, Rome, Italy
¹³ Chicago State University, Chicago, USA
¹⁴ Commissariat à l’Energie Atomique, IRFU, Saclay, France
¹⁵ COMSATS Institute of Information Technology (CIIT), Islamabad, Pakistan
¹⁶ Departamento de Física de Partículas and IGFAE, Universidad de Santiago de Compostela, Santiago de Compostela, Spain
¹⁷ Department of Physics Aligarh Muslim University, Aligarh, India
¹⁸ Department of Physics and Technology, University of Bergen, Bergen, Norway
¹⁹ Department of Physics, Ohio State University, Columbus, Ohio, USA
²⁰ Department of Physics, Sejong University, Seoul, South Korea
²¹ Department of Physics, University of Oslo, Oslo, Norway
²² Dipartimento di Fisica dell
23 Dipartimento di Fisica dell’Università and Sezione INFN, Cagliari, Italy
²⁴ Dipartimento di Fisica dell’Università and Sezione INFN, Trieste, Italy
²⁵ Dipartimento di Fisica dell’Università and Sezione INFN, Turin, Italy
²⁶ Dipartimento di Fisica e Astronomia dell’Università and Sezione INFN, Bologna, Italy
²⁷ Dipartimento di Fisica e Astronomia dell’Università and Sezione INFN, Catania, Italy
²⁸ Dipartimento di Fisica e Astronomia dell’Università and Sezione INFN, Padova, Italy
²⁹ Dipartimento di Fisica ‘E.R. Caianiello’ dell’Università and Gruppo Collegato INFN, Salerno, Italy
³⁰ Dipartimento di Scienze e Innovazione Tecnologica dell’Università del Piemonte Orientale and Gruppo Collegato INFN, Alessandria, Italy
³¹ Dipartimento Interateneo di Fisica ‘M. Merlin’ and Sezione INFN, Bari, Italy
³² Division of Experimental High Energy Physics, University of Lund, Lund, Sweden
³³ Eberhard Karls Universität Tübingen, Tübingen, Germany
³⁴ European Organization for Nuclear Research (CERN), Geneva, Switzerland
³⁵ Faculty of Engineering, Bergen University College, Bergen, Norway
³⁶ Faculty of Mathematics, Physics and Informatics, Comenius University, Bratislava, Slovakia
³⁷ Faculty of Nuclear Sciences and Physical Engineering, Czech Technical University in Prague, Prague, Czech Republic
³⁸ Faculty of Science, P.J. Šafárik University, Košice, Slovakia
³⁹ Frankfurt Institute for Advanced Studies, Johann Wolfgang Goethe-Universität Frankfurt, Frankfurt, Germany
⁴⁰ Gangneung-Wonju National University, Gangneung, South Korea
⁴¹ Gauhati University, Department of Physics, Guwahati, India
⁴² Helsinki Institute of Physics (HIP), Helsinki, Finland
⁴³ Hiroshima University, Hiroshima, Japan
⁴⁴ Indian Institute of Technology Bombay (IIT), Mumbai, India
⁴⁵ Indian Institute of Technology Indore, India (IITI)
⁴⁶ Inha University, College of Natural Sciences
⁴⁷ Institut de Physique Nucléaire d’Orsay (IPNO), Université Paris-Sud, CNRS-IN2P3, Orsay, France
⁴⁸ Institut für Informatik, Johann Wolfgang Goethe-Universität Frankfurt, Frankfurt, Germany
⁴⁹ Institut für Kernphysik, Johann Wolfgang Goethe-Universität Frankfurt, Frankfurt, Germany
⁵⁰ Institut für Kernphysik, Technische Universität Darmstadt, Darmstadt, Germany
⁵¹ Institut für Kernphysik, Westfälische Wilhelms-Universität Münster, Münster, Germany
⁵² Institut Pluridisciplinaire Hubert Curien (IPHC), Université de Strasbourg, CNRS-IN2P3, Strasbourg, France
⁵³ Institute for High Energy Physics, Protvino, Russia
⁵⁴ Institute for Nuclear Research, Academy of Sciences, Moscow, Russia
⁵⁵ Institute for Subatomic Physics of Utrecht University, Utrecht, Netherlands

- ⁵⁶ Institute for Theoretical and Experimental Physics, Moscow, Russia
⁵⁷ Institute of Experimental Physics, Slovak Academy of Sciences, Košice, Slovakia
⁵⁸ Institute of Physics, Academy of Sciences of the Czech Republic, Prague, Czech Republic
⁵⁹ Institute of Physics, Bhubaneswar, India
⁶⁰ Institute of Space Science (ISS), Bucharest, Romania
⁶¹ Instituto de Ciencias Nucleares, Universidad Nacional Autónoma de México, Mexico City, Mexico
⁶² Instituto de Física, Universidad Nacional Autónoma de México, Mexico City, Mexico
⁶³ iThemba LABS, National Research Foundation, Somerset West, South Africa
⁶⁴ Joint Institute for Nuclear Research (JINR), Dubna, Russia
⁶⁵ Konkuk University
⁶⁶ Korea Institute of Science and Technology Information, Daejeon, South Korea
⁶⁷ KTO Karatay University, Konya, Turkey
⁶⁸ Laboratoire de Physique Corpusculaire (LPC), Clermont Université, Université Blaise Pascal, CNRS-IN2P3, Clermont-Ferrand, France
⁶⁹ Laboratoire de Physique Subatomique et de Cosmologie (LPSC), Université Joseph Fourier, CNRS-IN2P3, Institut Polytechnique de Grenoble, Grenoble, France
⁷⁰ Laboratori Nazionali di Frascati, INFN, Frascati, Italy
⁷¹ Laboratori Nazionali di Legnaro, INFN, Legnaro, Italy
⁷² Lawrence Berkeley National Laboratory, Berkeley, California, USA
⁷³ Lawrence Livermore National Laboratory, Livermore, California, USA
⁷⁴ Moscow Engineering Physics Institute, Moscow, Russia
⁷⁵ National Centre for Nuclear Studies, Warsaw, Poland
⁷⁶ National Institute for Physics and Nuclear Engineering, Bucharest, Romania
⁷⁷ National Institute of Science Education and Research, Bhubaneswar, India
⁷⁸ Niels Bohr Institute, University of Copenhagen, Copenhagen, Denmark
⁷⁹ Nikhef, National Institute for Subatomic Physics, Amsterdam, Netherlands
⁸⁰ Nuclear Physics Group, STFC Daresbury Laboratory, Daresbury, United Kingdom
⁸¹ Nuclear Physics Institute, Academy of Sciences of the Czech Republic, Řež u Prahy, Czech Republic
⁸² Oak Ridge National Laboratory, Oak Ridge, Tennessee, USA
⁸³ Petersburg Nuclear Physics Institute, Gatchina, Russia
⁸⁴ Physics Department, Creighton University, Omaha, Nebraska, USA
⁸⁵ Physics Department, Panjab University, Chandigarh, India
⁸⁶ Physics Department, University of Athens, Athens, Greece
⁸⁷ Physics Department, University of Cape Town, Cape Town, South Africa
⁸⁸ Physics Department, University of Jammu, Jammu, India
⁸⁹ Physics Department, University of Rajasthan, Jaipur, India
⁹⁰ Physikalisches Institut, Ruprecht-Karls-Universität Heidelberg, Heidelberg, Germany
⁹¹ Politecnico di Torino, Turin, Italy
⁹² Purdue University, West Lafayette, Indiana, USA
⁹³ Pusan National University, Pusan, South Korea
⁹⁴ Research Division and ExtreMe Matter Institute EMMI, GSI Helmholtzzentrum für Schwerionenforschung, Darmstadt, Germany
⁹⁵ Rudjer Bošković Institute, Zagreb, Croatia
⁹⁶ Russian Federal Nuclear Center (VNIIEF), Sarov, Russia
⁹⁷ Russian Research Centre Kurchatov Institute, Moscow, Russia
⁹⁸ Saha Institute of Nuclear Physics, Kolkata, India
⁹⁹ School of Physics and Astronomy, University of Birmingham, Birmingham, United Kingdom
¹⁰⁰ Sección Física, Departamento de Ciencias, Pontificia Universidad Católica del Perú, Lima, Peru
¹⁰¹ Sezione INFN, Bari, Italy

- ¹⁰² Sezione INFN, Bologna, Italy
¹⁰³ Sezione INFN, Cagliari, Italy
¹⁰⁴ Sezione INFN, Catania, Italy
¹⁰⁵ Sezione INFN, Padova, Italy
¹⁰⁶ Sezione INFN, Rome, Italy
¹⁰⁷ Sezione INFN, Trieste, Italy
¹⁰⁸ Sezione INFN, Turin, Italy
¹⁰⁹ SUBATECH, Ecole des Mines de Nantes, Université de Nantes, CNRS-IN2P3, Nantes, France
¹¹⁰ Suranaree University of Technology, Nakhon Ratchasima, Thailand
¹¹¹ Technical University of Split FESB, Split, Croatia
¹¹² The Henryk Niewodniczanski Institute of Nuclear Physics, Polish Academy of Sciences, Cracow, Poland
¹¹³ The University of Texas at Austin, Physics Department, Austin, TX, USA
¹¹⁴ Universidad Autónoma de Sinaloa, Culiacán, Mexico
¹¹⁵ Universidade de São Paulo (USP), São Paulo, Brazil
¹¹⁶ Universidade Estadual de Campinas (UNICAMP), Campinas, Brazil
¹¹⁷ University of Houston, Houston, Texas, USA
¹¹⁸ University of Jyväskylä, Jyväskylä, Finland
¹¹⁹ University of Liverpool, Liverpool, United Kingdom
¹²⁰ University of Tennessee, Knoxville, Tennessee, USA
¹²¹ University of Tokyo, Tokyo, Japan
¹²² University of Tsukuba, Tsukuba, Japan
¹²³ University of Zagreb, Zagreb, Croatia
¹²⁴ Université de Lyon, Université Lyon 1, CNRS/IN2P3, IPN-Lyon, Villeurbanne, France
¹²⁵ V. Fock Institute for Physics, St. Petersburg State University, St. Petersburg, Russia
¹²⁶ Variable Energy Cyclotron Centre, Kolkata, India
¹²⁷ Vestfold University College, Tønsberg, Norway
¹²⁸ Warsaw University of Technology, Warsaw, Poland
¹²⁹ Wayne State University, Detroit, Michigan, USA
¹³⁰ Wigner Research Centre for Physics, Hungarian Academy of Sciences, Budapest, Hungary
¹³¹ Yale University, New Haven, Connecticut, USA
¹³² Yonsei University, Seoul, South Korea
¹³³ Zentrum für Technologietransfer und Telekommunikation (ZTT), Fachhochschule Worms, Worms, Germany

References

- [1] ALICE, *Letter of Intent for the Upgrade of the ALICE Experiment*, CERN-LHCC-2012-012 (2012).
- [2] ALICE, K. Aamodt *et al.*, *The ALICE experiment at the CERN LHC*, JINST **3**, S08002 (2008), JINST **3**, S08002, doi:10.1088/1748-0221/3/08/S08002.
- [3] ALICE, G. Martinez Garcia, *Quarkonium production measurements with the ALICE detector at the LHC*, 1106.5889, arXiv:1106.5889.
- [4] ALICE, A. Dainese, *Heavy-flavour production in Pb-Pb collisions at the LHC, measured with the ALICE detector*, J.Phys. **G38**, 124032 (2011), arXiv:1106.4042, doi:10.1088/0954-3899/38/12/124032.
- [5] ALICE Collaboration, B. Abelev *et al.*, *Light vector meson production in pp collisions at $\sqrt{s} = 7$ TeV*, Phys. Lett. B **710**, 557 (2012), doi:10.1016/j.physletb.2012.03.038.
- [6] CMS, *Technical Proposal for the Upgrade of the CMS detector through 2020*, CERN-LHCC-2011-006 (2011).
- [7] ATLAS, *Letter of Intent for the Phase-I Upgrade of the ATLAS Experiment*, CERN-LHCC-2011-012 (2011).
- [8] ATLAS, *Letter of Intent for the Phase-II Upgrade of the ATLAS Experiment*, CERN-LHCC-2012-022 (2012).
- [9] LHCb, *Letter of Intent for the LHCb Upgrade*, CERN-LHCC-2011-001 (2011).
- [10] PHENIX Collaboration, K. Adcox *et al.*, *Formation of dense partonic matter in relativistic nucleus-nucleus collisions at RHIC: Experimental evaluation by the PHENIX collaboration*, Nucl.Phys. **A757**, 184 (2005), arXiv:nucl-ex/0410003, doi:10.1016/j.nuclphysa.2005.03.086.
- [11] STAR Collaboration, J. Adams *et al.*, *Experimental and theoretical challenges in the search for the quark gluon plasma: The STAR Collaboration's critical assessment of the evidence from RHIC collisions*, Nucl.Phys. **A757**, 102 (2005), arXiv:nucl-ex/0501009, doi:10.1016/j.nuclphysa.2005.03.085.
- [12] PHOBOS Collaboration, G. Roland *et al.*, *New results from the PHOBOS experiment*, Nucl.Phys. **A774**, 113 (2006), arXiv:nucl-ex/0510042, doi:10.1016/j.nuclphysa.2006.06.034.
- [13] BRAHMS Collaboration, P. Staszel, *Recent results from the BRAHMS experiment*, Nucl.Phys. **A774**, 77 (2006), arXiv:nucl-ex/0510061, doi:10.1016/j.nuclphysa.2006.06.031.
- [14] PHENIX Collaboration, A. Adare *et al.*, *J/ψ suppression at forward rapidity in Au+Au collisions at $\sqrt{s_{NN}} = 200$ GeV*, Phys.Rev. **C84**, 054912 (2011), arXiv:1103.6269, doi:10.1103/PhysRevC.84.054912.
- [15] PHENIX Collaboration, A. Adare *et al.*, *J/ψ Production vs Centrality, Transverse Momentum, and Rapidity in Au+Au Collisions at $\sqrt{s_{NN}} = 200$ GeV*, Phys.Rev.Lett. **98**, 232301 (2007), arXiv:nucl-ex/0611020, doi:10.1103/PhysRevLett.98.232301.
- [16] ALICE Collaboration, M. Guilbaud, *Pseudorapidity density of charged particles and its centrality dependence in Pb-Pb collisions at $\sqrt{s_{NN}} = 2.76$ -TeV*, Nucl.Phys. **A904-905**, 381c (2013), doi:10.1016/j.nuclphysa.2013.02.029.
- [17] BRAHMS Collaboration, D. Rohrich *et al.*, *Properties of matter at forward rapidities at RHIC*, Nucl.Phys. **A749**, 295 (2005), doi:10.1016/j.nuclphysa.2004.12.055.
- [18] Y. L. Dokshitzer and D. Kharzeev, *Heavy quark colorimetry of QCD matter*, Phys.Lett. **B519**, 199 (2001), arXiv:hep-ph/0106202, doi:10.1016/S0370-2693(01)01130-3.
- [19] S. Wicks, W. Horowitz, M. Djordjevic and M. Gyulassy, *Heavy quark jet quenching with collisional plus radiative energy loss and path length fluctuations*, Nucl.Phys. **A783**, 493 (2007),

- [arXiv:nucl-th/0701063](https://arxiv.org/abs/nucl-th/0701063), doi:[10.1016/j.nuclphysa.2006.11.102](https://doi.org/10.1016/j.nuclphysa.2006.11.102).
- [20] A. Adil and I. Vitev, *Collisional dissociation of heavy mesons in dense QCD matter*, Phys.Lett. **B649**, 139 (2007), [arXiv:hep-ph/0611109](https://arxiv.org/abs/hep-ph/0611109), doi:[10.1016/j.physletb.2007.03.050](https://doi.org/10.1016/j.physletb.2007.03.050).
- [21] V. Greco, C. Ko and R. Rapp, *Quark coalescence for charmed mesons in ultrarelativistic heavy ion collisions*, Phys.Lett. **B595**, 202 (2004), [arXiv:nucl-th/0312100](https://arxiv.org/abs/nucl-th/0312100), doi:[10.1016/j.physletb.2004.06.064](https://doi.org/10.1016/j.physletb.2004.06.064).
- [22] H. van Hees, V. Greco and R. Rapp, *Heavy-quark probes of the quark-gluon plasma at RHIC*, Phys.Rev. **C73**, 034913 (2006), [arXiv:nucl-th/0508055](https://arxiv.org/abs/nucl-th/0508055), doi:[10.1103/PhysRevC.73.034913](https://doi.org/10.1103/PhysRevC.73.034913).
- [23] D. Kharzeev, E. Levin and L. McLerran, *Parton saturation and N(part) scaling of semihard processes in QCD*, Phys.Lett. **B561**, 93 (2003), [arXiv:hep-ph/0210332](https://arxiv.org/abs/hep-ph/0210332), doi:[10.1016/S0370-2693\(03\)00420-9](https://doi.org/10.1016/S0370-2693(03)00420-9).
- [24] R. Baier, A. Kovner and U. A. Wiedemann, *Saturation and parton level Cronin effect: Enhancement versus suppression of gluon production in p-A and A-A collisions*, Phys.Rev. **D68**, 054009 (2003), [arXiv:hep-ph/0305265](https://arxiv.org/abs/hep-ph/0305265), doi:[10.1103/PhysRevD.68.054009](https://doi.org/10.1103/PhysRevD.68.054009).
- [25] N. Armesto, A. Dainese, C. A. Salgado and U. A. Wiedemann, *Testing the color charge and mass dependence of parton energy loss with heavy-to-light ratios at RHIC and CERN LHC*, Phys.Rev. **D71**, 054027 (2005), [arXiv:hep-ph/0501225](https://arxiv.org/abs/hep-ph/0501225), doi:[10.1103/PhysRevD.71.054027](https://doi.org/10.1103/PhysRevD.71.054027).
- [26] N. Armesto *et al.*, *Heavy Ion Collisions at the LHC - Last Call for Predictions*, J.Phys. **G35**, 054001 (2008), [arXiv:0711.0974](https://arxiv.org/abs/0711.0974), doi:[10.1088/0954-3899/35/5/054001](https://doi.org/10.1088/0954-3899/35/5/054001).
- [27] PHENIX, S. Adler *et al.*, *Centrality dependence of charm production from single electrons measurement in Au + Au collisions at $s(NN)^{**}(1/2) = 200$ -GeV*, Phys.Rev.Lett. **94**, 082301 (2005), [arXiv:nucl-ex/0409028](https://arxiv.org/abs/nucl-ex/0409028), doi:[10.1103/PhysRevLett.94.082301](https://doi.org/10.1103/PhysRevLett.94.082301).
- [28] PHENIX, S. Adler *et al.*, *Measurement of single electron event anisotropy in Au+Au collisions at $s(NN)^{**}(1/2) = 200$ -GeV*, Phys.Rev. **C72**, 024901 (2005), [arXiv:nucl-ex/0502009](https://arxiv.org/abs/nucl-ex/0502009), doi:[10.1103/PhysRevC.72.024901](https://doi.org/10.1103/PhysRevC.72.024901).
- [29] PHENIX, S. Adler *et al.*, *Nuclear modification of electron spectra and implications for heavy quark energy loss in Au+Au collisions at $s(NN)^{**}(1/2) = 200$ -GeV*, Phys.Rev.Lett. **96**, 032301 (2006), [arXiv:nucl-ex/0510047](https://arxiv.org/abs/nucl-ex/0510047), doi:[10.1103/PhysRevLett.96.032301](https://doi.org/10.1103/PhysRevLett.96.032301).
- [30] PHENIX, A. Adare *et al.*, *Heavy Quark Production in $p + p$ and Energy Loss and Flow of Heavy Quarks in Au+Au Collisions at $\sqrt{s_{NN}} = 200$ GeV*, Phys.Rev. **C84**, 044905 (2011), [arXiv:1005.1627](https://arxiv.org/abs/1005.1627), doi:[10.1103/PhysRevC.84.044905](https://doi.org/10.1103/PhysRevC.84.044905).
- [31] CMS, S. Chatrchyan *et al.*, *Suppression of non-prompt J/ψ , prompt J/ψ , and $Y(1S)$ in PbPb collisions at $\sqrt{s_{NN}} = 2.76$ TeV*, JHEP **1205**, 063 (2012), [arXiv:1201.5069](https://arxiv.org/abs/1201.5069), doi:[10.1007/JHEP05\(2012\)063](https://doi.org/10.1007/JHEP05(2012)063).
- [32] ALICE, B. Abelev *et al.*, *Suppression of high transverse momentum D mesons in central Pb-Pb collisions at $\sqrt{s_{NN}} = 2.76$ TeV*, JHEP **1209**, 112 (2012), [arXiv:1203.2160](https://arxiv.org/abs/1203.2160), doi:[10.1007/JHEP09\(2012\)112](https://doi.org/10.1007/JHEP09(2012)112).
- [33] ALICE, B. Abelev *et al.*, *Production of muons from heavy flavour decays at forward rapidity in pp and Pb-Pb collisions at $\sqrt{s_{NN}} = 2.76$ TeV*, Phys.Rev.Lett. **109**, 112301 (2012), [arXiv:1205.6443](https://arxiv.org/abs/1205.6443), doi:[10.1103/PhysRevLett.109.112301](https://doi.org/10.1103/PhysRevLett.109.112301).
- [34] T. Matsui and H. Satz, *J/ψ Suppression by Quark-Gluon Plasma Formation*, Physics Letters B **178**, 416 (1986), doi:[10.1016/0370-2693\(86\)91404-8](https://doi.org/10.1016/0370-2693(86)91404-8).
- [35] L. Kluberg and H. Satz, *Color Deconfinement and Charmonium Production in Nuclear Collisions*, 0901.3831, [arXiv:0901.3831](https://arxiv.org/abs/0901.3831).
- [36] B. Svetitsky, *Diffusion of charmed quarks in the quark-gluon plasma*, Phys.Rev. **D37**, 2484 (1988), doi:[10.1103/PhysRevD.37.2484](https://doi.org/10.1103/PhysRevD.37.2484).

- [37] P. Braun-Munzinger and J. Stachel, *(Non)thermal aspects of charmonium production and a new look at J/ψ suppression*, Phys.Lett. **B490**, 196 (2000), [arXiv:nucl-th/0007059](https://arxiv.org/abs/nucl-th/0007059), doi:[10.1016/S0370-2693\(00\)00991-6](https://doi.org/10.1016/S0370-2693(00)00991-6).
- [38] ALICE, B. Abelev, *J/ψ suppression at forward rapidity in Pb-Pb collisions at $\sqrt{s_{NN}} = 2.76$ TeV*, Phys.Rev.Lett. **109**, 072301 (2012), [arXiv:1202.1383](https://arxiv.org/abs/1202.1383), doi:[10.1103/PhysRevLett.109.072301](https://doi.org/10.1103/PhysRevLett.109.072301).
- [39] ALICE, C. Suire, *Charmonia production in ALICE*, 1208.5601, [arXiv:1208.5601](https://arxiv.org/abs/1208.5601).
- [40] ALICE, L. Massacrier, *J/ψ elliptic flow measurement in Pb-Pb collisions at $\sqrt{s_{NN}} = 2.76$ TeV at forward rapidity with the ALICE experiment*, 1208.5401, [arXiv:1208.5401](https://arxiv.org/abs/1208.5401).
- [41] PHENIX, A. Adare *et al.*, *J/ψ Production vs Centrality, Transverse Momentum, and Rapidity in Au-Au Collisions at $\sqrt{s_{NN}} = 200$ GeV*, Phys.Rev.Lett. **98**, 232301 (2007), [arXiv:nucl-ex/0611020](https://arxiv.org/abs/nucl-ex/0611020), doi:[10.1103/PhysRevLett.98.232301](https://doi.org/10.1103/PhysRevLett.98.232301).
- [42] X. Zhao and R. Rapp, *Medium Modifications and Production of Charmonia at LHC*, Nucl.Phys. A **859**, 114 (2011), [arXiv:1102.2194](https://arxiv.org/abs/1102.2194), doi:[10.1016/j.nuclphysa.2011.05.001](https://doi.org/10.1016/j.nuclphysa.2011.05.001).
- [43] Y.-p. Liu, Z. Qu, N. Xu and P.-f. Zhuang, *J/ψ Transverse Momentum Distribution in High Energy Nuclear Collisions at RHIC*, Phys. Lett. B **678**, 72 (2009), [arXiv:0901.2757](https://arxiv.org/abs/0901.2757), doi:[10.1016/j.physletb.2009.06.006](https://doi.org/10.1016/j.physletb.2009.06.006).
- [44] STAR, L. Adamczyk *et al.*, *Measurement of J/ψ Azimuthal Anisotropy in Au+Au Collisions at $\sqrt{s_{NN}} = 200$ GeV*, 1212.3304, [arXiv:1212.3304](https://arxiv.org/abs/1212.3304).
- [45] CMS, *Measurement of the $\psi(2S)$ meson in PbPb collisions at $\sqrt{s_{NN}} = 2.76$ TeV*, CMS-PAS-HIN-12-007, [arXiv:CMS-PAS-HIN-12-007](https://arxiv.org/abs/CMS-PAS-HIN-12-007).
- [46] ALICE, R. Arnaldi, *J/ψ and $\psi(2S)$ production in Pb-Pb collisions with the ALICE Muon Spectrometer at the LHC*, 1211.2578, [arXiv:1211.2578](https://arxiv.org/abs/1211.2578).
- [47] STAR Collaboration, A. Kesich, *Measurements of Υ Production and Nuclear Modification Factor at STAR*, J.Phys.Conf.Ser. **389**, 012025 (2012), [arXiv:1207.7166](https://arxiv.org/abs/1207.7166), doi:[10.1088/1742-6596/389/1/012025](https://doi.org/10.1088/1742-6596/389/1/012025).
- [48] CMS Collaboration, S. Chatrchyan *et al.*, *Observation of sequential Upsilon suppression in PbPb collisions*, Phys.Rev.Lett. **109**, 222301 (2012), [arXiv:1208.2826](https://arxiv.org/abs/1208.2826), doi:[10.1103/PhysRevLett.109.222301](https://doi.org/10.1103/PhysRevLett.109.222301).
- [49] A. Baltz *et al.*, *The Physics of Ultraperipheral Collisions at the LHC*, Phys.Rept. **458**, 1 (2008), [arXiv:0706.3356](https://arxiv.org/abs/0706.3356), doi:[10.1016/j.physrep.2007.12.001](https://doi.org/10.1016/j.physrep.2007.12.001).
- [50] C. A. Bertulani, S. R. Klein and J. Nystrand, *Physics of ultra-peripheral nuclear collisions*, Ann.Rev.Nucl.Part.Sci. **55**, 271 (2005), [arXiv:nucl-ex/0502005](https://arxiv.org/abs/nucl-ex/0502005), doi:[10.1146/annurev.nucl.55.090704.151526](https://doi.org/10.1146/annurev.nucl.55.090704.151526).
- [51] V. Rebyakova, M. Strikman and M. Zhalov, *Coherent rho and J/ψ photoproduction in ultraperipheral processes with electromagnetic dissociation of heavy ions at RHIC and LHC*, Phys.Lett. **B710**, 647 (2012), [arXiv:1109.0737](https://arxiv.org/abs/1109.0737), doi:[10.1016/j.physletb.2012.03.041](https://doi.org/10.1016/j.physletb.2012.03.041).
- [52] ALICE, B. Abelev *et al.*, *Coherent J/ψ photoproduction in ultra-peripheral Pb-Pb collisions at $\sqrt{s_{NN}} = 2.76$ TeV*, Phys.Lett. **B718**, 1273 (2013), [arXiv:1209.3715](https://arxiv.org/abs/1209.3715), doi:[10.1016/j.physletb.2012.11.059](https://doi.org/10.1016/j.physletb.2012.11.059).
- [53] A. Lardeux, (2012), Hot Quarks 2012, October 2012, Copamarina, Puerto-Rico.
- [54] J. Nystrand, (2010), First ReteQuarkonii Workshop, October 2010, Nantes, France.
- [55] E. de Oliveira, A. Martin and M. Ryskin, *Improving the Drell-Yan probe of small x partons at the LHC via a kt cut*, Eur.Phys.J. **C73**, 2361 (2013), [arXiv:1212.3135](https://arxiv.org/abs/1212.3135), doi:[10.1140/epjc/s10052-013-2361-6](https://doi.org/10.1140/epjc/s10052-013-2361-6).
- [56] L. McLerran and R. VENUGOPALAN, *Computing Quark and Gluon Distribution-Functions for Very Large Nuclei*, Physical Review D **49**, 2233 (1994).

- [57] L. McLerran and R. VENUGOPALAN, *Gluon Distribution-Functions for Very Large Nuclei at Small Transverse-Momentum*, Physical Review D **49**, 3352 (1994).
- [58] L. McLerran and R. VENUGOPALAN, *Green-Functions in the Color Field of a Large Nucleus*, Physical Review D **50**, 2225 (1994).
- [59] A. AYALA, J. JALILIANMARIAN, L. McLerran and R. VENUGOPALAN, *Gluon Propagator in Non-Abelian Weizsäcker-Williams Fields*, Physical Review D **52**, 2935 (1995).
- [60] A. AYALA, J. JALILIANMARIAN, L. McLerran and R. VENUGOPALAN, *Quantum corrections to the Weizsäcker-Williams gluon distribution function at small x* , Physical Review D **53**, 458 (1996).
- [61] PHOBOS Collaboration, C. PHOBOS, *Phobos results on charged particle multiplicity and pseudorapidity distributions in Au+Au, Cu+Cu, d+Au, and p+p collisions at ultra-relativistic energies*, Physical Review C **83**, 024913 (2011), [arXiv:1011.1940](https://arxiv.org/abs/1011.1940), [doi:10.1103/PhysRevC.83.024913](https://doi.org/10.1103/PhysRevC.83.024913).
- [62] CMS Collaboration, C. CMS, *Observation of Long-Range Near-Side Angular Correlations in Proton-Proton Collisions at the LHC*, JHEP **1009**, 091 (2010), [arXiv:1009.4122](https://arxiv.org/abs/1009.4122), [doi:10.1007/JHEP09\(2010\)091](https://doi.org/10.1007/JHEP09(2010)091).
- [63] ALICE Collaboration, C. ALICE, *J/ψ Production as a Function of Charged Particle Multiplicity in pp Collisions at $\sqrt{s} = 7$ TeV*, Physical Letters **B712**, 165 (2012), [arXiv:1202.2816](https://arxiv.org/abs/1202.2816), [doi:10.1016/j.physletb.2012.04.052](https://doi.org/10.1016/j.physletb.2012.04.052).
- [64] I. Abt, D. Emelyanov, I. Gorbunov and I. Kisel, *Cellular automaton and Kalman filter based track search in the HERA-B pattern tracker*, Nucl.Instrum.Meth. **A490**, 546 (2002), [doi:10.1016/S0168-9002\(02\)01097-5](https://doi.org/10.1016/S0168-9002(02)01097-5).
- [65] A. Bubak, M. Krauze, W. Zipper, I. Kisel and W. Müller, *TRD Tracking Using the Cellular Automaton Algorithm for Compressed Baryonic Matter Experiment*, Acta Physica Polonica B **41**, No. 1 (2010), <https://www-alt.gsi.de/documents/DOC-2010-Jan-101.html>.
- [66] A. Strandlie and R. Frühwirth, *Track and vertex reconstruction: From classical to adaptive methods*, Rev. Mod. Phys. **82**, 1419 (2010), [doi:10.1103/RevModPhys.82.1419](https://doi.org/10.1103/RevModPhys.82.1419).
- [67] A. Standli and R. Frühwirth, *Track and vertex reconstruction: From classical to adaptive methods*, Rev. Mod. Phys. **82**, 1419 (2010).
- [68] ALICE Collaboration, B. Abelev *et al.*, *Centrality determination of Pb-Pb collisions at $\sqrt{s_{NN}} = 2.76$ TeV with ALICE*, nucl-ex/1301.4361, [arXiv:nucl-ex/1301.4361](https://arxiv.org/abs/nucl-ex/1301.4361).
- [69] A. Collaboration, *ALICE: Physics Performance Report, Volume II*, Journal of Physics G: Nuclear and Particle Physics **32**, 1295 (2006).
- [70] ALICE Collaboration, B. Abelev *et al.*, *Measurement of inelastic, single- and double-diffraction cross sections in proton-proton collisions at the LHC with ALICE*, Eur.Phys.J. C (2012), [arXiv:1208.4968](https://arxiv.org/abs/1208.4968).
- [71] S. Grigoryan, *Private communication*.
- [72] ALICE Collaboration, B. Abelev *et al.*, *J/ψ Suppression at Forward Rapidity in Pb-Pb Collisions at $\sqrt{s_{NN}} = 2.76$ TeV*, Phys. Rev. Lett. **109**, 072301 (2012), [doi:10.1103/PhysRevLett.109.072301](https://doi.org/10.1103/PhysRevLett.109.072301).
- [73] ALEPH, D. Buskulic *et al.*, *Measurement of the \bar{B}^0 and B^- meson lifetimes*, Phys. Lett. B **307**, 194 (1993).
- [74] ALEPH, D. Buskulic *et al.*, *Errata: Measurement of the \bar{B}^0 and B^- meson lifetimes*, Phys. Lett. B **325**, 537 (1993).
- [75] LHCb, *Measurement of J/ψ production in pp collisions at $\sqrt{s} = 7$ TeV*, Eur. Phys. J. C **71**, 1645 (2011).
- [76] A. Andronic, K. Braun-Munzinger, P. Redlich and J. Stachel, *The thermal model on the verge*

- of the ultimate test: particle production in Pb–Pb collisions at the LHC*, J. Phys. G **38**, 124081 (2011), [doi:10.1088/0954-3899/38/12/124081](https://doi.org/10.1088/0954-3899/38/12/124081).
- [77] A. Andronic, *Private communication*.
- [78] P. Braun-Munzinger and J. Stachel, *(Non)thermal aspects of charmonium production and a new look at J/ψ suppression*, Phys. Lett. B **490**, 196 (2000), [doi:10.1016/S0370-2693\(00\)00991-6](https://doi.org/10.1016/S0370-2693(00)00991-6).
- [79] A. Andronic, K. Braun-Munzinger, P. Redlich and J. Stachel, *Statistical hadronization of heavy quarks in ultra-relativistic nucleus-nucleus collisions*, Nucl. Phys. A **789**, 334 (2007), [doi:10.1016/j.nuclphysa.2007.02.013](https://doi.org/10.1016/j.nuclphysa.2007.02.013).
- [80] A. Andronic, K. Braun-Munzinger, P. Redlich and J. Stachel, *Evidence for charmonium generation at the phase boundary in ultra-relativistic nuclear collisions*, Phys. Lett. B **652**, 259 (2007), [doi:10.1016/j.physletb.2007.07.036](https://doi.org/10.1016/j.physletb.2007.07.036).
- [81] R. Thews, M. Schroedter and J. Rafelski, *Enhanced J/ψ production in deconfined quark matter*, Phys. Rev. C **63**, 054905 (2001), [doi:10.1103/PhysRevC.63.054905](https://doi.org/10.1103/PhysRevC.63.054905).
- [82] M. Cacciari, M. Greco and P. Nason, *The p_T Spectrum in Heavy-Flavour Hadroproduction*, JHEP **05**, 007 (1998), [doi:10.1088/1126-6708/1998/05/007](https://doi.org/10.1088/1126-6708/1998/05/007).
- [83] ALICE, B. Abelev *et al.*, *Measurement of the Cross Section for Electromagnetic Dissociation with Neutron Emission in Pb–Pb Collisions at $\sqrt{s_{NN}} = 2.76$ TeV*, Phys. Rev. Lett. **109**, 252302 (2012), [doi:10.1103/PhysRevLett.109.252302](https://doi.org/10.1103/PhysRevLett.109.252302).
- [84] J. Uphoff, O. Fochler, Z. Xu and C. Greiner, *Open heavy flavor in Pb+Pb collisions at $\sqrt{s}=2.76$ TeV within a transport model*, Phys. Lett. B **717**, 430 (2012), [doi:10.1016/j.physletb.2012.09.069](https://doi.org/10.1016/j.physletb.2012.09.069).
- [85] R. Rapp, private communications.
- [86] R. Rapp and J. Wambach, *Low mass dileptons at the CERN SPS: Evidence for chiral restoration?*, Eur.Phys.J. **A6**, 415 (1999), [arXiv:hep-ph/9907502](https://arxiv.org/abs/hep-ph/9907502), [doi:10.1007/s100500050364](https://doi.org/10.1007/s100500050364).
- [87] H. van Hees and R. Rapp, *Dilepton Radiation at the CERN Super Proton Synchrotron*, Nucl.Phys. **A806**, 339 (2008), [arXiv:0711.3444](https://arxiv.org/abs/0711.3444), [doi:10.1016/j.nuclphysa.2008.03.009](https://doi.org/10.1016/j.nuclphysa.2008.03.009).
- [88] R. Rapp, *Theory of Soft Electromagnetic Emission in Heavy-Ion Collisions*, Acta Phys.Polon. **B42**, 2823 (2011), [arXiv:1110.4345](https://arxiv.org/abs/1110.4345), [doi:10.5506/APhysPolB.42.2823](https://doi.org/10.5506/APhysPolB.42.2823).
- [89] Y. Degerli *et al.*, *Development of Binary Readout CMOS Monolithic Sensors for MIP Tracking*, IEEE Trans. Nucl. Sci. **56** (2009).
- [90] C. Hu-Guo *et al.*, *First reticule size MAPS with digital output and integrated zero suppression for the EUDET-JRA1 beam telescope*, NIMA **623** (2010), [doi:10.1016/j.nima.2010.03.043](https://doi.org/10.1016/j.nima.2010.03.043).
- [91] ALICE MFT collaboration, *A Muon Forward Tracker for the ALICE Experiment*, ALICE Internal Document **ALICE-INT-2013-XXX** (2013).
- [92] ALICE collaboration, *Upgrade of the Inner Tracking System Conceptual Design Report*, **CERN-LHCC-2012-013** (2012).
- [93] P. Moreira *et al.*, *The GBT-SerDes ASIC prototype*, JINST **5**, C11022 (2010), [doi:10.1088/1748-0221/5/11/C11022](https://doi.org/10.1088/1748-0221/5/11/C11022).
- [94] Samtec, *One piece interface, SIBF series*, <http://www.samtec.com/documents/webfiles/pdf/sibf.pdf>.
- [95] W. H. T. et al., *T0 upgrade proposal*, <https://indico.cern.ch/conferenceDisplay.py?confId=229958>, 24th January, 2013, ALICE Technical Board.
- [96] L. Musa, *ALICE Upgrade with focus on ITS*, LHCC Upgrade Session, December 4th, 2012.